SPATIAL AND TEMPORAL MEASUREMENTS USING POLYOXOMETALATE, ENZYMATIC AND BIOFILM LAYERS ON A CMOS 0.35 μm 64 X 64-PIXEL I.S.F.E.T. ARRAY SENSOR

A THESIS SUBMITTED TO
THE DEPARTMENT OF ELECTRONICS AND ELECTRICAL ENGINEERING
SCHOOL OF ENGINEERING
UNIVERSITY OF GLASGOW
IN FULFILMENT OF THE REQUIREMENTS
FOR THE DEGREE OF
DOCTOR OF PHILOSOPHY

By
Angelos Streklas
March 2015

To the loving memory of my grandmother

Abstract

This thesis presents the achievements and scientific work conducted using a previously designed and fabricated 64 x 64-pixel ion camera with the use of a 0.35 μm CMOS technology. We used an array of Ion Sensitive Field Effect Transistors (ISFETs) to monitor and measure chemical and biochemical reactions in real time. The area of our observation was a 4.2 x 4.3 mm silicon chip while the actual ISFET array covered an area of 715.8 x 715.8 μm consisting of 4096 ISFET pixels in total with a 1 μm separation space among them. The ion sensitive layer, the locus where all reactions took place was a silicon nitride layer, the final top layer of the austriamicrosystems 0.35 μm CMOS technology used. Our final measurements presented an average sensitivity of 30 mV/pH. With the addition of extra layers we were able to monitor a 65 mV voltage difference during our experiments with glucose and hexokinase, whereas a difference of 85 mV was detected for a similar glucose reaction mentioned in literature, and a 55 mV voltage difference while performing photosynthesis experiments with a biofilm made from cyanobacteria, whereas a voltage difference of 33.7 mV was detected as presented in literature for a similar cyanobacterial species using voltamemtric methods for detection.

To monitor our experiments PXIe-6358 measurement cards were used and measurements were controlled by LabVIEW software. The chip was packaged and encapsulated using a PGA-100 chip carrier and a two-component commercial epoxy. Printed circuit board (PCB) has also been previously designed to provide interface between the chip and the measurement cards.

Acknowledgements

This thesis would not have been completed without the help and support of many people. First of all, I would like to thank my supervisor, Prof. David R. S. Cumming for giving me the opportunity to participate in this interesting and challenging project. His advice, guidance, encouragement and overall support was very important throughout this thesis. Also, I would like to thank Prof. Lee Cronin, Prof. Mike Barrett, Dr. Alasdair MacDonald, Dr. Mark D. Symes, Dr. Christoph Busche, Dr. Soichiro Tsuda and Gordon Campbell for sharing with me all the necessary chemical, biological and technical knowledge and for their collaboration on my research.

I would also like to thank all colleagues from the MicroSystem group, Dr. Li Chong, Dr. Feng Hong, Pete Shields, Dr. Mohamed Al-Rawhani, Pete McPherson, Boon Cheah Chong, Dr. James Grant and Iain McCrindle for their scientific support and other people from Rankine Building Dr. Lourdes Ferre Llin, Dr. Kirsty Walls and Dr. Fatemeh Aghamoradi for being supportive and sharing with me good banter during lunch breaks.

Many thanks to Dr. Balazs Nemeth who shared his own technical achievements with me and for providing me guidance to my first steps in the world of sensors and electrolytic solutions.

Special thanks to my good friend and office mate Ivonne Escorcia Carranza for her help on the electronic design process, for being patient with me when freaking out with my work and providing encouragement throughout the whole duration of the PhD.

I would like to express my warm thanks to my good friend Dr. Vasileios Papageorgiou for being an excellent flat mate and always cheerful and encouraging during our challenging journey living in Glasgow. Our talks, basketball sessions and bike rides were very stress relieving.

I wish to express my sincere appreciation to the Engineering and Physical Sciences Research Council (EPSRC) for their financial support to this project.

Finally, I deeply thank my parents Yanni and Kiki as well as my sister Iliana for their love and support throughout every stage of my life. Many thanks also to Maria, Michael, Christina, Bill, Gianna, Giorgos, Christiana, Arman, Katerina, Thomai, Danae, Kostas, Eirianna, Rodi and many other people related with one way or another to this challenging four-year journey in Glasgow.

Publications

a. Conference Paper

Nemeth, B., Streklas A., Boulay, A.G., Symes, M., Busche, C., Cronin, L., Cumming, D.R.S ‘’*Development of a 64×64-pixel ion camera chip for ionic imaging using an unmodified 0.35 μm CMOS technology*’’ The 17th International Conference on Solid-State Sensors, Actuators and Microsystems (TRANSDUCERS & EUROSENSORS XXVII), 2013 Transducers & Eurosensors XXVII. June 2013

b. Oral presentations

‘’*Development of a ion camera chip for ionic imaging using an unmodified 0.35μm CMOS technology*’’ EPSRC mMOS Meeting, Department of Chemistry, University of Glasgow June 2013

c. Poster presentations

Streklas A., Nemeth, B., Chong B.C., Cumming D.R.S. ‘*0.35μm CMOS 64x64 pixel ion camera chip for real-time ionic imaging*’ Royal Society meeting: the long arm of microelectronics, *Kavli Royal Society International Centre, Buckinghamshire, May 2013*

Contents

List of Figures

List of Tables

1. Introduction

1.1 Motivation

Electronics can be considered the biggest revolution in modern technology, as within a couple of decades it has completely transformed practically everything in science, entertainment, industry, medicine and everyday life. Especially, most of machinery and devices for medical applications have developed highly sophisticated robustness and accuracy thanks to the advanced features offered by electronic design which served diagnostic purposes at the most, but also affecting other aspects. Semiconductor technology continued advancing and applications were becoming more and more efficient and scalable.

Among all inventions, ion sensors came to be established as an important tool in medical diagnostics and now play a significant role in biomedical engineering in general. The ions sensors, commonly known as ion sensitive field effect transistors (ISFETs) was an idea firstly conceived by P. Bergveld from the University of Twente [2]. ISFET sensors were basically transistors with their gate removed and replaced by electrolyte, thus enabling pH measurements and moreover the detection of other ionic activity in solution. The initial size of the ISFETs varied starting to be in the scale of micrometres, but modern circuit integration has enabled a reduction in size the scale of microns. This advantage made ion detection possible to areas where bulky machinery would be inapplicable.

ISFETs are capable of not only detecting but monitoring ionic activity both in temporal and spatial resolution. The latter became feasible when ISFETs were able to be organised in arrays with the use of standard unmodified CMOS technology. The fabrication of ISFET devices was in the beginning carried out with the use of a standard CMOS process where the gate metal had to be removed. Later on ISFETs could also be produced with the use of sub-micron unmodified CMOS processes lowering the costs of fabrication and providing more standardised performance [3] [4]. Digital circuitry and any additional electronics [5] became easier to embed through these processes giving the ISFET multiple variations.

The most commonly used passivation layer in these processes is silicon nitride, a material that elicits a response to the majority of ion species, making sensing difficult for specific ions. Thus, efforts have been made to engage additional layers to introduce ion selectivity. However, ISFETs mostly have served in research mainly as proton-sensitive devices. Moreover hydrogen cations are found in most of measurable assays, electrolytes, salts and biological tissues.

In this thesis an integrated ion imaging system is introduced based on a 64x64-pixel ISFET array technology. The chips were fabricated in an unmodified 4-metal layer 0.35 μm CMOS process by austriamicrosystems. It will be shown in later chapters that the imaging array is a 715.8 μm x 715.8 μm area which is covered with 4096 sensor units. Each sensor unit covers an area of 10.2 μm x 10.2 μm providing the resolution of our array. The array has been used before to measure ionic activity of acids [1], chemical oscillating reactions [6] and monitor polyoxometalate structures [7]. On this thesis we developed a better way of packaging and tried to achieve lower noise mainly by new cleaning techniques of the chip and better maintained reference electrodes. We experimented with other cations besides protons such as sodium and potassium ions and we introduced polyoxometalate layers to achieve selectivity for ions such as potassium. Also, measurements with other extra layers have been conducted: Experiments with a Hexokinase layer to study the first reaction of the glycolysis path and experiments with biofilms to study bacterial photosynthesis.

In conclusion, ISFET research is an important part of the biomedical engineering research. New tools, new techniques with less cost and more effectiveness to serve as diagnostic sensors for a variety of health problems such as cancer, cardiovascular diseases and any other situation or syndrome that can be investigated through ionic behaviour or solutions such as human serum. To be more specific also in the focus of this research, regarding also the possible applications we can emphasize the use of the additional sensitive layers which provide great versatility to the ISFET sensors:

- The use of the POMs inducing selectivity for potassium ions can be useful for human serum monitoring, as there are many health conditions related with potassium cation concentrations.

- Monitoring the glycolysis reaction with the use of the sepharose beads layer, one of the most important reactions in biochemistry. A key for all metabolomics related with cancer research and degenerative diseases.
- Monitoring ionic activity of cyanobacteria. This kind of bacterial cells have the ability to increase voltage amplitude when light is applied on the surface of the formed biofilm. This could be a very early stage of a biological battery in the form of bio-photovoltaic cells. A low cost and green source of producing electricity to power simple devices.

1.2 Objectives

This thesis is focused on the progress achieved with the use of mainly the unmodified 0.35 μm CMOS technology and the ISFET sensor array. More specifically the thesis' work is presented below:

- Extensive testing and further reliability and robustness measurements on an existing 0.35 μm CMOS fabricated ISFET sensor array.
- Optimisation of packaging and on peripheral procedures in order to reduce noise and increase accuracy of measurements.
- Measurement of H, Na and K cations in aqueous solutions in relation with voltage amplitude and measurements with the use of a selective polyoxometalate layer for potassium ions.
- Monitoring temporally and spatially the first step of glycolysis reaction with the use of a layer infused with Hexokinase.
- Studying the ionic behaviour of the photosynthetic cyanobacterium Synechocystis sp. PCC 6803: Ionic oscillations in darkness and light, biofilm formation and an attempt to monitor photosynthesis in real time.

All these objectives can be found also organised in chapters as presented in the next section:

1.3 Organisation of the chapters

The thesis is organised in chapters in the following manner:

Chapter 1 **Introduction**

Introduction to the 64 x 64 ISFET sensor array system and its measurements. Motivation objectives and organisation of the chapters are presented.

Chapter 2 **Theory**

The basic theoretical principles are presented. The definition of the pH measure, charge transfer across an interface and the Electrolyte-Insulator-Semiconductor Interface is examined as a physical system with the appropriate mathematical formalism. The Site Binding model is also examined for both silicon dioxide and silicon nitride surfaces and an overview on the basic principles of the ISFET transistor. The chapter ends with a short introduction of the concept of the additional layers that can be added on the ISFET surface for more ion specific measurements.

Chapter 3 **Literature Review**

Provides a literature review on the development of potentiometric sensors and of ion sensitive field-effect transistors (ISFETs) leading to more complex systems such as ISFET arrays for more advanced measurements. The CMOS fabrication process is also examined. There are also mentioned examples of extra layers on fabricated surfaces.

Chapter 4 **The 64x64 pixel sensor array system**

Presentation of the 64x64 pixel ISFET sensor array. Cross-sectional view of the 0.35 μm technology used, an overview of the single pixel schematic, layout, all additional digital circuitry and the final integration to an ISFET array is also described. There are also descriptions about packaging and encapsulation of the

ISFET chip. The chapter ends outlining the real-time data acquisition process with the use of some additional hardware and software tools.

Chapter 5 **Performance with H, Na and K cations**

This chapter presents some introductory results in measuring hydrogen, sodium and potassium cations using single-pixel measurements. Additional polyoxometalate (POM) layers were introduced and it was attempted thus to create selective cation sensors for potassium.

Chapter 6 **Experiments with enzymes**

This chapter describes the interaction of the ISFET array with enzymes. A preliminary measurement with the enzyme papain was conducted leading to the assumption that the formation of a precipitate was recorded. After that, a series of experiments were conducted in order to monitor the first step of the glycolysis reaction. This time measurements were conducted showing both temporal and spatial resolution providing data for studying the diffusion kinetics.

Chapter 7 **Experiments with cyanobacteria**

This chapter is about the ionic behaviour of the cyanobacterium Synechocystis sp. PCC 6803. Oscillations were detected and other periodic signals likely related with the organism's circadian behaviour or with some other standard periodic reactions such as nitrogen fixation. The ability of the Synechocystis to photosynthesize was also examined and also the formation of the bacterial culture into films on top of the sensor's surface for more accurate measurements.

1.4 Summary-Conclusion

On this chapter we discussed about the motivation of this thesis and its context in the field of science and technology. We went through the main objectives of the project: Testing the 64 x 64 pixel ISFET array, optimizing encapsulation and packaging techniques. Experiments with various cations with extra embedded

layers, enzymic and bacterial films. There is also a section where we indicate how the thesis is organised in chapters.

2. Theory

2.1 Introduction

This chapter is about basic concepts on physics and chemistry concerning the Ion-Sensitive-Field-Effect Transistors (ISFET) and their applications. An ISFET is a modified version of a MOSFET introduced by Bergveld in 1970 [8]. pH measurement theory will be briefly introduced and the 'site-binding model', the mechanism that explains the electrolyte-insulator-semiconductor interface will be explained. There will be also an overview of the interface charge transfer on our devices and a few words about the reference electrodes and basic ideas on ISFET operation.

2.2 pH measurement

In the study of aqueous solutions a magnitude was needed to measure the acidity or the alkalinity of a solution. Sørensen introduced the idea of pH in 1909. The initials stand for ''power of hydrogen'' and it is actually a measure of the molar concentration of hydrogen ions in an aqueous solution [9]. pH is expressed with the following equation:

$$pH = -\log_{10}[H^+] \tag{2.1}$$

where H^+ stands for the molar concentration of hydrogen ions. This definition places pure water pH to be around 7 as a boundary. Values lower than 7, are considered to be acidic and larger than 7 are considered to be alkaline. The scale ranges from 0 to 14. The correlation between measured voltage output on the ISFET surface and ionic concentration of the solution [10] is going to be studied extensively on this chapter.

2.2.1 Charge transfer across an interface

Measurement of pH can be a simple and straight forward process with solutions but more complicated when dealing with interfaces, such as the insulator-electrolyte interface in ion sensitive transistors. So the introduction of the interface potential difference $\Delta\phi$ is needed. Electronic charge transfer across an interface kinetics can be described by the Butler-Volmer equation [11]. Equation 2.2 is not only used to describe insulator-electrolyte interface charge transfer but can be generalised to any active process where charge exchange occurs. It stands as a basic form to describe potential difference across any interface which separates two distinct phases.

$$\mathrm{J}_p = z_p F \vec{k}_p [X_p]_\beta \exp\left(\frac{z_p F \zeta \Delta\phi}{RT}\right) - z_p F \overleftarrow{k}_p [X_p]_\alpha \exp\left(\frac{-z_p F (1-\zeta)\Delta\phi}{RT}\right) \qquad (2.2)$$

Exchange net current density J_p is expressed as magnitude depending of the potential difference across the interface, more specifically between ß-phase (solid) and α-phase (liquid), $\Delta\phi = (\phi_\beta - \phi_\alpha)$ and the ionic concentration of species *p* in the two phases, $[X_p]_\beta$ and $[X_p]_\alpha$. $\vec{k}_p$ and $\overleftarrow{k}_p$ stand for the heterogeneous rate constants for forward and reverse ionic flux across the interface respectively. z_p is the formal ionic charge and ζ the symmetry coefficient between flux directions, ranging from 0 to 1 but with typical value of 0.5 [12]. R is the universal gas constant, T absolute temperature and F the Faraday constant. Exchange net current density is actually a difference between ionic fluxes between the two distinct phases and can be expressed as:

$$J_p = \vec{J}_p - \overleftarrow{J}_p \qquad (3.3)$$

where $\vec{J}_p$ stands for the flux out of solid phase and $\overleftarrow{J}_p$ into solid phase [12]. If various mobile ion species were present, the exchange current of all *m* ion fluxes would be expressed as [12]:

$$J_{tot} = \sum_{p=1}^{m} \vec{J}_p = \sum_{p=1}^{m} \left(\vec{J}_p - \overleftarrow{J}_p \right) \tag{2.4}$$

Current density behaviour in relation to $\Delta\phi$ is shown in Fig. 2.1 for the case of a single ion species. Total current density J_{tot} is shown with a dotted line. Open-circuit potential difference is defined as the value of $\Delta\phi$ when J_{tot} is zero. It can also be considered as an equilibrium potential ($\Delta\phi_{p(eq)}$) for the forward and reverse exchange currents of the interface. Focusing on a single ion species (*p=1*) and solving equation (2.2) we can derive $\Delta\phi$:

$$\Delta\phi = \frac{RT}{z_p F} \ln \frac{k_p}{k_p} + \frac{RT}{z_p F} \ln \frac{\left[X_p \right]_\alpha}{\left[X_p \right]_\beta} = \phi_k + \frac{RT}{z_p F} \ln \frac{\left[X_p \right]_\alpha}{\left[X_p \right]_\beta} \tag{2.5}$$

Assuming that the concentration of the ion species in ß-phase remains constant, we can then combine constant ϕ_k with $\left[X_p \right]_\beta$ which yields:

$$\Delta\phi = \phi_k' + \frac{RT}{z_p F} \ln \left[X_p \right]_\alpha = \phi_k' + 2.303 \frac{RT}{z_p F} \log \left[X_p \right]_\alpha \tag{2.6}$$

Equation (2.6) is an expression of the Nerst equation that relates ionic concentrations with potential difference. $\Delta\phi$ versus $\log\left[X_p\right]_\alpha$ gives a linear behaviour with a slope of *59.2 mV/decade* for univalent ions (z_p=*1*) at 25° C. This is considered to be the ideal response, which is also known as Nerstian response [11]. During measurements specific ion selective electrodes and membranes are been chosen in order to transport selectively a single ion species across the interface and thus achieve a better Nerstian response.

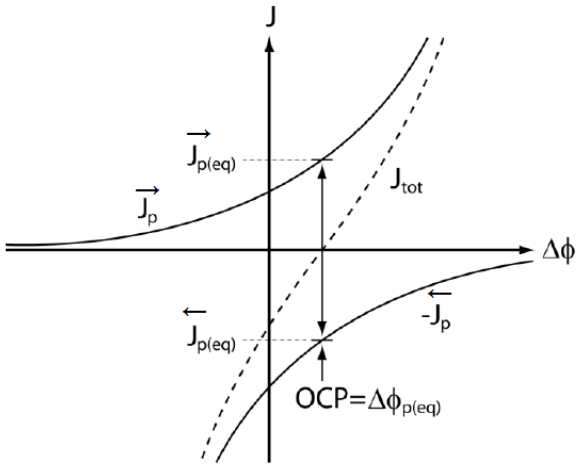

Fig. 2.1: Graph of forward and reverse ion exchange currents versus interface potential for a single ion species [12]

2.3 Electrolyte-Insulator-Semiconductor Interface

A redistribution of charge and potential occurs at an interface when we bring two phases of different electrochemical properties into contact. This happens until the electrochemical potential of the charge carriers become equal in both phases. Thus, the electrochemical properties of this electrolyte-insulator-semiconductor interface are determined by this redistribution of charge and potential. The solution part of this interface has been analysed with a model made by Grahame [13]. This model consists of three regions as shown in Fig. 2.2

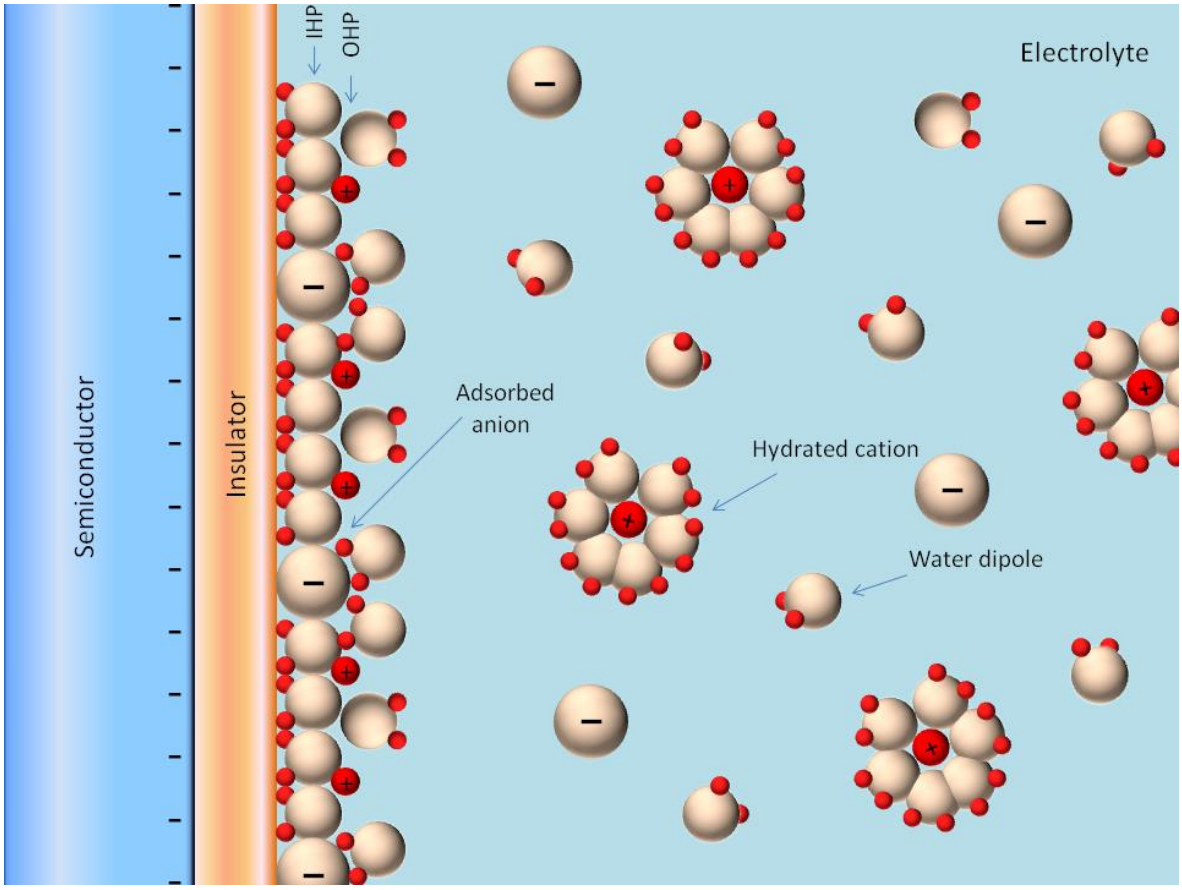

Fig. 2.2: Electrolyte-insulator-semiconductor (EIS) interface [13].

The first region consists of water molecules and ions which are specifically adsorbed onto the insulator surface. The locus of the electrical centres of these adsorbed ions is called the *inner Helmholtz plane* (IHP) and we define the total charge density of this region as σ_0. Hydrated ions in the solution are prevented from coming to close to the surface due to the existence of the IHP, nevertheless the closest approach of the hydrated ion forms the second region which is called *outer Helmholtz plane* (OHP). The third region of the model consists of a diffuse charge region, extending from OHP to the bulk of the electrolyte and is called *Gouy-Chapman layer*.

The surface of the insulator contacts with the electrolyte and hydrolyses to form surface groups. These groups can be positively, negatively or neutrally charged depending on the pH of the electrolyte. We define point of zero charge pH(pzc) the pH on the surface when charge is zero. We also call H^+ and OH^- potential-determining ions as they are responsible for the state of the charge on surface. Charge distribution and potential distribution are determined by whether the surface adsorbs positive (Fig. 2.3b) or negative (Fig. 2.3a).

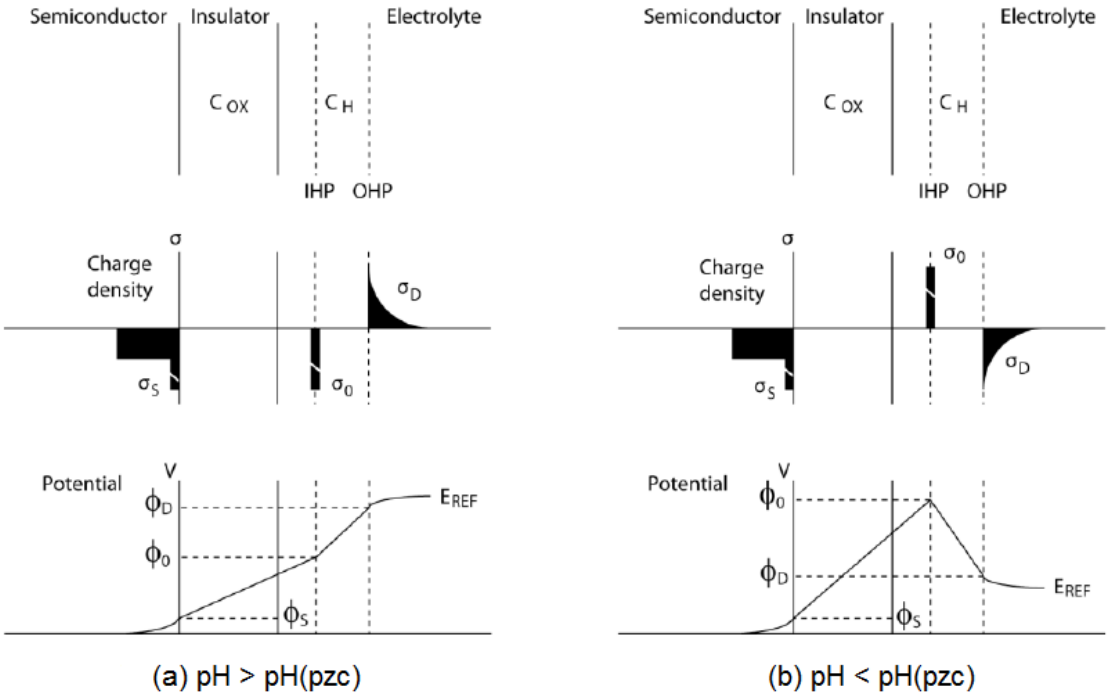

Fig. 2.3: Charge and potential distribution on the EIS interface [14].

We define charge density in the Gouy-Chapman region as σ_D, so now the total charge in the solution is $\sigma_0 + \sigma_D$. If we now also add the charge density of the semiconductor region that is σ_S and consider the concept of charge being neutral we get:

$$\sigma_0 + \sigma_D + \sigma_S = 0 \tag{2.7}$$

More over since the potential across the EIS surface has to be continuous we get:

$$E_{REF} + (\phi_D - E_{REF}) + (\phi_0 - \phi_D) + (\phi_S - \phi_0) - \phi_S = 0 \tag{2.8}$$

and also,

$$\phi_0 - \phi_S = -\frac{\sigma_S}{C_{OX}} \tag{2.9}$$

$$\phi_0 - \phi_D = -\frac{\sigma_D}{C_H} \tag{2.10}$$

$$\phi_D - E_{REF} = -\frac{2kT}{q}\sinh^{-1}\left(\frac{\sigma_D}{\sqrt{8\varepsilon kTc}}\right) \tag{2.11}$$

where k is the Boltzmann constant, ε the electrolyte permittivity and c the ionic concentration. Equation (3.11) shows the Gouy-Chapman model for the third region [11]. Finally, by combining all equations we can write:

$$E_{REF} + \underbrace{\left[-\frac{2kT}{q}\sinh^{-1}\left(\frac{\sigma_D}{\sqrt{8\varepsilon kTc}}\right) - \frac{\sigma_D}{C_H}\right]}_{\phi_{EI} = -\Delta\phi} + \underbrace{\left[\frac{\sigma_S}{C_{OX}} - \phi_S\right]}_{\phi_{IS}} = 0 \tag{2.12}$$

where E_{REF} is the externally applied reference potential. ϕ_{EI} and ϕ_{IS} are the potentials of the electrolyte-insulator and insulator-semiconductor interfaces respectively. This equations shows us how the interface potential $\Delta\phi$ and charge density are related on the EIS interface.

2.4 Site binding model

Ideally the boundary of the interface, where electrolyte and semiconductor meet would be a locus where ions meet the physical barrier of the solid as they move into the solution and further they can react with the semiconductor's impurity atoms if the latter is doped with them. The opposite idea would suggest a total blocked interface with the electrolyte molecules in abundance preventing any ionic reaction between the two phases. In reality what happens is something in between. Yates in 1974 described the interactions taking place on a oxide-electrolyte surface by developing the 'site-binding model' [15]. This

description can help us calculate pH response for the oxides used on our ISFET devices: SiO_2 and Si_3N_4, as these two are the basic layers used in our experiments which will be presented extensively later in chapters 5, 6 and 7.

2.4.1. Silicon dioxide

When silicon dioxide is brought in contact with aqueous solution, hydrolysis occurs and silanol (SiOH) groups are formed on the surface (Fig. 2.4). These silanol groups depending on the electrolyte pH can be positively, negatively or neutrally charged. The neutral site of silanol can have an acidic or basic character shown by the reactions below along with their equilibrium constants:

$$SiOH_2^+ \rightleftharpoons SiOH + H^+ \qquad K_{A1} = \frac{[\mathrm{SiOH}][\mathrm{H}^+]_S}{[SiOH_2^+]} \tag{2.13}$$

$$SiOH \rightleftharpoons SiO^- + H^+ \qquad K_{A2} = \frac{[\mathrm{SiO}^-][\mathrm{H}^+]_S}{[SiOH]} \tag{2.14}$$

where subscript S indicates surface quantity. Density of sites on surface N_A and charge per unit area $\sigma_{0\mathrm{A}}$ can be seen below [16]:

$$N_A = [SiOH_2^+] + [\mathrm{SiOH}] + [\mathrm{SiO}^-] \tag{2.15}$$

$$\sigma_{0\mathrm{A}} = q([SiOH_2^+] - [\mathrm{SiO}^-]) \tag{2.16}$$

The surface concentration of H^+ in relation with the bulk concentration of H^+ can be described as below due to thermal mixing, according to Boltzmann statistics [15]:

$$[H^+]_S = [H^+]\exp(-\frac{q\Delta\phi}{kT}) \tag{2.17}$$

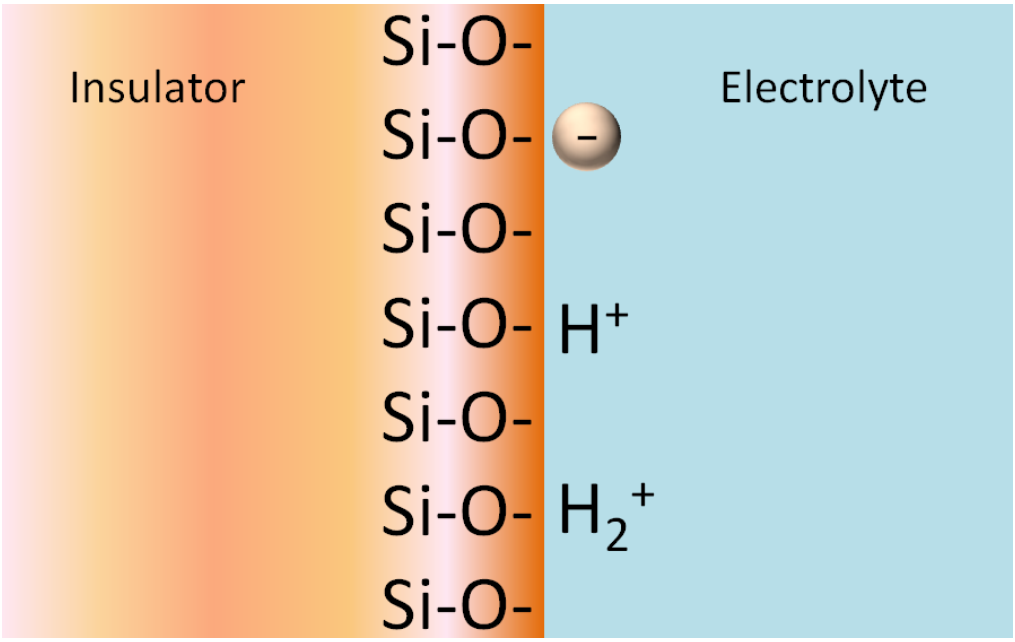

Fig. 2.4: Surface sites and reactions for silicon dioxide

where $\Delta\phi$ is the potential difference between electrolyte bulk and insulator surface. Using (2.13), (2.14) and (2.17) we get:

$$[H^+] = \sqrt{K_{A1}K_{A2}}\exp(\frac{q\Delta\phi}{kT})\sqrt{\frac{[SiOH_2^+]}{[\mathrm{SiO^-}]}} \tag{2.18}$$

If $\Delta\phi = 0$ and $\sigma_{0A} = 0$ (that is for example: $[SiOH_2^+] = [\mathrm{SiO^-}]$) then (2.18) gives $[H^+] = \sqrt{K_{A1}K_{A2}}$, with this being the concentration for $[H^+]$ in the solution that is needed for a neutral surface to be produced and is related to the point of zero charge (pzc). pH at this point is noted as $pH(pzc)_A$ and (2.18) can be written as:

$$2.303(pH(pzc)_A - pH) = \frac{q\Delta\phi}{kT} + \ln F_A \tag{2.19}$$

providing an equation which charge, potential and pH are linked. The function:

$$F_A = \sqrt{[SiOH_2^+]/[\mathrm{SiO^-}]} \tag{2.20}$$

is an important indicator of the response of the surface. Parameter χ_A is defined below as normalised net charge on the surface, in order to solve this function:

$$\chi_A = \frac{\sigma_{0A}}{qN_A} = \frac{[SiOH_2^+]-[\mathrm{SiO^-}]}{[SiOH_2^+]+[\mathrm{SiOH}]+[\mathrm{SiO^-}]} \tag{2.21}$$

Dividing by $[\mathrm{SiO^-}]$, we find χ_A as a function of F_A:

$$\chi_A = \frac{F_A{}^2 - 1}{F_A{}^2 + F_A\sqrt{K_{A1}K_{A2}} + 1} \tag{2.22}$$

We can invert this equation, defining also $\delta = 2\sqrt{K_{A2}/K_{A1}}$ and picking the positive root of the quadratic to produce $F_A(\chi_A)$:

$$F_A{}^2(\chi_A - 1) + F_A\frac{2\chi_A}{\delta} + \chi_A + 1 = 0 \tag{2.23}$$

$$F_A = \frac{\chi_A/\delta + \sqrt{(\chi_A/\delta)^2(1-\delta^2)+1}}{1-\chi_A} \tag{2.24}$$

Equations (2.19) and (2.24) can express pH of the solution as a function of both $\Delta\phi$ and σ_{0A}. Using the definition for $\Delta\phi$ from (2.12) , a direct link between $\Delta\phi$ and σ_{0A} can be found, which is shown by:

$$\Delta\phi = \frac{2kT}{q}\sinh^{-1}\left(\frac{\sigma_D}{\sqrt{8\varepsilon kTc}}\right) + \frac{\sigma_D}{C_H} \tag{2.25}$$

Considering charge to be neutral for the EIS interface:

$$\sigma_D + \sigma_{0A} = \Delta\sigma = -\sigma_s \tag{2.26}$$

We normally assume that $\Delta\sigma = 0$, so σ_D = - σ_{0A} [17]. Now we can solve for $\Delta\phi/\mathrm{pH}$ using a parametric method. Considering χ_A as a parameter, $\Delta\phi$ from (2.25) then F_A is found from (2.24). Using these two in (2.19) the solution pH is determined. Equilibrium constants and surface site densities for silicon dioxide can be found in literature and are $\mathrm{K}_{A1} = 10^{1.8}$, $K_{A2} = 10^{-6.2}$ and $N_A = 5\cdot 10^{18} sites/m^2$ [16]. Using these values on the site binding model it can be seen that silicon dioxide surface presents a *-46.3mV/pH* sensitivity at pH=7.

Point of zero charge can be found at pH=2.2 which indicated a highly non-linear response in the acidic pH range as shown in Fig. 2.5

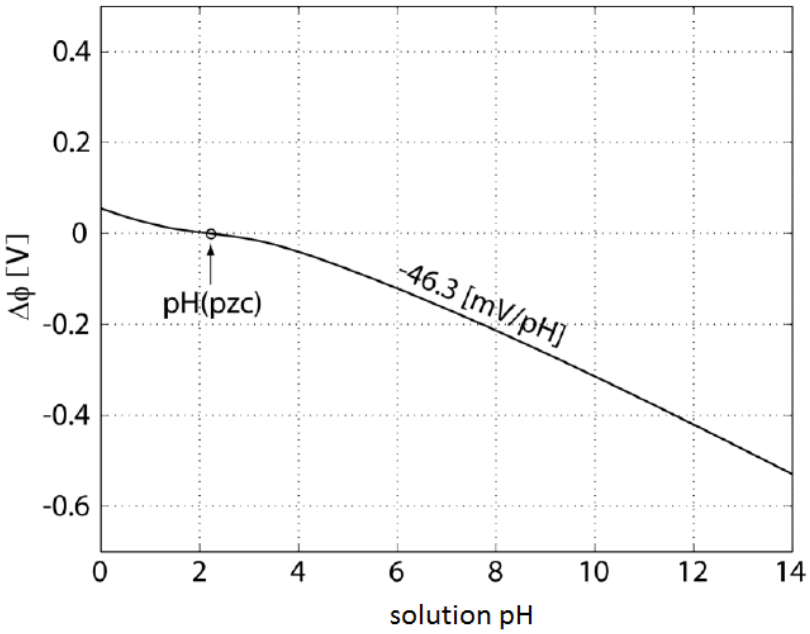

Fig. 2.5: Theoretical response of pH of a silicon dioxide surface [18]

We can see from the above that silicon dioxide cannot provide us with linear pH range for our measurements, so an alternative material is required to serve as an insulator. Moreover, other material such as silicon nitride studied in the next paragraph provide us with bigger sensitivity ensuring more accurate measurements.

2.4.2. Silicon nitride

The surface of silicon nitride surface forms Si_3N sites, because each nitrogen atom is considered to bond to three silicon atoms. When silicon nitride surface interacts with an aqueous solution we get these sites from the hydrolysis [16]:

$$Si_3N + H_2O \longrightarrow Si_2NH + SiOH \tag{2.27}$$

The Si_2NH are hydrolysed further to produce:

$$Si_2NH + H_2O \longrightarrow SiNH_2 + SiOH \qquad (2.28)$$

so the total product of hydrolysis is both $SiOH$ and $SiNH_2$ surface sites as can be seen in Fig. 2.6.

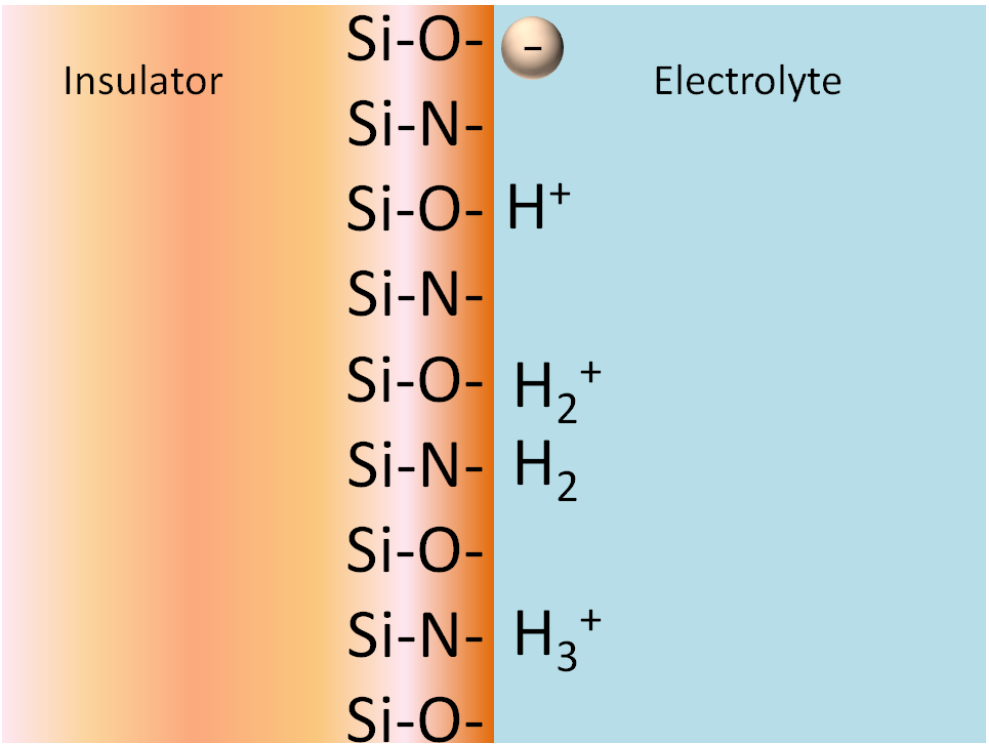

Fig. 2.6: Surface sites and reactions for silicon nitride

The behaviour of $SiOH$ sites has already been discussed (2.13, 2.14) while the behaviour of $SiNH_2$ sites is shown below:

$$SiNH_3^+ \rightleftharpoons SiNH_2 + H^+ \qquad K_B = \frac{[SiNH_2][H^+]_S}{[SiNH_3^+]} \qquad (2.29)$$

The density of $SiNH_2$ on the surface and the surface charge per unit area are also given below:

$$N_B = [SiNH_2] + [SiNH_3^+] \tag{2.30}$$

$$\sigma_{0B} = q[SiNH_3^+] \tag{2.31}$$

Following similar procedure as outlined in the previous section, we get:

$$2.303(pK_B - pH) = \frac{q\Delta\phi}{kT} + \ln\left(\frac{[SiNH_3^+]}{N_B - [SiNH_3^+]}\right) \tag{2.32}$$

where pK_B is -logK$_B$. Here we only have positive and neutral sites, so the point of zero charge occurs when $[SiNH_3^+]$ is zero. We get the equivalent F-function as before for the $SiNH_2$ sites if we compare (2.19) with (2.32):

$$F_B = \frac{[SiNH_3^+]}{N_B - [SiNH_3^+]} = \frac{\chi_B}{1 - \chi_B} \tag{2.33}$$

The above refers to only $SiNH_2$ sites. Now if we consider both $SiNH_2$ and $SiOH$ groups, we get total density of sites to be $N = N_A + N_B$ and also:

$$\frac{N_A}{N}+\frac{N_B}{N}=f_A+f_B=1 \tag{2.34}$$

So total normalised charge per unit area χ is:

$$\chi=\frac{q([SiOH_2^+]-[SiO^-]+[SiNH_3^+])}{N}=f_A\chi_A+f_B\chi_B \tag{2.35}$$

Using the definitions for χ_A and χ_B given before we get:

$$\chi=f_A\frac{F_A{}^2-1}{F_A{}^2+F_A\sqrt{K_{A1}K_{A2}}+1}+f_B\frac{F_B}{F_B+1} \tag{2.36}$$

Subtracting (2.19) from (2.32) we obtain the R ratio between the two F-functions:

$$R=\frac{F_B}{F_A}=10^{(pK_B-pH_{A(pzc)})}=\frac{\sqrt{K_{A1}K_{A2}}}{K_B} \tag{2.37}$$

Point of zero charge for silicon nitride surface occurs when $\chi=0$ and pH also equals $pH(pzc)$. If we add the constant $2.303(pH(pzc)-pH(pzc)_A)$ to (2.19) we have:

$$2.303(pH(pzc)-pH)=\frac{q\Delta\phi}{kT}+\ln F \tag{2.38}$$

Where here F-function is:

$$F=10^{(pH(pzc)-pH(pzc)_A)}F_A \tag{2.39}$$

So pH= $pH(pzc)$ and $\Delta\phi$ *=0* at the point of zero charge. So (2.38) gives *F(pzc)=1*. Putting this value in (2.39) we get:

$$pH(pzc)=pH(pzc)_A-\log F_A(pzc) \tag{2.40}$$

We can use a parametric method again to solve and find the $\Delta\phi/\mathrm{pH}$ response by following the steps below:

1. define χ_A as parameter
2. evaluate F_A from (2.24)
3. find F_B from (2.37)
4. calculate χ_B using (2.33)
5. derive χ from (2.35)
6. find $\Delta\phi$ using (2.25)
7. find F using 2.39
8. find the solution pH by solving (2.38)

Equilibrium constants and surface site densities for silicon nitride can be found in the literature and are listed as: $K_{A1} = 10^{1.8}$, $K_{A2} = 10^{-6.2}$, $K_B = 10^{-10}$, $N_A = 5 \cdot 10^{18} sites/m^2$ and $N_B = 2 \cdot 10^{18} sites/m^2$ [16]. Using these values on the site binding model it can be seen that silicon nitride surface presents a pH value of 6.5 at the point of zero charge. Moreover we can see that the silicon nitride surface presents a linear behaviour across the pH range and its theoretical sensitivity reaches *-56.7mV/pH* (Fig. 2.7) [16].

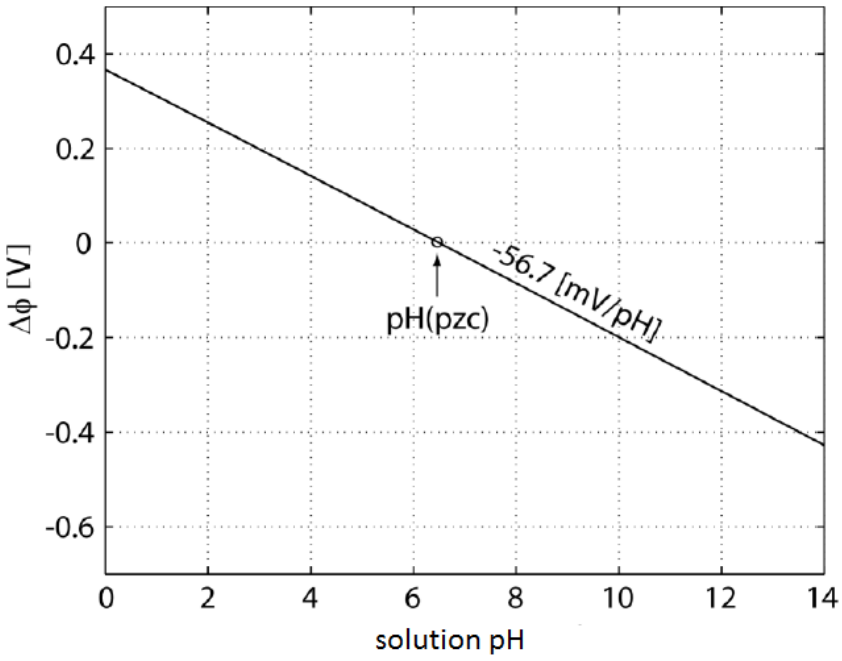

Fig. 2.7: Theoretical response of pH of a silicon nitride surface [18]

At that point we can mention, in an attempt to compare theoretical values with experimental results presented in this thesis, that we managed to reach this theoretical number of 56.7 mV/pH by achieving a 50 mV difference from pH=4 to pH=3 (10^{-4}M $\rightarrow 10^{-3}$M in concentration of HCl). This result was achieved at the final experiments where techniques and packaging were optimized as can be seen in chapter 5, Fig. 5.13.

2.5 The Ion Sensitive Field Effect Transistor

The need to measure the interface potential eventually led to the creation of a device based on the semiconductor technology as early as 1970 [2] called ISFET. ISFET operation is quite similar to MOSFET operation. In a n-channel MOSFET, when a voltage is applied to the gate, electrons are attracted from the p-type bulk to the surface underneath the oxide layer (Fig 2.8). When this voltage reaches the threshold voltage, we notice inversion of this area of substrate, in our case from p-type to n-type. Thus, a n-type channel is formed between source and drain which enables carriers to flow into it. This inversion can only be achieved if the surface potential is increased from its initial negative value $\phi_S = -\phi_F$ to a positive value $\phi_S = \phi_F$ by passing through zero ($\phi_S = 0$), where ϕ_F is the Fermi potential. The minimum potential on the gate required to produce this state, also known as strong inversion is called threshold voltage V_T and it can be seen below:

$$V_T = V_{FB} - \frac{Q_B}{C_{OX}} + 2\phi_F \tag{2.41}$$

V_{FB} is the flatband voltage, Q_B is the depletion charge in the silicon substrate, and C_{OX} is the capacitance of the oxide layer. V_{FB} is given by:

$$V_{FB} = \frac{\Phi_M - \Phi_S}{q} - \frac{Q_{SS} + Q_{OX}}{C_{OX}} \tag{2.42}$$

where $\Phi_M - \Phi_S$ is the work function difference between the gate and the bulk silicon, q is the electronic charge, Q_{SS} is the surface state density on the surface of the silicon and Q_{OX} is the fixed oxide charge. From these two equations we can clearly see that threshold voltage V_T of a MOSFET is a function of the properties of the material used, such as the work function difference $\Phi_M - \Phi_S$ and the charge accumulation.

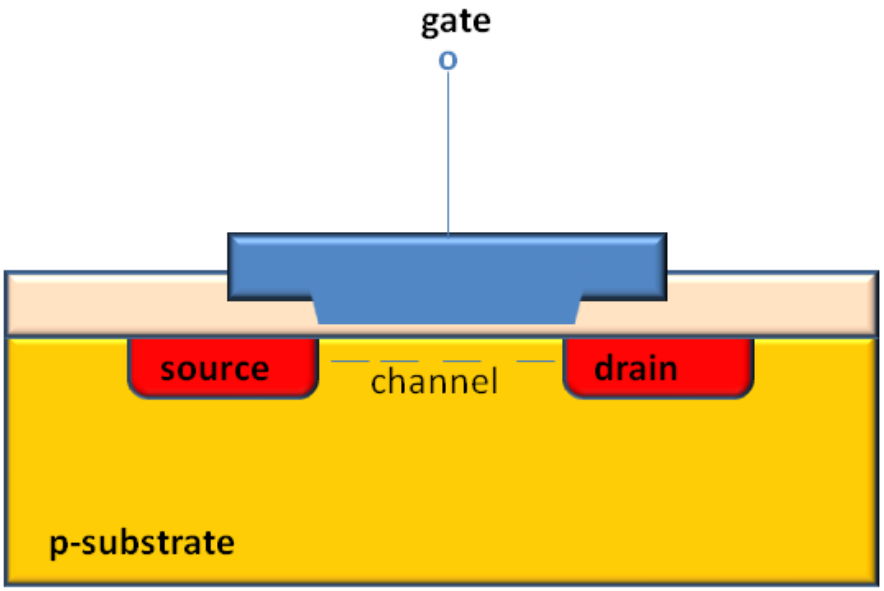

Fig. 2.8: Cross-section view of a MOSFET

In the case of the ISFET, the MOSFET metal gate is replaced by the metal of a reference electrode and the aqueous solution where the reference electrode is positioned in contact with the gate oxide (Fig 2.9). Here, our gate voltage is the potential that we apply to the reference electrode. Threshold voltage in this case contains terms that relate to the characteristics of the interface between the solution and the gate oxide and also between the solution and the reference electrode. For the first term, the potential refers to gate oxide-electrolyte interface $\Delta\phi + \chi_{SOL}$ and is constant defined by the surface dipole potential of the aqueous solution χ_{SOL} and the interface potential $\Delta\phi$ which is concentration-dependent. For the second term, behaviour is defined by the reference

electrode potential E_{REF} where the associated work function Φ_M is included. So the ISFET's flatband voltage is given by:

$$V_{FB} = E_{REF} - \Delta\phi + \chi_{SOL} - \frac{\Phi_S}{q} - \frac{Q_{SS} + Q_{OX}}{C_{OX}} \tag{2.43}$$

From the above we can see that the only term which is not constant is the $\Delta\phi$ and thus becomes the term which defines the ISFET's sensitivity to the electrolyte pH. This makes the ISFET to be an ideal transducer for measuring ionic concentrations in a solution with also high input impedance and low output impedance.

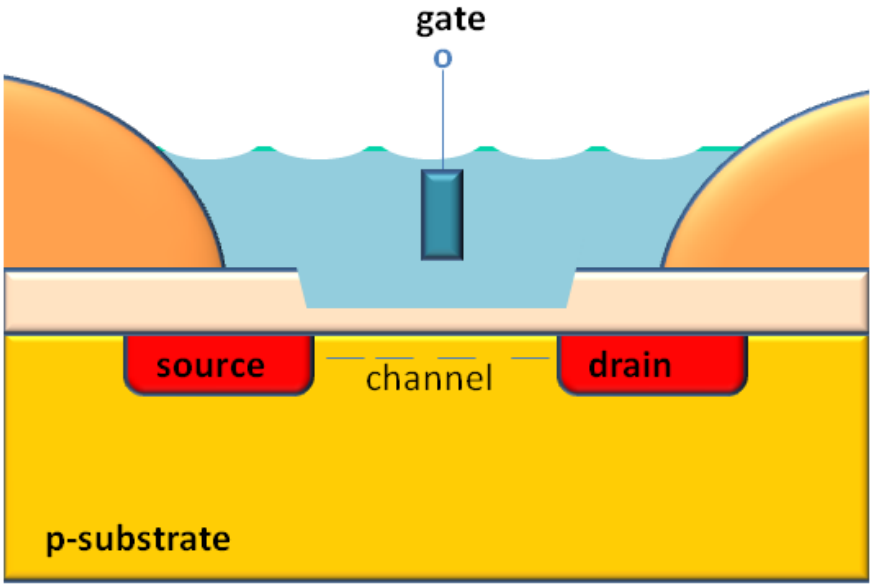

Fig. 2.9: Cross-section view of an ISFET

2.6 Additional layers

For more specific measurements, such as selective ionic monitoring (i.e. potassium ions) or measurements with living cells or other biological materials, additional layers covering the oxide membrane can be engaged. In this work, we

focused on making layers of polyoxometalate crystals, biofilms with photosynthetic bacteria, as the one shown in Fig. 2.10 and layers of sepharose beads with immobilised enzymes onto them. All these attempts will be presented in chapters 5, 6 and 7 along with some basic information about the materials used and their properties related with our research

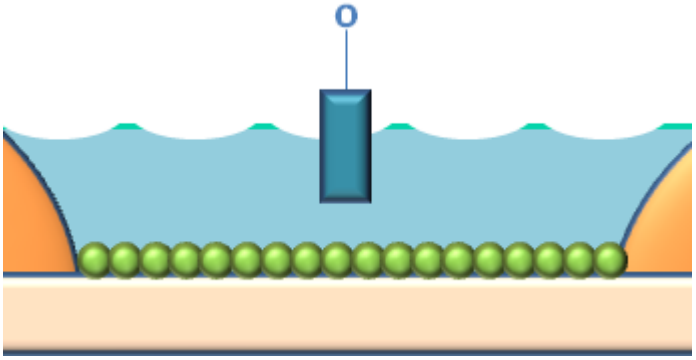

Fig. 2.10: A biofilm made of cyanobacteria acting as an additional layer on the oxide surface.

2.7 Summary

In this chapter a model of the charge transfer across an interface of two separate phases was presented. Also the electrolyte-insulator-semiconductor interface was studied thoroughly based on previous theoretical work on layer interactions. Then the site-binding model was expounded to investigate the relation between interface potential and ionic concentration of the aqueous solution with a focus on two basic materials: silicon dioxide and silicon nitride. Finally an overview of the basic mechanism of an ISFET was presented in addition to a short introduction to the concept of additional layers that can be embedded to the ISFET device for more specific measurements and will be explored further in the later chapters on a discussion about certain experiments

2.8 Conclusion

Throughout the theoretical examination of the aspects of the ISFETs we can conclude that this devices can act as charged molecule sensors presenting

adequate linearity, especially for the silicon nitrate layer. Moreover, additional layers can be applied on the surface of the sensors enabling them to monitor specific mechanisms like biochemical reactions of bacteria or inducing selectivity to the detection of ions. Ionic selectivity is discussed extensively in chapter 5 and biochemical reactions on chapters 6 and 7 where glucose and bacterial reactions are presented.

3. Literature review

3.1 Introduction

This chapter will focus on the literature relevant to potentiometric sensors and transistor-based devices related to the research topic of this thesis. In the first part we will present work based primarily on monitoring extracellular electric activity in various biological tissues including neurons and bacterial cells. We will see how sensors evolved from larger single devices to more sensitive, smaller electronic units consisting of pixel arrays providing high spatial and temporal resolution. We will also present an overview of the CMOS technology used for electrochemical sensing and the ion sensitive field effect transistor (ISFET) and some of the associated support circuitry that is often implemented.

3.2 Ion Sensitive Field-Effect Transistors

In 1970 Bergveld introduced the concept of the Ion Sensitive Field-Effect transistor (ISFET). It was a device similar to a MOSFET but with the metal gate removed and replaced by an electrolytic solution, so it therefore combined ion sensitive electrode technology with solid state electronics [2]. Bergveld measured the drain current and found it to be proportional to the increasing molarity of NaCl solution, which was applied to the device. Later on, Bergveld used his novel technology device to conduct electrochemical experiments using the ISFET as a tool for electrophysiology [10] also embedding additional circuitry for signal amplification. The circuit where this ISFET was implemented can be seen in Fig. 3.1.

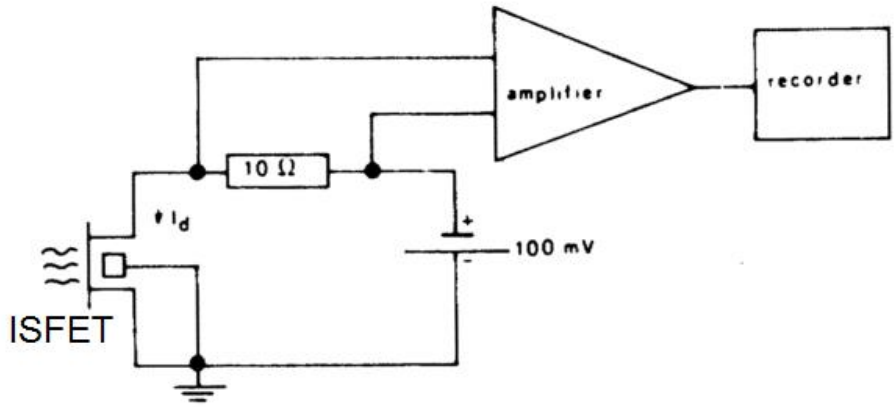

Fig. 3.1: Electronical circuit where the ISFET was implemented

In 1974, Matsuo et al. used an improved version of Bergveld's device with a dual ion sensitive layer of thermally grown SiO_2 and pyrolytically deposited Si_3N_4 [19] shown in picture 3.2a. A 1 μm thick layer of silicon dioxide was also used for insulation leaving a small area as the sensing window. The whole circuitry was connected in a source follower configuration presented as a circuit diagram in Fig. 3.2b.

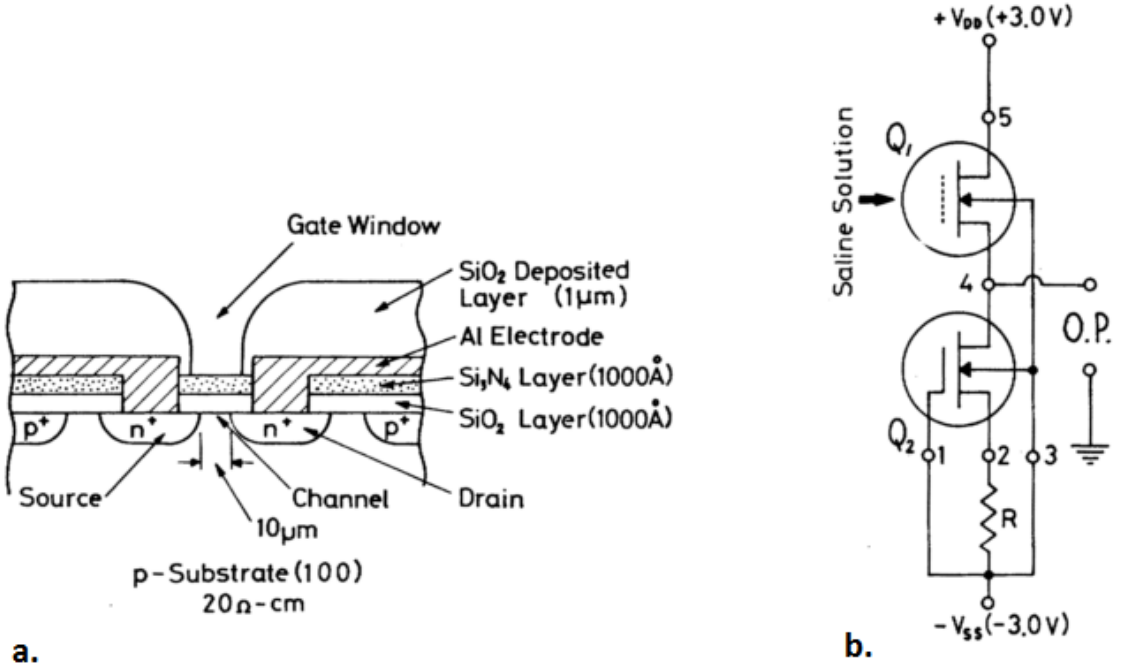

Fig. 3. 2: a. Matsuo's cross-sectional view of the device. b. circuit configuration as used [19].

Focusing on specific ions, Moss et al. used a similar dual layer for building a potassium sensor in 1975 [20]. An extra layer of valinomycin/plasticizer/PVC was added to induce potassium selectivity. Moss emphasized ISFET preconditioning by hydration and considered the use of a reference electrode to be essential. More work on ion selectivity was conducted by Esashi et al. [21]. They fabricated their own ISFET device and focused on sodium ion selectivity. They used an extra layer of aluminosilicate which was deposited by chemical vapour deposition over the existing layer of silicon dioxide and silicon nitride. The additional layer induced a high selectivity in sodium ions. The measured sodium sensitivity was ten times higher than potassium. The principle and cross section of the device is shown in Fig. 3.3.

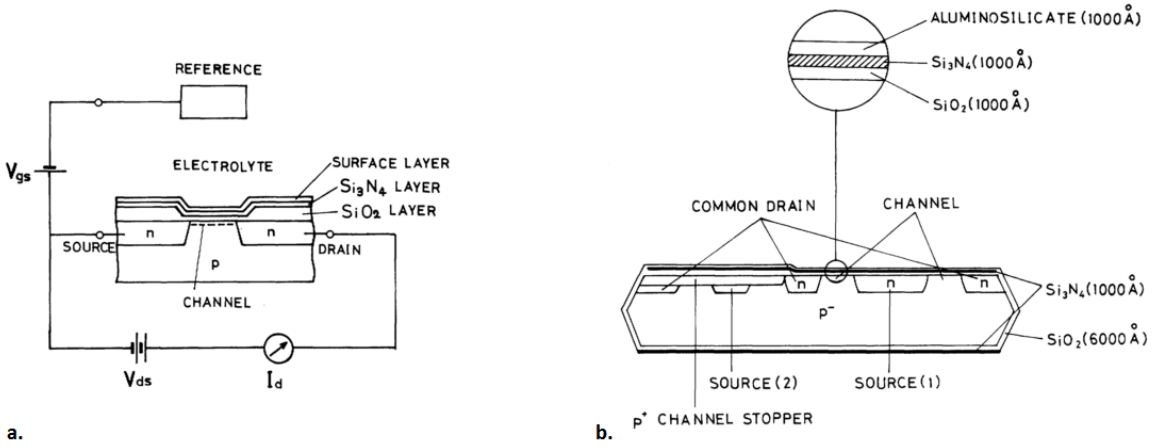

Fig. 3.3: a. principle of Esashi et al. sensor. b. cross-sectional view of the device [21].

Another attempt to achieve selectivity, this time for copper ions, was made from Wakida et al. [22]. They used an additional layer of 7,7,8,8-Tetracyanoquinodimethane (TCNQ) achieving time responses of less than 10 seconds for various ionic concentrations.

3.3 CMOS process Ion Sensitive Field-Effect Transistors

CMOS (complementary metal-oxide-semiconductor) fabrication processes provided a breakthrough that could be applied to the development of the structure of ISFET sensors. This technology led to smaller sizes of sensors on the micrometre scale. The whole process followed the standardised method of MOSFET device fabrication with the appropriate modifications for the ISFET features. A device, where CMOS and ISFET concur can be seen in Fig. 3.4. Bousse et al. [4] worked on a process where CMOS and ISFET circuits were built on the same chip. They used a 2 μm CMOS technology following common fabrication steps for both types of circuit, except for the final metallisation step. They used a tungsten silicide interconnect layer which was resistant enough to temperature variations throughout the deposition processes. ISFETs were constructed with the use of polysilicon floating gates, exposed by photolithographic masking and HF etching before the deposition of the silicon nitride. The use of the polysilicon gate solved the problem of the ambient light sensitivity of the ISFETs. The outer silicon nitride layer of the process acts both as the pH-sensitive layer as also a protection of the on-chip circuitry buried underneath.

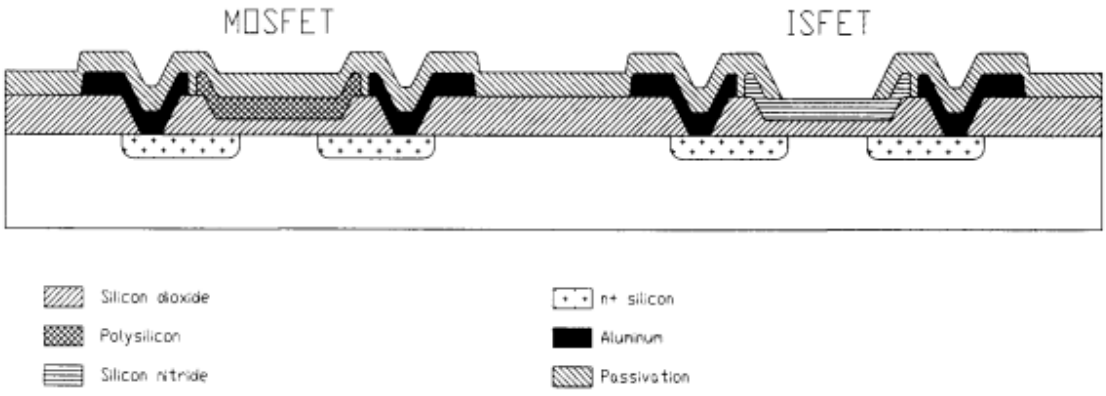

Fig. 3.4: Representation of a MOSFET and an ISFET on the same chip fabricated with CMOS process [23]

Wong et al. [24] implemented another circuit design and managed thus to amplify the signal taken from his ISFET. He matched it with a MOSFET at a differential input stage forming a CMOS operational amplifier which he named 'ISFET-operational amplifier' along with other MOSFETs. The amplifier is further combined with another ISFET-operational amplifier with a different capacitative layer on the gate. The first being a $SiO_xN_y/Si_3N_4/SiO_2$ and the other a Ta_2O_5/SiO_2 layer. With this differential technique they managed to conduct more accurate pH measurements. They accomplished common-mode rejection of the solution potential also to ambient light and noise from the electrolyte. A cross sectional view of their CMOS device can be seen on Fig. 3.5.

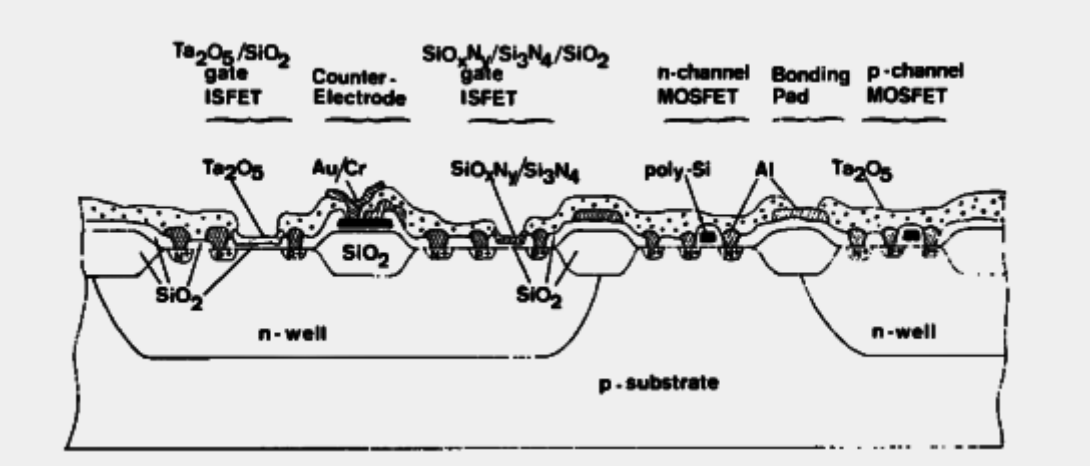

Fig. 3.5: Cross sectional view of Wong et al. CMOS device [24]

Finally, in 1999 Bausells et al. [25] were able to fabricate an ISFET device solely integrated using only a commercial CMOS process. They selected a two metal layer process where the polysilicon gates were connected to the Si_3N_4/SiO_2 passivation layer through interconnection with the metal layers and the vias as shown in Fig. 3.6. The unmodified CMOS process fabrication simplified the circuit design of the devices as computer aided design and simulation was feasible and the characteristics of the design was now fitted to foundry parameters provided by companies using the appropriate microfabrication equipment.

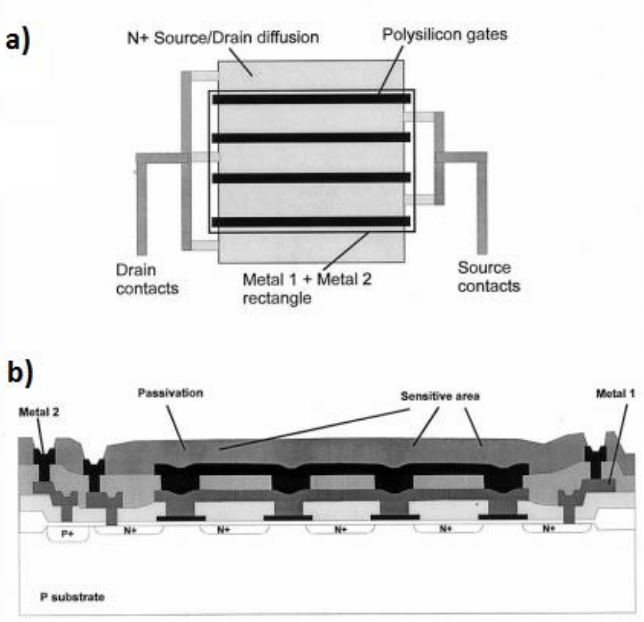

Fig. 3.6: a) top view and b) schematic cross section of integrated ISFET device of Bausells et al. [25]

Lots of inorganic materials have been used which were compatible with ion-sensitive measurements. Literature has plenty examples of membrane deposition on top of the ISFET devices. Table 3.1 presents some of these materials along with their pH range and their sensitivity.

Materials	**pH Range**	**Sensitivity** (mV/pH)	**References**
SiO_2	4-10	25-35	[26]
Ta_2O_5	2-9	59.3	[27]
BN	1.8-10	50-59	[28]
ZrO_2	1-8.5	58	[29]
RuO_2	2-10	52.1	[30]
TiN	4-10	57	[31]
Pt	1-5	25.1	[32]
IrO_x	1.5-12.1	57.1-57.6	[33]
HfO_2	2-8	55	[34]
Si_3N_4	1-13	46-56	[20]

Table 3.1 Materials used for ion-sensitive measurements

3.4 Ion-sensitive sensor arrays

Using a CMOS process for the design and fabrication of the ISFET devices was a big step towards its functionality and utilisation. The scalability and standardised structure of this technology led to the idea of constructing an array sensor. With an ISFET sensor array we are now able to acquire spatial resolution in the form of pixels and thus monitor more complicated chemistry or biology related to ionic solutions. Milgrew et al. [35] using an unmodified standard 0.35 μm CMOS process fabricated a 2 x 2 pixel array of ISFETs. All readout circuitry was also situated on the foundry chip. The chip was exposed to ultraviolet light as soon as it came from the foundry to eliminate any difference in threshold voltage. Encapsulation and waterproof packaging was achieved with the addition of a double layer SU-8 photoresist which was also situated to provide biocompatibility. The circuit provided a sufficient linear range for the ISFETs to act as pH sensors. Cross-section of this CMOS process and a microphotograph can be seen in Fig. 3.7

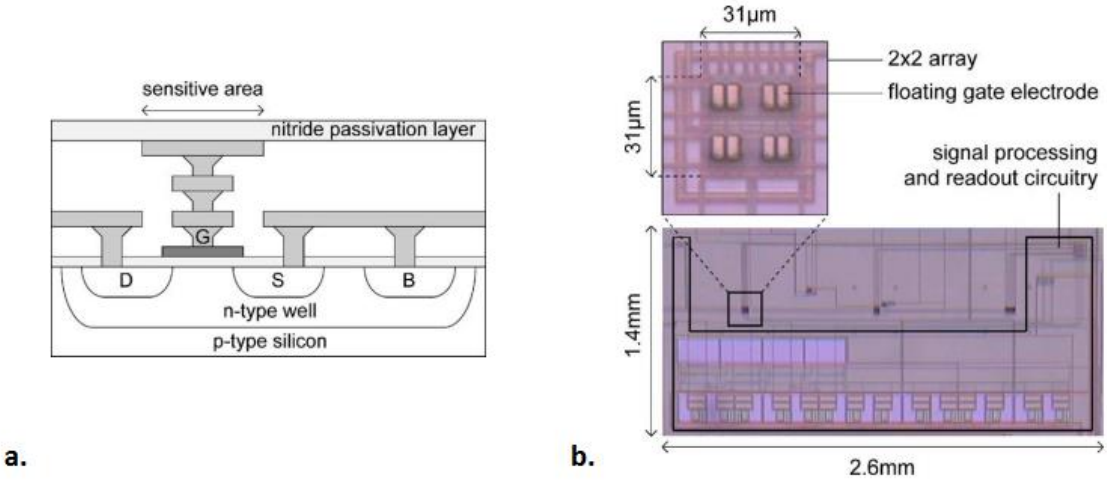

Fig. 3.7 a. cross-section of the CMOS process ISFET used and b. microphotograph of the 2 x 2 array sensor chip [35].

Later on Milgrew et al. upgraded their device by adding more pixel and thus more spatial resolution with the appropriate addressing and amplifying circuitry [36]. With 256 pixels altogether the device was ideal for monitoring biological

activity, so an additional microfluidic chamber made from elastomer was embedded to enable cell culture experiments to be executed. A p-channel transistor was chosen for the ISFET which presented lower noise performance than a n-channel one with a W/L ratio of 1/0.35 μm. The single pixel of the device consisted, apart from the ISFET, of two additional switches. A transmission gate and a simple switch, made by an n-transistor that allowed constant current to flow through the ISFET. The transistors used for the switching also have the same W/L ratio of 1/0.35 μm. For the addressing, two 4-to-16 decoders were used. The analogue signal was then converted to digital through a 10-bit analogue-to-digital converter. Each pixel of the array covers an area of 12.8 μm x 12.8 μm and the entire array is surrounded by a metal frame of approximately 100 μm. As it was observed under the microscope the cell culture was able to grow properly directly above the surface of the chip and remained alive for at least 48 hours. A microphotograph of this device can be seen in Fig. 3.8

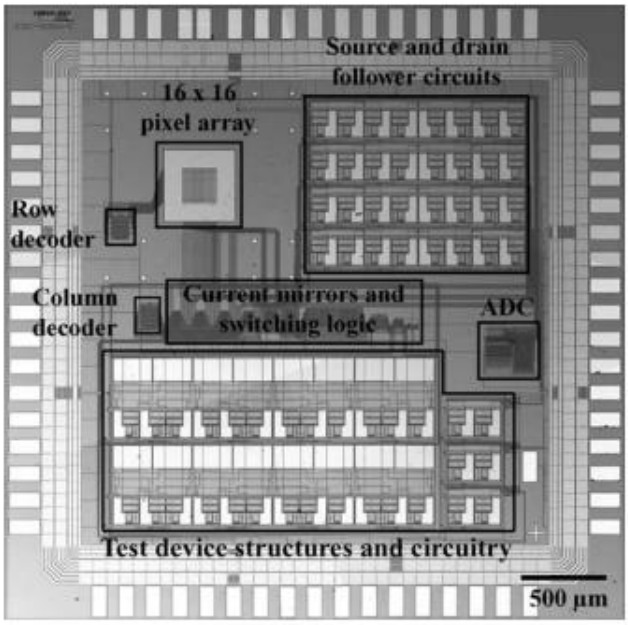

Fig. 3.8 micrograph of Milgrew's 16x16 pixel sensor array chip [36]

More work on the specific chip was conducted by Shields et al. [37] on an attempt to measure liquid diffusion parameters on the chip using a different encapsulation technique (Fig. 3.9a) for the device to be compatible with a Eppendorf Femtojet micromanipulator (Fig. 3.9b) for injecting extremely small amounts of liquids on the surface of the chip. They recorded videos with 333 frames/s frame rate to monitor the pH change induced by sulphuric acid to

normal saline solution and thus estimated diffusivity coefficient values for the interfering analytes.

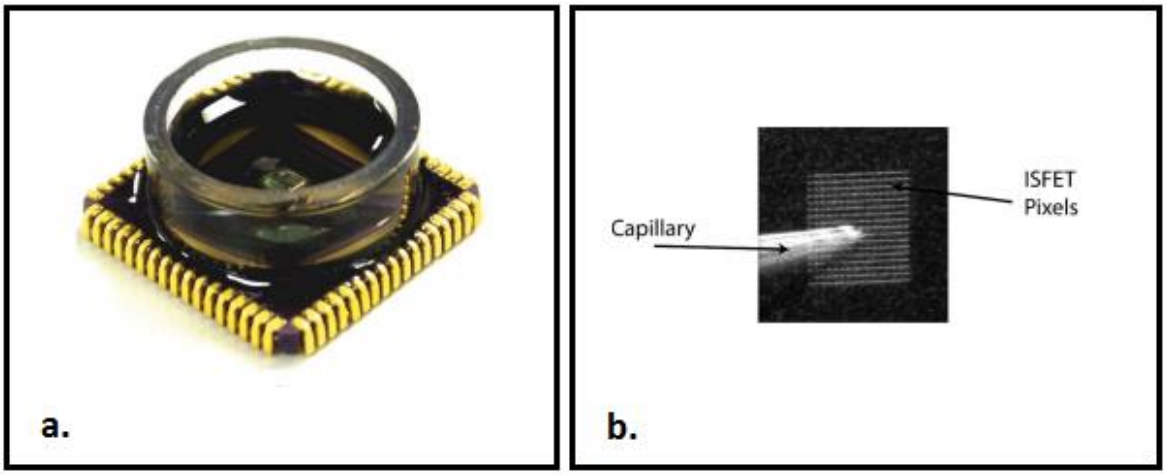

Fig. 3.9: a. packaged ISFET sensor array chip. b. microcapillary of an Eppendorf Femtojet microinjector and the 16x16 ISFET array surface [37].

Later on, Hassibi et al. used a 0.18 μm CMOS technology in order to create a multisensor capable of performing ion-sensitive, amperometric, voltammetric and impedance measurements [5]. The device consists of 5 x 10 pixels, counter and reference electrodes and an appropriate amplifying circuitry. Each pixel covers a 160 μm x 120 μm area. Due to the nature of the measurements –i.e. mostly biochemical, this array was not easily reusable.

ISFET arrays were also used in genome sequencing. In 2011, Rothberg et al. [38] presented their array consisting of millions of pixels of ISFETs (Fig. 3.10). They used tantalum oxide metal as the sensitive layer and the sensitive wells onto the pixels were only 1.3 μm wide providing extreme spatial resolution. This was the first time that DNA sequencing was conducted with CMOS technology and not with the conventional light spectroscopic method, opening the road for measurements based on scalable technology.

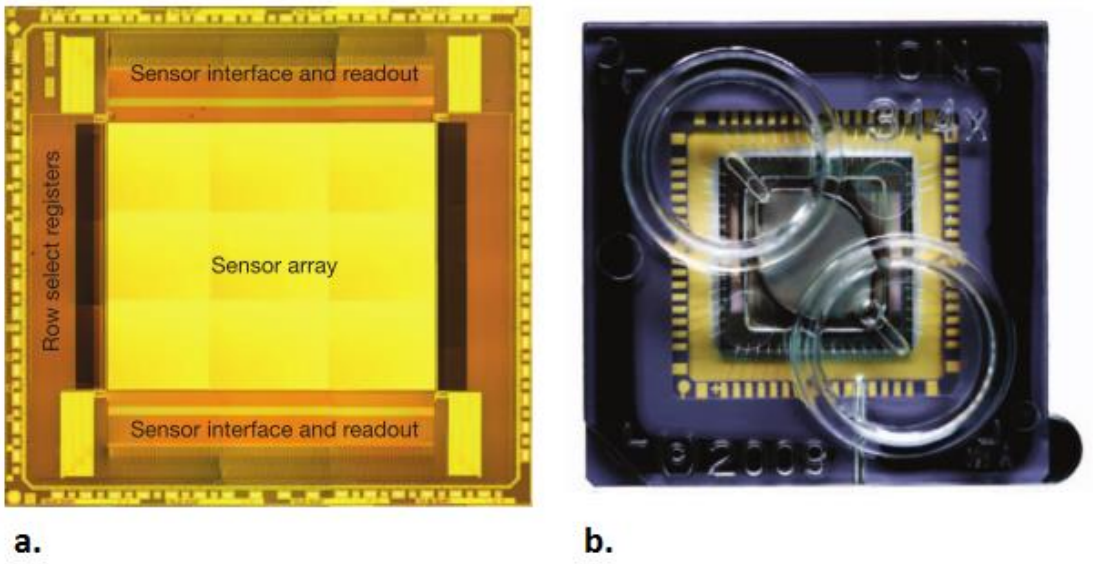

Figure 3.10: a. unpackaged chip from Rothberg et al. with all areas indicated. b. the chip is packaged and wire bonded for electrical connection. A special lid was embedded on top to enable the addition of sequencing substances [38].

3.5 Bacterial ISFETs and Enzyme ISFETs

3.5.1 Bacterial activity detection

A significant amount of research has also been conducted concerning the detection of bacterial activity with ion sensitive sensors. Bacteria can be an excellent assay to study metabolism, gene sequencing and even photosynthesis if the specific phylum of cyanobacteria is monitored. Pourciel-Gouzy et al. [39] built an ISFET microsensor for the detection of Lactobacillus Acidophilus a bacterium that occurs naturally in the human gastrointestinal tract and ferments sugars to lactic acid. The sensors were packaged in micro-tanks made from plexiglass or poly-dimethylsiloxane (PDMS). The addition of glucose in the solution initiated the production of lactic acid and lowered the pH. The packaged device can be seen in Fig. 3.11.

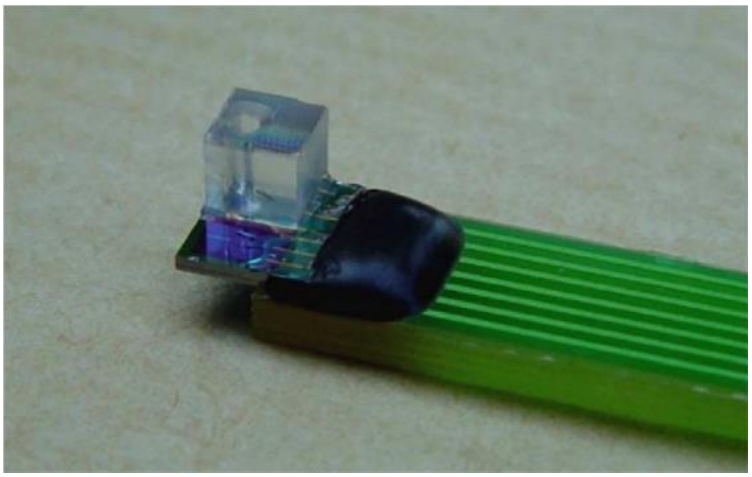

Fig. 3.11: ISFET chip packaged with a plexiglass micro-tank to control small volumes of bacterial solutions [39]

In their work, Castellarnau et al. [40] moved a step further and engaged integrated dielectrophoretic microelectrodes to successfully position the bacteria on top of the sensor. The bacterial activity was monitored by the addition of glucose which lowered the pH of the solution. An image of the fabricated ISFET with the embedded dielectrophoresis microelectrodes and the reference electrode can be seen in Fig. 3.12.

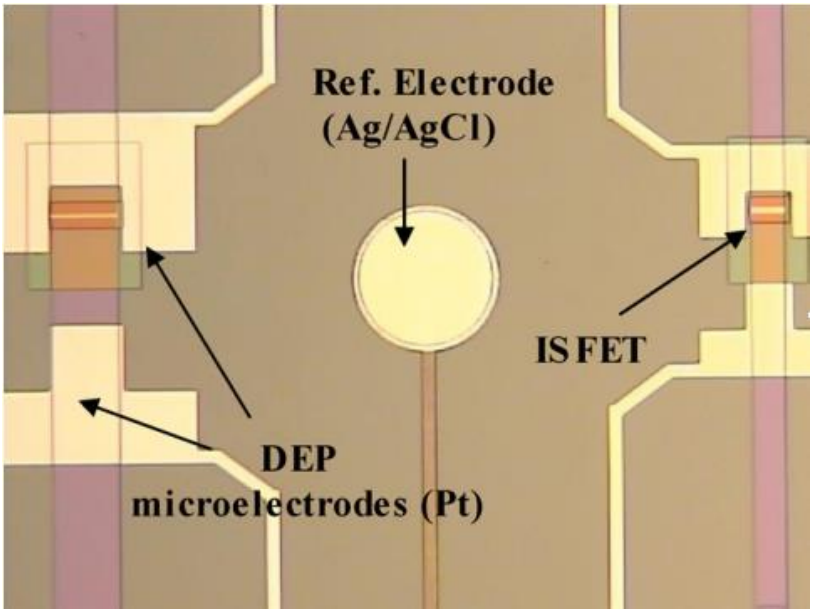

Fig. 3.12: image of the device with the ISFET sensors, dielectrophoresis microelectrodes and reference electrode [40].

3.5.2 Enzyme biosensors

Enzyme ISFET sensors are mainly sensor devices that operate with an extra sensitive layer of an enzyme, each time appropriate for a related ionic reaction. Immobilization of the enzyme is always a challenge for these methods and there are a big variety of enzymes that can be used for various fields of biomedical research. Van der Schoot and Bergveld [41] used an ISFET with an extra layer of albumin and urease on top of an extra tantalum pentoxide layer as seen in Fig. 3.13(a). The device presented significant sensitivity with the gradual addition of urea in the solution as seen in Fig. 3.13(b).

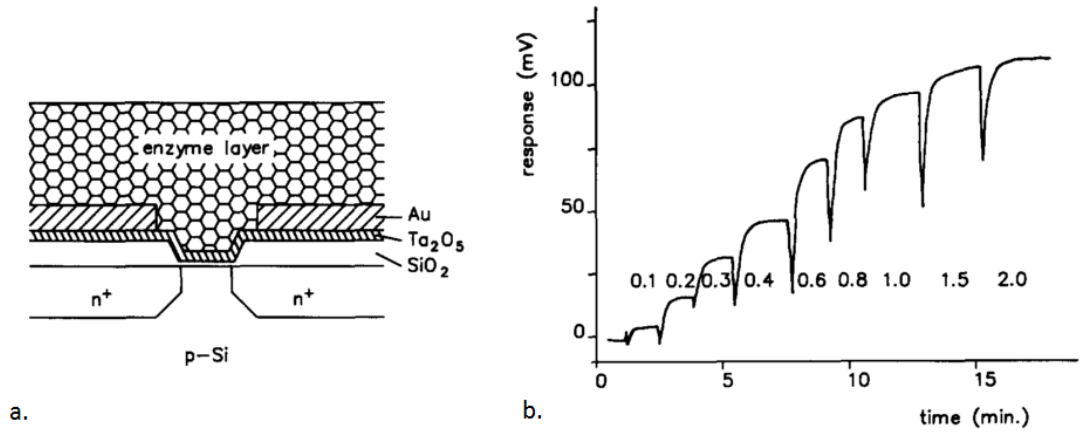

Fig. 3.13: a. cross-section of the enzyme sensor. b. time response of the urease/albumin enzyme ISFET. The numbers on the curve indicate the added urea concentration in mmol/litre [41].

Xi-Liang Luo et al. [42] in 2003, developed another Enzyme ISFET (also called ENFET) with an extra enzyme layer but this time doped with SiO_2 nanoparticles which exhibit good biocompatibility (Fig. 3.14). Indeed their experiments enhanced the ENFET's sensitivity and lengthen the device life time producing more stable and reproducible techniques which can be used for glucose detection.

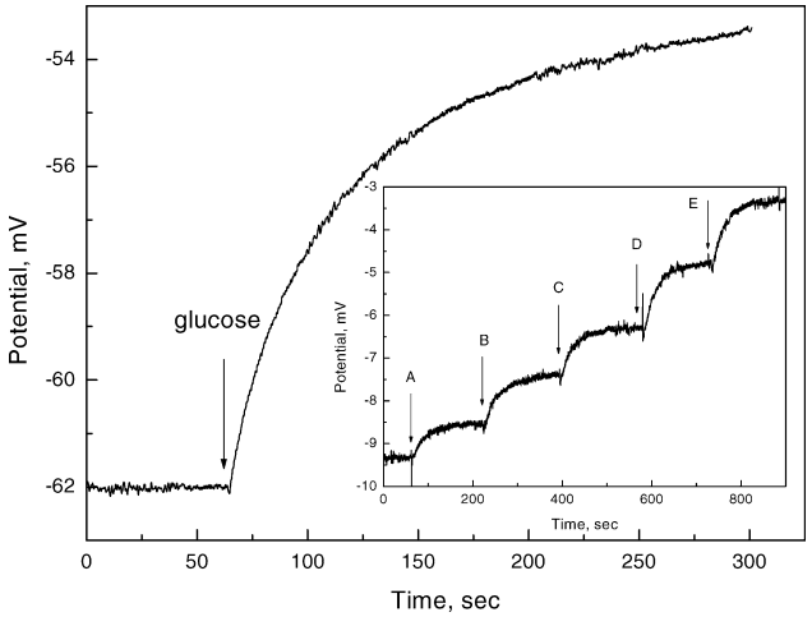

Fig. 3.14: time response of the enzyme ISFET in response to 1.0 mM glucose in 10 mM PBS, containing 100 mM NaCl. Inset: time response of the ENFET to gradual additions of glucose [42].

In 2002, Park et al. [43] fabricated an ISFET sensor with a silicon nitride-tantalum pentoxide sensitive layer and an extra enzyme-immobilized membrane for glucose detection. The glucose of the solution is converted to gluconate releasing hydrogen ions detected by the enzyme-immobilized membrane.

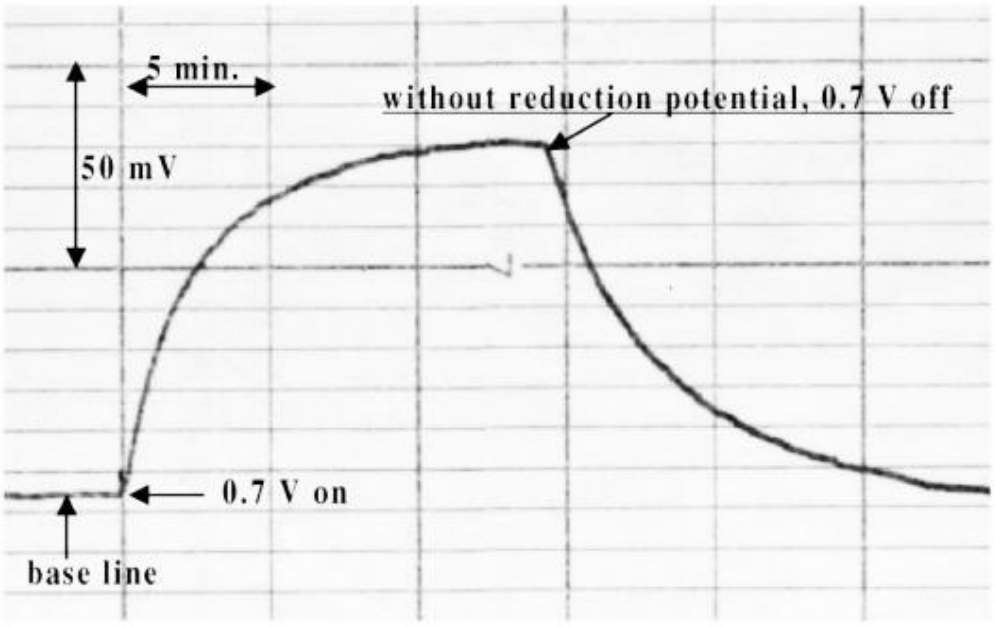

Fig. 3.15: Time response of Park et al. ENFET during a glucose reaction [43]

As seen in Fig. 3.15 they obtained a signal of 85 mV caused by proton interaction with the enzyme-immobilized membrane.

3.6 Cyanobacterial monitoring of light depended activity

Regarding bacterial activity detection, Bombelli et al.[44] in 2012 used cyclic voltammetry to detect ionic behaviour of *Pseudanabaena limnetica* a cyanobacterium found in fresh water. Their device consisted of an anode made from indium tin oxide-coated polyethylene terephthalate where the cells were inoculated. The cathode consisted of carbon paper, coated with a layer of platinum. Representation of this structure can be seen in Fig. 3.16

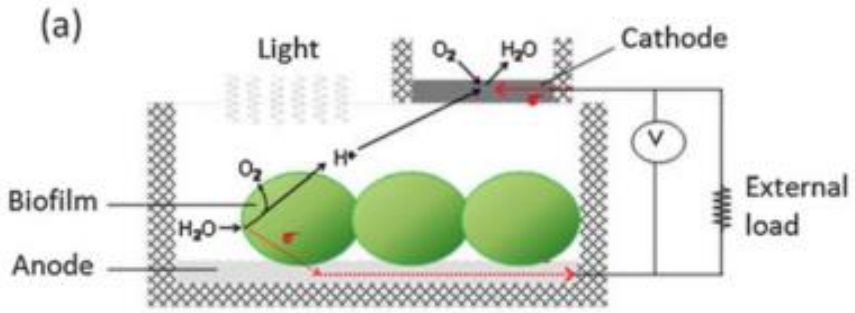

Figure 3.16: Schematic representation of Bombelli's device for cyanobacterial activity monitoring [44].

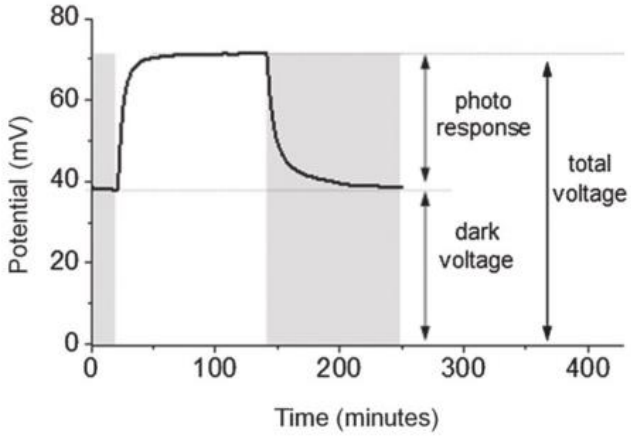

Figure 3.17: Voltage response of Bombelli's device during light-off light-on intervals

Figure 3.17 shows the voltage response of the device during light-off and light-on intervals. The voltage difference detected between them was reported to be 33.7 mV.

3.7 Summary

The literature review is a short history regarding the ISFET array technology and how it is linked to our research. Bergveld was the first that come up with the idea of the ion sensitive transistor devices just by removing the gate from the transistor and instead adding an aqueous solution. Matsuo et al. was the one who established the dual sensitive layer of silicon dioxide and silicon nitride wich was studied also on this thesis theoretically (Chapt.2) and used in our foundry (Chapt. 4). Moss et al. used the sensor to measure potassium ions, which we also tried in Chapt. 5. Wakida used it to measure copper ions by adding additional layers, an idea we used in chapters 5, 6 and 7. Bousse embedded the ISFET with CMOS technology and Bausells fabricated an ISFET using a standard foundry CMOS two-metal layer process. Milgrew et al. used the 0.35 μm technology, the same we used and made an array of ISFETs. Pourciel-Gouzy used the ISFET to monitor bacterial activity and the devices Van der Schoot, Xi-Lang and Park were fabricated to detect enzyme reactions. Using a different approach, but interested also in bacterial and enzymatic behaviour we were also interested in enzymatic and bacterial experiments with ISFETs and additional layers. Chapters 6 and 7 are dedicated to this direction of research.

3.8 Conclusion

In this chapter we examined briefly the early devices used for potentiometric measurements and selective electrodes and their biomedical applications. We then moved to the study of microelectrodes and microelectrode arrays which were capable of monitoring neural activity of living tissue in vitro. Then we moved to the ion sensitive field-effect transistors which opened a new path on measuring pH and ionic activity in solutions. With CMOS process engaged in ISFET fabrication, this technology became scalable and more accessible giving way to

more complicated experiments involving extra sensitive layers and enzyme layers for specialised biosensing. ENFETs and bacterial ISFETs were also briefly examined, due to their relation with the experimental part of the present thesis.

4. The 64x64 pixel sensor array system

4.1 Introduction

This chapter describes the design of the 64x64 pixel sensor array system by going through all stages of the design process. This working chip has been designed previously by Balazs Nemeth during his PhD. The first stage describes the technology used and the design of the analogue circuit of the sensor array. Then additional amplification and digital addressing circuitry was designed to be embedded on the main ISFET array. These parts describe the basic components of the chip that was sent to foundry for fabrication. Also, an external Printed Circuit Board (PCB) was designed and fabricated to enable the chip to communicate with the external power supply and the data acquisition devices. The chip is placed on an appropriate carrier which provides connections to the PCB. The chip is bonded on the carrier and then encapsulated leaving the active parts open and insulating the bonding wires in such a way that the chip is able to interact with aqueous solutions without danger of short circuit. We will examine all these steps in the following paragraphs in detail.

4.2 CMOS technology used

For the 64 x 64 ISFET array device the austriamicrosystems AG foundry [45] was selected, also known as AMS using the HIT-Kit v3.70 design kit. C35B4 is the CMOS process we used, with four metal layers and a feature size of 0.35 μm. The cross sectional view of this technology can be seen in Fig. 4.1. The four alloy metal layers are interconnected with vias made of tungsten alloys. The structure is divided into different levels that are insulated by oxide layers. On the top surface there is a passivation layer to prevent the device from oxidation.

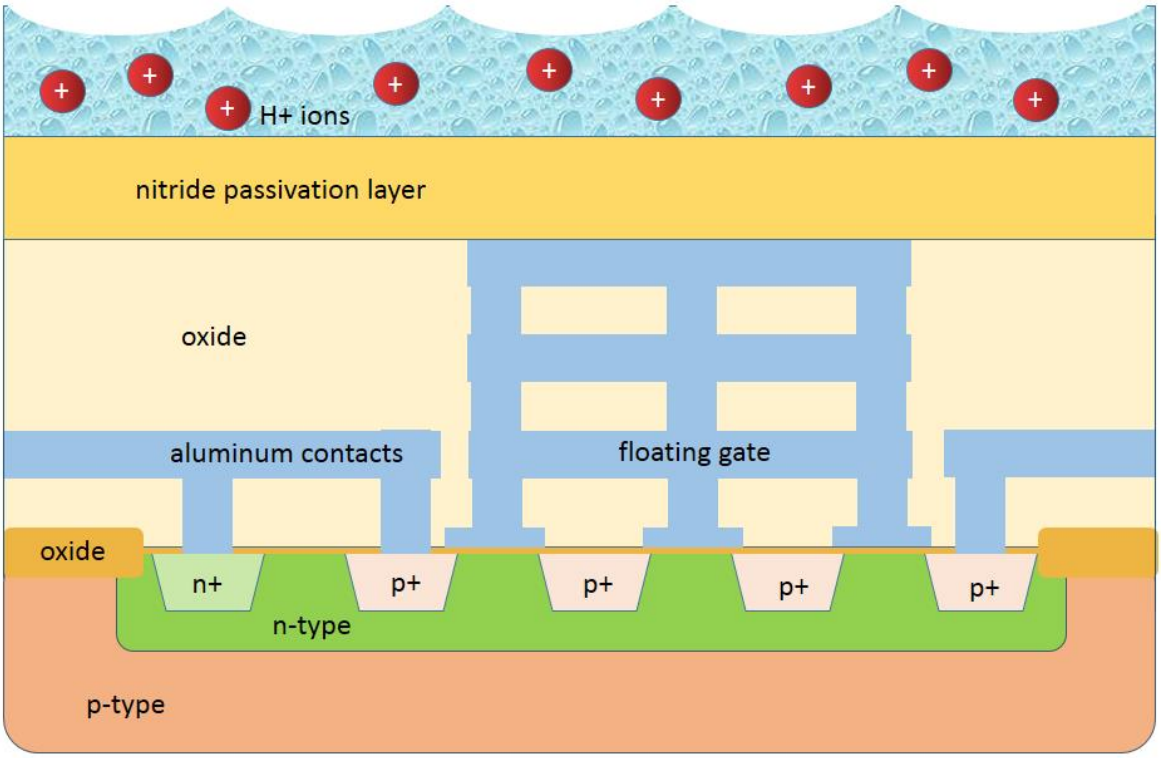

Fig. 4.1: Cross-sectional view of the ISFET using AMS 0.35μm C35B4 foundry. Image not to scale

4.3 64x64 pixel ISFET array chip

In this section we analyse all components of the array chip; the pixels, the amplifying circuitry, the digital addressing and their interconnections. The 0.35 μm technology we used enabled us to design the 4096 ISFET pixels using the complexity of its four metal layers and also use the passivation layer as the sensitive layer that characterizes the ISFET devices. Single pixel, pixel array and complementary amplifying and digital circuitry are described in the following sections in detail.

4.3.1 Pixel

The pixel is the fundamental element of our design. It is basically an ion sensitive transistor along with other transistors used for addressing. The whole pixel circuit consists of four transistors as seen in Fig. 4.2a. P2 is the ISFET p-type transistor, P1 is another pMOS transistor and P3 with N1 are pMOS and nMOS transistors respectively which stand for the transmission gate circuitry. P1 pMOS

has a double role in our design. Firstly, it behaves as a current source, providing the ISFET transistor with a 16 μA current load during the array readout. Secondly, as regards to addressing, P1 has the role of row addressing the array also as its V_{row} gate voltage switches from 1.2V to power potential. P2 is our ISFET transistor reaching out through the passivation layer and it is able to sense concentration differences for cations in the aqueous solution. Transistors P3 and N1 which are the transmission gate provide exclusive access to the pixel for column addressing while array readout. In Fig. 4.2b we can see the layout of the chip. Row addressing and column addressing routing is made with thicker lines and the ISFET transistor's gate is connected to poly and this connected further to MET 4, which is the top metal layer of this technology going through all vias and metal layers. Further, MET 4 is in direct connection with the technology's passivation membrane which is the active membrane of our ion sensitive device.

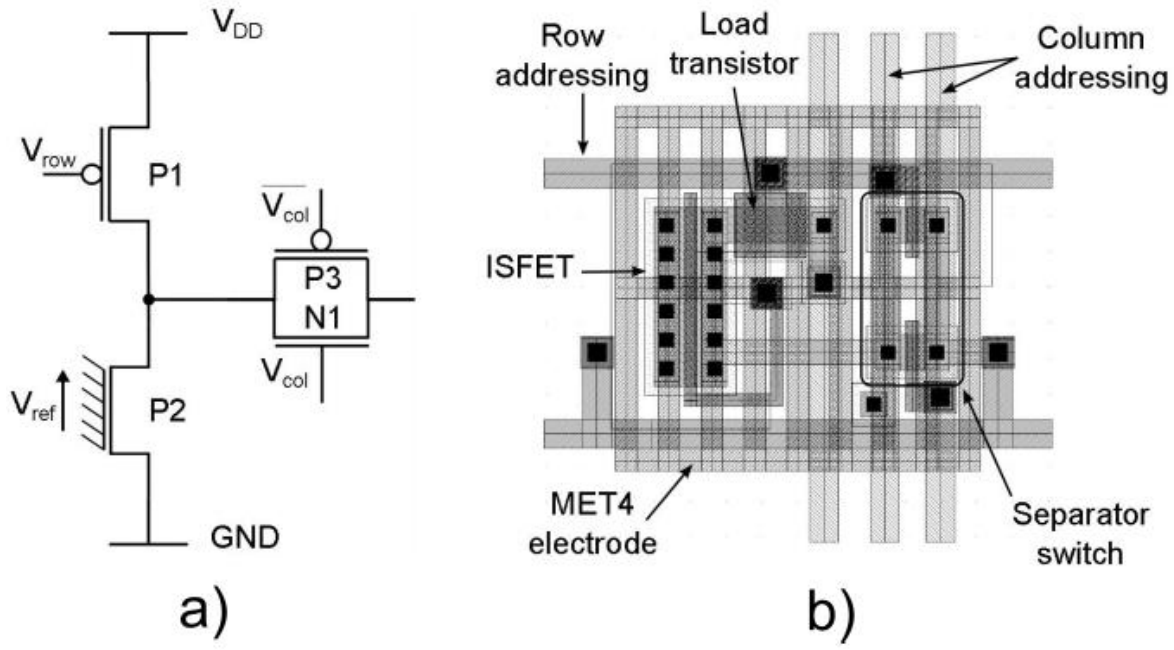

Fig. 4.2: a. Schematic representation of the ISFET pixel circuit b. layout representation of the ISFET pixel circuit [1]

The dimensions of the transistors of the pixel are $W_{P1}/L_{P1} = 2\mu m / 1\mu m$, $W_{P2}/L_{P2} = 5\mu m / 0.35\ \mu m$, $W_{P3,NI}/L_{P3,NI} = 2\mu m / 0.35\ \mu m$.

4.3.2 Addressing digital circuitry

Apart from the 64x64 ISFET array design, our chip is equipped with extra digital logic circuitry for addressing and sequencing. Vertical addressing is performed by using a 6/64 decoder circuit shown in Fig. 4.3a. The decoder receives the 6-bit digital code from the

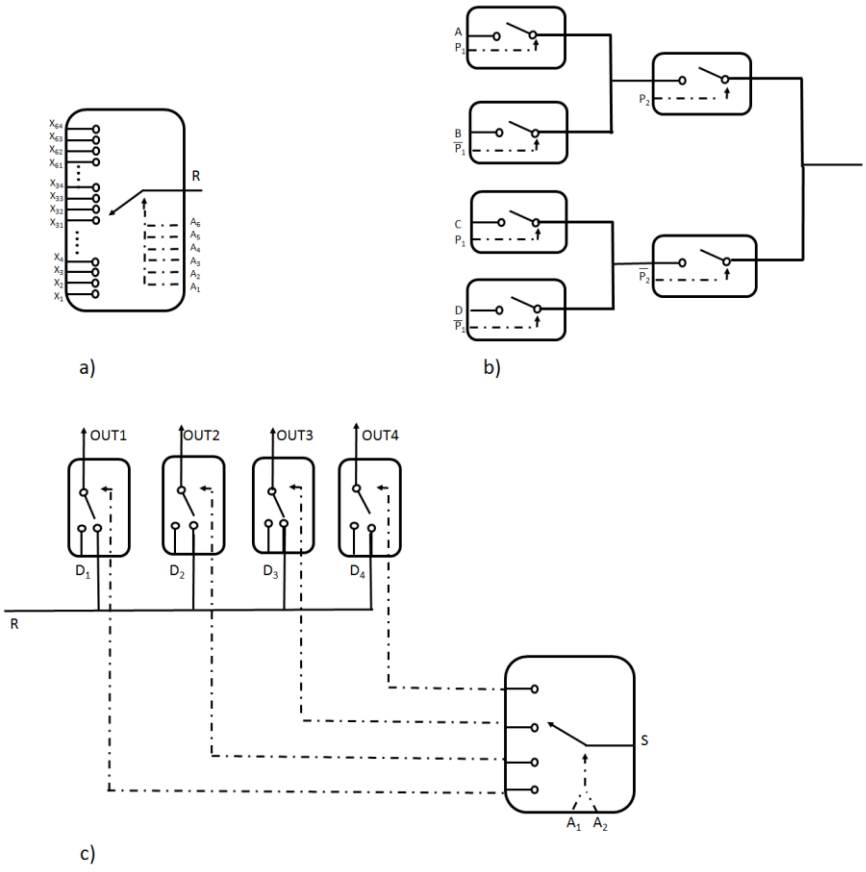

Fig. 4.3: Digital circuitry for addressing on the ISFET array chip. a) 6/64 decoder, b) 4/1 multiplexer and c) 1/4 demultiplexer

power supply of the selected column of the array connecting the potential of the chosen output to GND. The input digital code is ascending from 000000 to 111111 in equal time steps so as each column from 0 to 63 is selected in

sequence. Horizontal addressing is performed by a 4/1 multiplexer shown in Fig. 4.3b. It is used to connect the appropriate row with the output buffer amplifiers of the chip addressing the rows sequentially. The demultiplexer shown in Fig. 4.3c is receiving the same signal for row addressing as the multiplexers. Its operation is to activate the selected line while the multiplexer leads the analogue voltage readout values to the output buffers of the chip.

4.3.3 The ISFET array

The array consists of 4096 single pixel blocks as seen in the previous paragraph, in a 64 x64 square array. Each single pixel of the array is identical to the others. The array is divided into 16 separate sections as seen in Fig. 4.4. Each section consists of 4 rows of the array. Dividing the array into 16 sections proved to be beneficial for the data readout as it accelerated the whole process. With this division data were read in parallel mode saving time and achieving faster time resolution. A 4-row block of pixels contains 256 sensors and it can stand at its own. Each block like this is connected to a multiplexer and a demultiplexer, so 16 multiplexers and 16 demultiplexers are situated on the side of the ISFET sensor array. More specifically, all the four gates of the P1 transistors -shown in the schematic of Fig. 4.2- of a block are connected to a demultiplexer's output terminals. The demultiplexer by altering the control potential of transistor P1 activates or deactivates a whole row at once. In a similar way, the outputs of the rows are also connected with the inputs of the multiplexers.

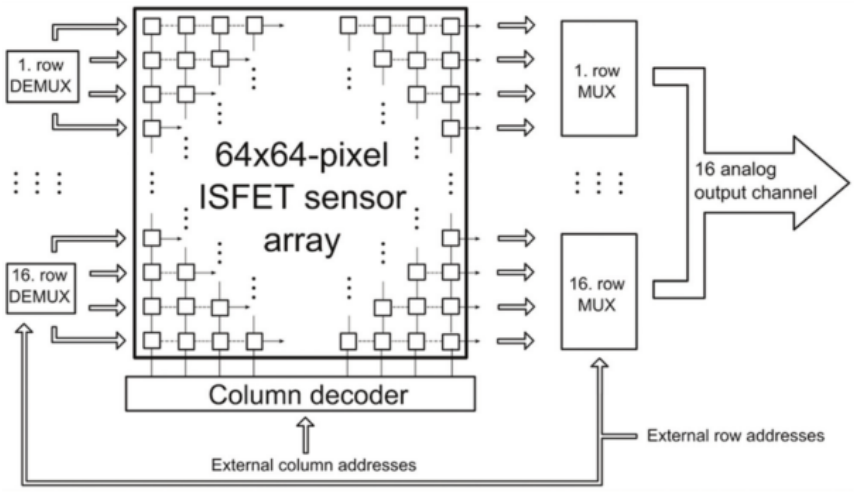

Fig. 4.4: Diagram of the digital addressing of the ISFET array [7].

We can see all the images of the fabricated ISFET array, Metal 4 ring around the array in Fig. 4.5. The whole array covers a square space of 715.8 µm x 715.8 µm. Also in Fig. 4.5a. we can clearly see the pattern of the top metal for each pixel. Fig 4.5b shows us the complete fabricated and bonded chip. The sensor is located at the centre of the chip that makes encapsulation and measuring easier, which we will discuss later. Chip is glued on a chip carrier and bonded to the associated pins.

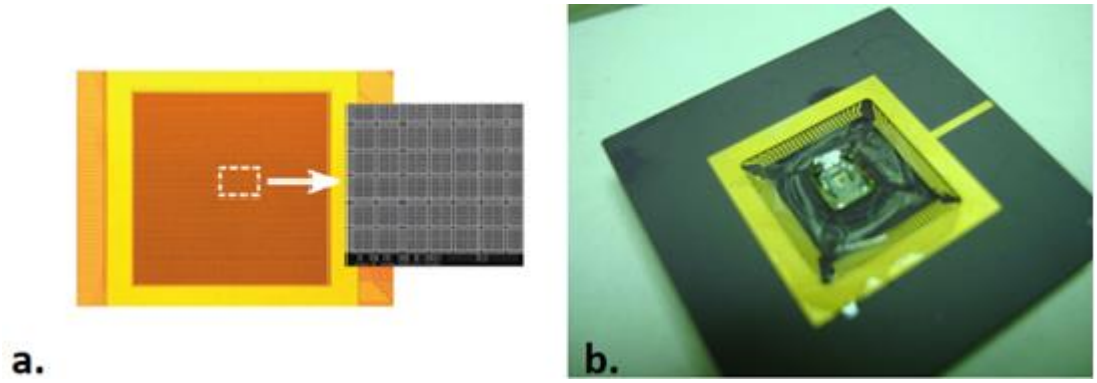

Fig. 4.5: a) Optical microscope photograph of the array and zoomed electron microscope picture of the patterned metal 4 surface [6]. b) packaged and bonded chip.

4.4 Chip layout and external electronic circuitry

The layout of the sensor array chip was designed with the use of Cadence designing environment and also the use of HIT-Kit v3.70 design kit provided by austriamicrosystems. Complete architecture of the 64x64-pixel array chip can be seen in Fig. 4.6. With all components, chip covers an area of approximately 4.4 µm x 4.3 µm. It uses 95 I/O pads in the 3-bus padring. It has double power and double ground terminals –to provide a backup if one is malfunctioning- each one covers a width of 75 µm using MET1 and MET2. All chip components discussed in previous paragraphs can be seen in Fig. 4.6.

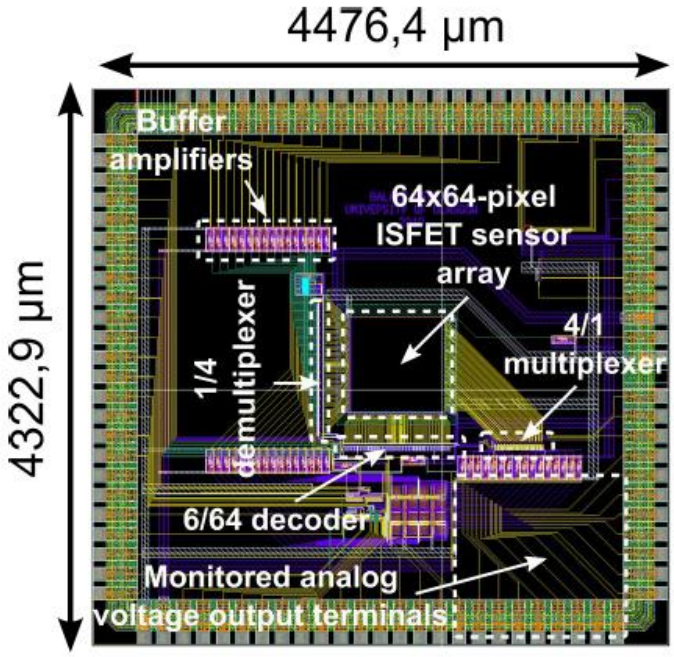

Fig. 4.6: Physical layout of the 64x64-pixel ISFET Array chip [46].

Connection between the chip and a computer was important to achieve control and to monitor the ISFET device processes. The need of an interface board between these two was essential to access data acquisition hardware and also power supply and ground. For that reason a Printed Circuit Board (PCB) was previously fabricated to provide us with this interconnection. Grounding the board was very important during experiments, so all ground cables and areas were connected to a common ground. Small Computer System Interface (SCSI) connectors on the PCB provided connection through the appropriate cables with the data readout device. SCSI connectors on the board along with BNC connectors were used for the external power supply. Two different BNC connectors were used on the board, one for power supply associated with the digital circuitry and one for the actual analogue part going from 0 - 5V and 0 – 3.3V respectively. The PCB interface used was fabricated in the PCB service of the PCB Train-Newbury Electronics Ltd. This two layer fabrication was made by using 1 oz. of copper with silver immersion finish and a minimum track gap of 0.2 mm. Fig. 4.7 shows the final version of the PCB used for the experiments.

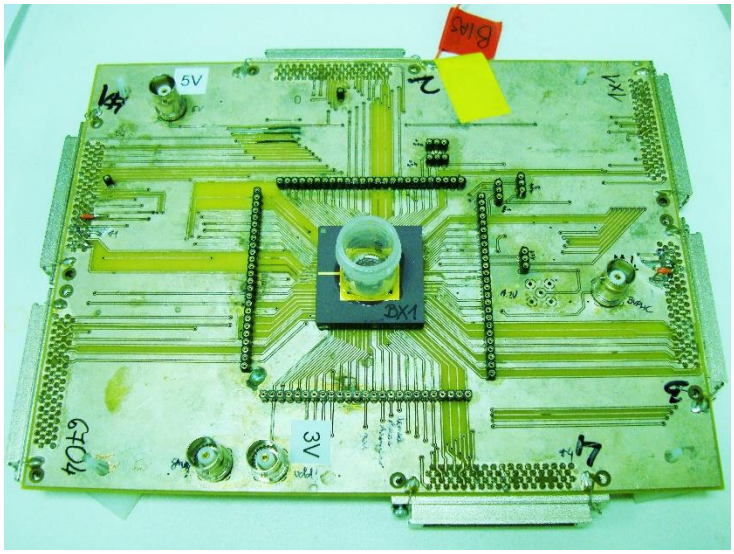

Fig. 4.7: Final version of the Printed Circuit Board (PCB) used for our measurements

4.5 Packaging and encapsulation

The aqueous solution is required to be in contact with the ISFET array core of the chip, but all other electronic parts should be shielded and protected. The choice of a robust and stable encapsulation technique is crucial for normal operation of the chip device. Special consideration must be given to the bond pads: they need to be strongly insulated from the aqueous solution but also insulated between each other to prevent short circuits of the device. Normally the encapsulant is a two-part liquid which has to be mixed appropriately to ensure the optimal sealing. The second part of the encapsulant regulates the viscosity of the mix and finally cures it to a solid volume. Regulating the viscosity and the curing process is essential during the encapsulation process because there are certain parts of the chip that need to be covered and others that need to be accessible to the environment. A less viscous mix can result in an uncontrolled covering of the area of the chip which would lead to a non-functional device. So the encapsulation was something that had to be mastered as a special technique. In addition to the appropriate mixing, it was necessary to work in a very small area using materials with different surface tension.

After trying different types of encapsulants, we concluded that the Epotek 302-3M epoxy was best suited for this work. This two-component epoxy is colourless with low viscosity and a short curing period. Transparency of the epoxy was a highly favourable property, as it ensured that we could detect any faulty wiring, short circuit or corrosion happening on the chip surface. To assure that the epoxy wouldn't flow over the array surface during application, we placed a barrier around the array. A general purpose silicon rubber sealant from Geocel Ltd, was applied circumferentially without touching any array pixels, bond pads or wires. The sealant was applied from a small pipette continuously to prevent any breaks or stops. The application method was crucial because any leakage or discontinuity on the sealant would result in bad epoxy packaging at the later stage. On most of the occasions, the sealant was left to dry for a couple of hours and then another square shape was applied on top of the first one to make the barrier taller. Another thing worth noticing is the size of the square. If the square is too small, it is possible to trap air bubbles during the measurements, so no solution can reach the array.

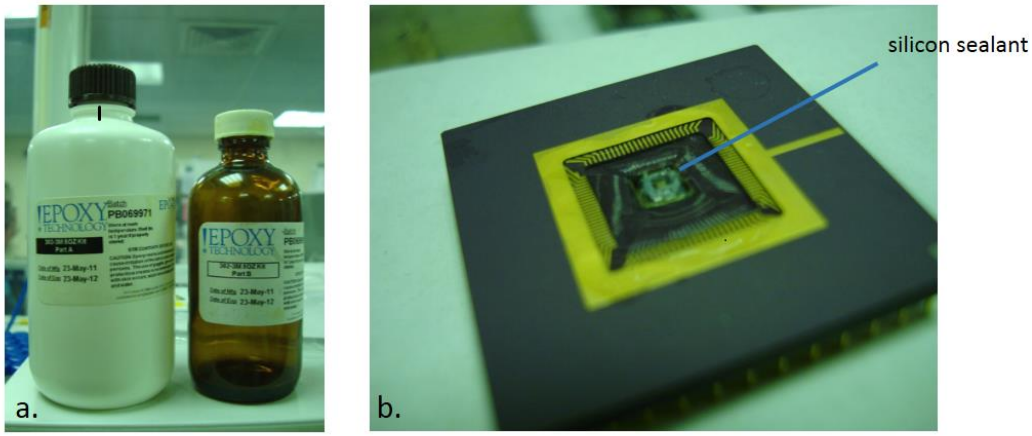

Fig 4.8: a. two-part epoxy encapsulant Epotek 302-3M. b. bonded chip encapsulated and with the additional silicon rubber sealant added for protection of the array.

After applying the silicon sealant, we need to apply the epoxy over the rest of the free space of the chip. We need to cover the bond pads the bonding wires all the way to the pin outputs and any space on the chip till the silicon barrier. If we look closely, the bonding wires form an arc shape, so extra attention is need not to leave parts uncovered as the epoxy is spread. Usually we spread the epoxy on two or even three doses, waiting for the previous one to dry. Curing

time is approximately 24 hours for room temperature and 3 hours for 65 ºC. Although the chip's originator (Balazs Nemeth) used the 65 ºC method, we preferred the room temperature method, because slow drying led to more robust chips.

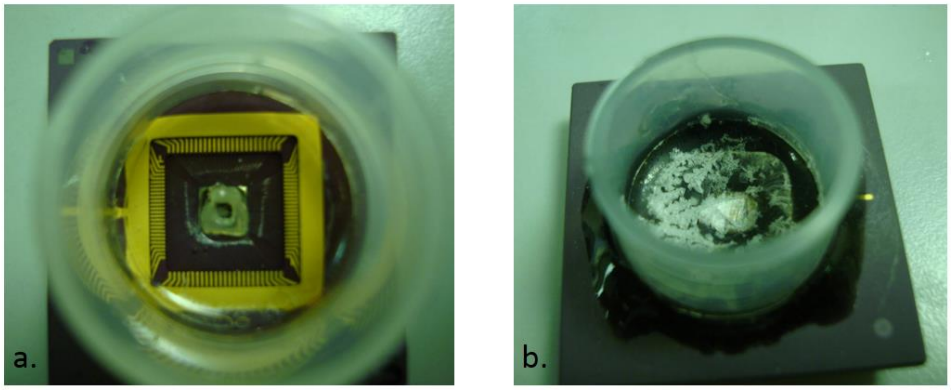

Fig 4.9: Errors in encapsulation. a. very small chamber formed by the silicon sealant which prevented the solution from be applied normally b. poor encapsulation can create leakage of the solution and different chemical residue can damage the chip surface.

After the epoxy dries, the chip looks like the one in Fig. 4.8b. The only thing missing for a complete packaged chip is the addition of the reaction chamber: a small transparent and cylindrical plastic component which acts as a container for our solutions. This chamber is positioned in such a way, that the array sensor in the centre is exposed. Then, epoxy is spread carefully with a pipette through the external and internal sides of it and thus gluing it on the chip's surface. We used two different types of cylindrical plastic in our experiments as shown in Fig 4.10. In Fig. 4.9 some errors in encapsulation are also presented. Bad application of the silicon sealant or poor encapsulation creating problems for the solution distribution on the surface or leakage and shortcircuit of the electronics. We concluded that using the cylindrical plastic component shown in Fig 4.10b was best suited for this experiment, as it is more focused on the sensory area. Also the smaller size of the container gave us the convenience to monitor samples through microscopes or work with micromanipulators.

a. b.

Fig. 4.10. Reaction chamber embedded on the chip. a. big plastic container used in initial experiments b). smaller container more focused on the sensory center and compatible with microscopes and micromanipulators.

Applying the sealant was a very delicate process. Although it could be possible with naked eye, most of the time we encapsulated the chip with the use of an optical microscope using of pipettes and micropipettes. Usually the first, and thicker, layer of the epoxy was applied with the use of disposable pipettes and then the remaining thinner layers and various gaps were filled with the help of micropipette tips. Screenshots of the encapsulation can be seen in Fig. 4.11.

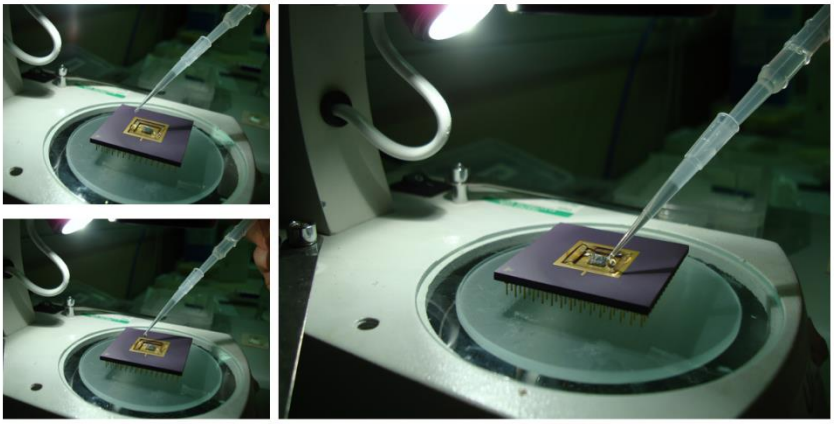

Fig. 4.11: The epoxy is applied on the chip mainly at the edges and let to flow carefully reaching the silicon sealant barrier. After drying more epoxy is applied to fill any gaps and abnormalities.

Special care was taken where the bond wires had to be insulated. The wires were curved, so they formed an elliptical bridge between the pads and the chip.

We had to be sure that the whole structure was covered with epoxy to avoid a short-circuit. Again, in some cases we had to wait for a first layer of epoxy to dry before applying a second or third one.

The epoxy drying process can be done in two ways. We can other dry in a high temperature around 65 °C or we can leave the chip in room temperature to dry and wait for 24 hours. In our packaging, we preferred the 24-hour room temperature dry process that provided us with more robust packaged products.

Many different approaches were used to ensure the best application of the encapsulant over the array. Most of the already used methods were optimized or differentiated in order to achieve better sensitivity and longer life of the chip.

A critical point had to be achieved first for the size of the silicon sealant square. It has to be close enough to the array, but not as close as to favour bubble formation due to surface tension on it (Fig. 4.9), but not as far as to touch the bond pads and the bonding wires because its viscosity could damage them. The sealant was applied carefully under the microscope in the same manner of a toothpaste on a brush avoiding bubbles and gaps to form. The sealant square was formed by two 'brushstrokes' of the sealant in the sape of two 'L' s. We had to pay extra attention where the 'L's were connected to form the square so as not to leave any gaps and maintain the same height of the silicon barrier.

The epoxy was applied slowly having a medium viscosity in order to cover all bond wires and leave no bubbles. To achieve that few droplets were poured from one side at a time giving some time for the epoxy to spread, so four times in total. As before, when dried it was examined again under the microscope and more epoxy was applied in the same manner if needed.

For the reaction chamber we concluded using a smaller diameter pipe (Fig. 4.10b) instead of the initial one used (Fig. 4.10a), enabling us to use less solution quantity each time for our experiments. Also the height of the chamber was decreased covering thus less space when it had to be used under specific microscopes. Smaller size in general, especially in height made the device more versatile for any future use.

These packaging modifications increased the chip's life significantly compared with the previously packaged chips. Most of them were only used once or twice

and then stop functioning. With the optimized encapsulation methods chips were able to go at least for 4 or 5 measurements, depending of course on the layers used and some of them were used for multiple experiments more than 7 times.

4.6 Real-time data acquisition

An acquisition method was needed to be followed in order to extract and analyse our data from the 64x64 pixel sensor array accurately and efficiently. The 16 analogue output channels have to be pipelined to a monitoring system, as presented in Fig. 4.4. For that, we used two NI PXIe-6358 measurement cards which were loaded onto a PXIe-1073 5-slot chassis. Pixels were sampled to a maximum data acquisition rate of 40 μs per pixel, corresponding to 10.2 ms for the whole array. Since the acquisition was performed by the 16 output channels simultaneously, the array acquisition rate of the array is 256 times the rate of the single pixel.

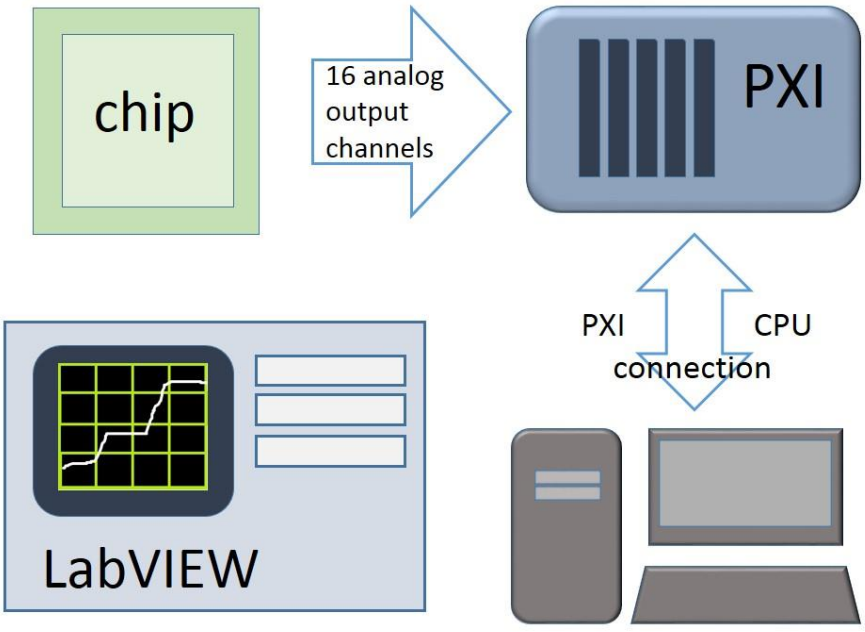

Fig. 4.12: Interconnection of the system for real-time data acquisition.

The whole system is interconnected as shown in Fig. 4.12. Control over the experiments was achieved by the LabVIEW software through three basic programs: one for real-time data acquisition, one for single-pixel data monitoring and one for the whole 64x64 array all developed by chip's originator Balazs Nemeth and further optimised by Boon Chong Cheah, also a member of our team. In Fig. 4.13 the whole experimental setup of the ISFET array is presented. The actual chip with its chip carrier embedded on the PCB, the adaptors for the PXI unit and the Ag/AgCl reference electrode.

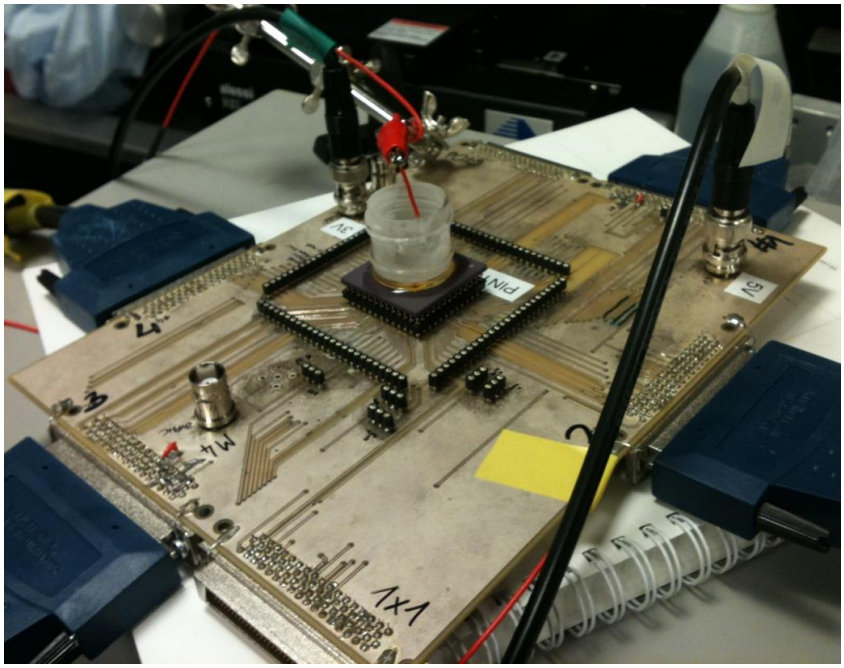

Fig. 4.13: Photography of the whole experimental setup. In the centre we see the chip mounted on the chip carrier and the embedded reaction chamber. Black cables are the power supply and the blue adaptors connect with the PXI unit. We also see the Ag/AgCl electrode mounted on a red wire positioned on top of the chip with a crocodile clip.

4.7 Reference electrodes

As seen before the basic structure of an electrochemical setup consists of a reference electrode, the electrolyte solution and the top insulator layer of the ISFET sensor. We use the reference electrode so a constant bias potential can be maintained across the insulator surface of the chip.

An optimal reference electrode provides our system with robust behaviour, stability in interface potentials and a long life time. Moreover, drying out of the electrode and contaminations from oxidation or other materials can shorten the lifespan of the electrode and eventually can become ineffective. Therefore optimal bias voltages varied in our experiments.

We fabricated custom Ag/AgCl electrodes (Fig.4.14b) that suited our requirements for our measurements.Basic reasons we switched from commercial ones to custom are the following:

- Custom electrodes provided less area than the commercial glass ones for molecules of water or other ions to stick on them and add noise to measurements
- Custom electrodes small size gave us more space on the reaction chamber to monitor what is happening on the surface supplementary with a microscope and more convenience for injections etc.
- The low cost of the custom reference electrodes and the easy way they are fabricated made it easier for us to refresh them more often

BASi RE-6 commercial reference electrodes were also used for some tests, but they were not so applicable due to their size (Fig.4.14a). The BASi RE-6 electrodes are also Ag/AgCl electrodes contained in a glass body 3 cm long a slightly more than 6 mm as seen in the picture. The tip of the electrode is gold-plated .The glass protection of the electrode was thick enough to sometimes block our vision of what was happening on the surface of the chip, which was sometimes necessary. Also the water which was accumulated electrostatically on the surface of the glass caused an increase of even 50% on noise in our measurements.

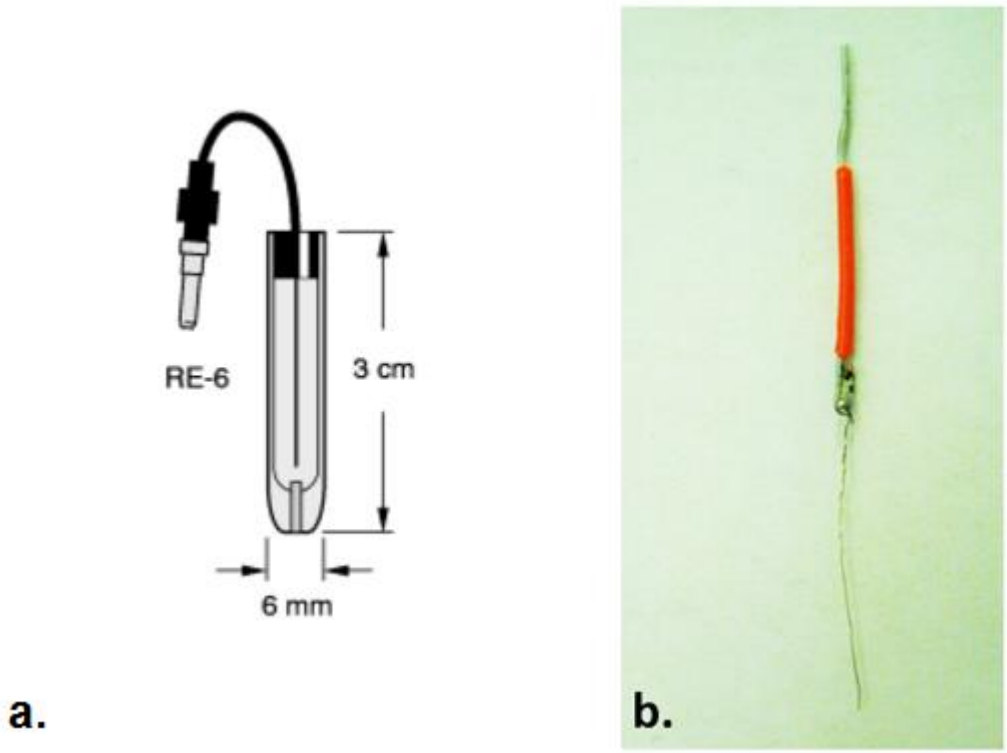

Fig. 4.14: Photographs of reference electrodes: a. the BASi RE-6 commercial reference electrode, b. a custom Ag/AgCl reference electrode fabricated for our experiments

4.7.1 Custom Ag/AgCl reference electrode

The Ag/AgCl reference electrode was fabricated using a wire of silver applying a three electrode cell procedure[47] This process is demonstrated in figure 4.15. The Ag/AgCl reference electrode, a Ag working electrode and a Pt counter electrode were used. The electrolyte used was a solution of 0.1 M KCl and the oxidation took place in a glass baker where the electrodes were placed manually. 1.3 V of voltage was applied to the working and Ag/AgCl electrode resulting to a difference between working and counter electrode which caused an ionic current to flow through the electrolyte. The whole process of oxidation lasted 1 minute. Finally the electrode was rinsed with DI water, left to dry and kept in a box away of light

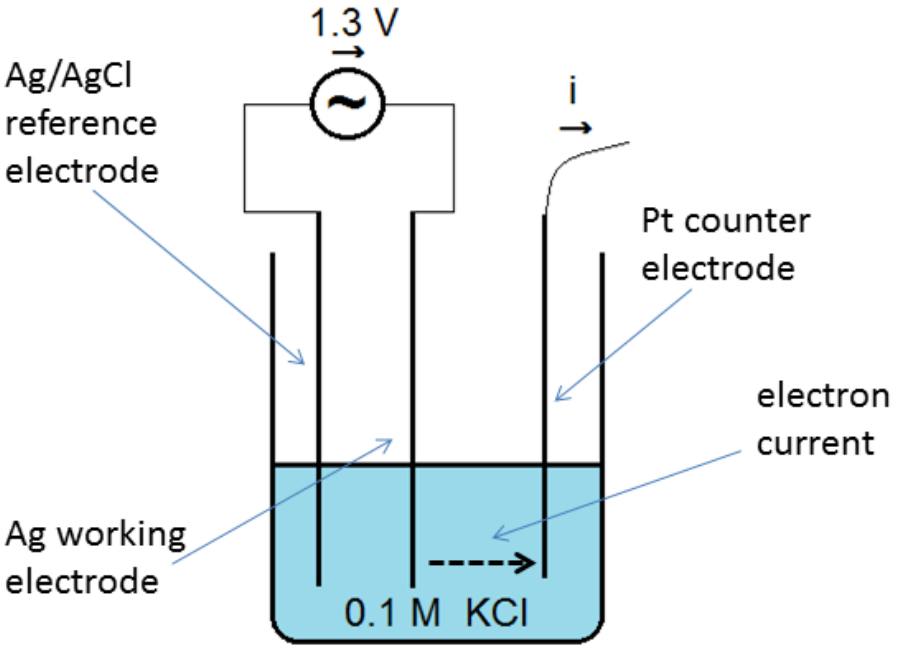

Fig. 4.15: Method of custom Ag/ACl reference electrode fabrication

They provided a robust tool for acquisition without the noise effects associated with electrostatic interactions, however they demonstrated short life, lasting no more that 5-6 measurements due to their sensitivity to light and the easily corroded AgCl from various acids used in the experiments. Fortunately their fabrication procedure was quick and easy, so they were replaced frequently.

4.8 Summary

A 64x64 pixel ISFET sensor array have been previously fabricated with the use of a 0.35 μm four-metal CMOS process by austriamicrosystems AG. Fabrication was carried out in the Fraunhofer foundry. A packaging process was also developed with the use of epoxy and other sealants. The chip was embedded in a digital addressing circuitry and interconnected with a PXI device for data acquisition in real-time measurements. The whole experiment was controlled over with the use of the LabVIEW software. A custom Ag/AgCl reference electrode was used for the experiments instead of the commercial ones to provide flexibility and applicability to our experiments.

4.8 Conclusion

In this chapter we examined the basic and the auxiliary circuitry of the sensor device but also the encapsulation process of the isfet array. We made significant changes on the encapsulation methods increasing the sensitivity and the life-

time of the chip sensor. We used better methods for applying the sealant, room temperature curing time for the epoxy and smaller reaction chambers managing thus space more efficiently. The chips were now able to function for multiple experiments and could be used several times instead of once or twice as previously.

5. Performance with H, Na and K cations

5.1 Introduction-Motivation

In this chapter we perform experiments studying hydrogen, sodium and potassium cations activity in solution. As these measurements were at the beginning of our research, techniques used were optimized through time. Selective layers were introduced to achieve exclusive detection of specific cations.

Motivation for this kind of experiments was that selectivity of ions can lead to the design of a biosensor capable of detecting concentrations of specific cations in blood or other human fluids. It is widely known that sodium and potassium are electrolytes found in the human serum and are linked with blood pressure. Also calcium, althought not examined here, can be an indicator of high concentration of plaque inside arteries linked with heart disease and many other metals that are linked with various health issues.

5.2 Chip functionality – integrity

We use LabView to monitor our ISFET array experiments. During the experiment a real time acquisition program is used not only for acquiring data but also to check if the array and its circuitry is working correctly during the measurement. Short-circuits or any other connectivity errors can be detected in this process. When the experiment is concluded, another program is used for monitoring the chip temporally and spatially. This LabView program provides a single pixel view of the experiment but also a 64x64 monitor of the array at a given time frame. This program can be also useful to monitor any part of the chip which is not working properly or at all. Below there is an example of a chip which is partially working. In picture 5.1a. in the

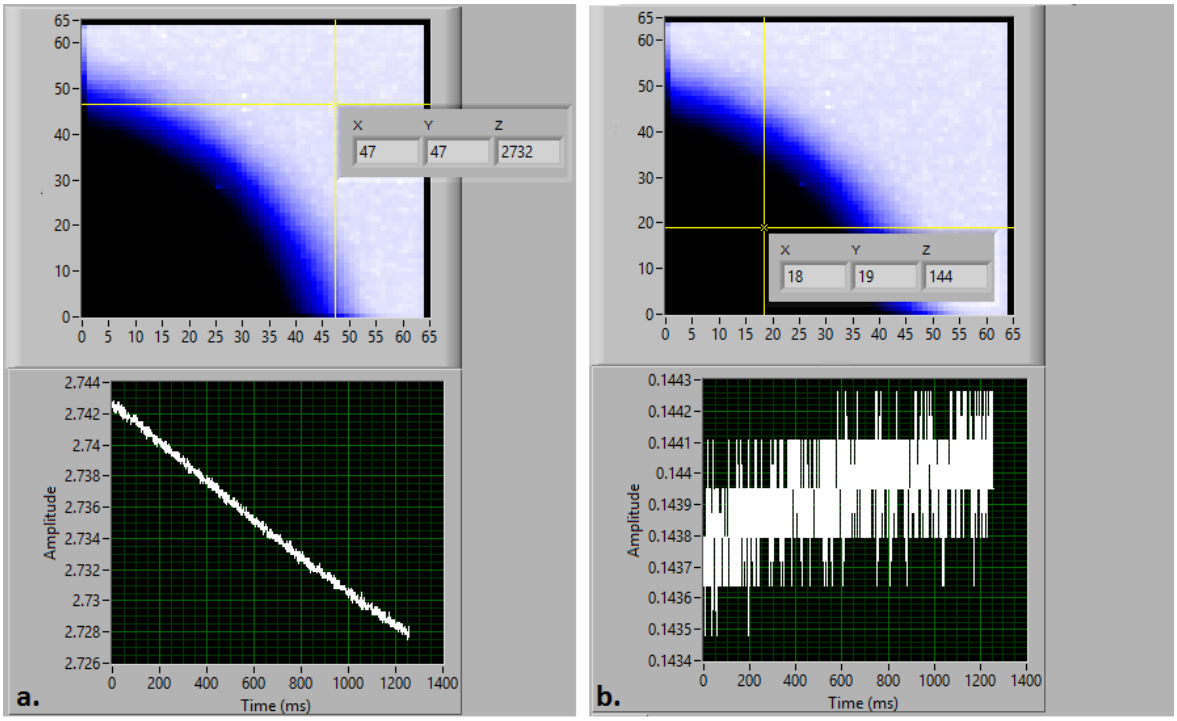

Fig. 5.1: Examining the ISFET array for non-working areas (faulty pixels)

top screen, we can see the cursor being in the bright area, in pixel (47,47). This area indicates the chip's active area, as it can be verified with the graph below which is an expected drift graph of pixel (47,47) through time. The cause of this behaviour, drift, which is profound in most of ISFET devices, is examined at the end of this chapter in 5.8. In picture 5.1b, cursor is placed in pixel (18,19), which is a pixel in the dark area of the chip. As can be verified on the single pixel view below, this is a non-working pixel. Its graph appears as a random signal with an amplitude less than millivolts.

5.3 Tests with acidic and basic solutions

We conducted a simple calibration test each time a new chip was used for the experiments. Some chips turned out to be less sensitive than others, so experiments with them were avoided to achieve uniformity in all our measurements.

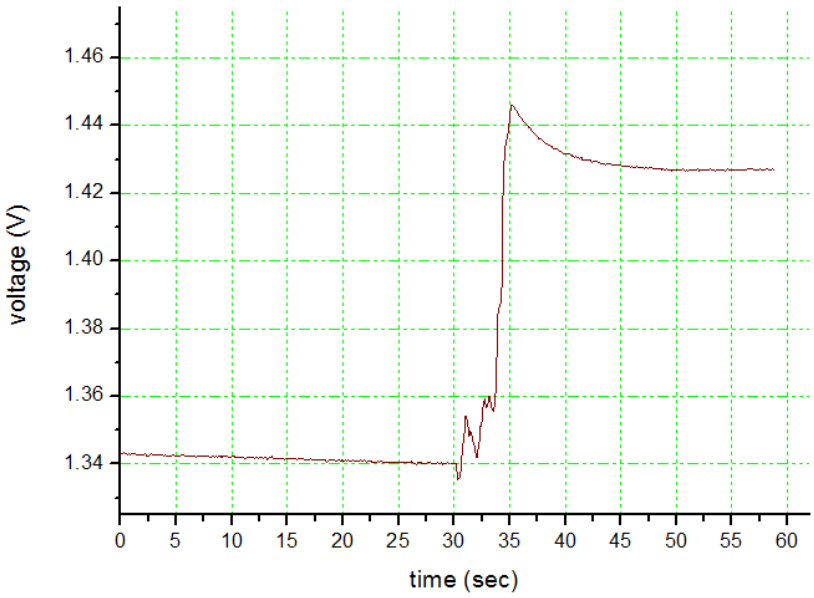

Fig. 5.2 Single pixel sensitivity test. A two-step experiment with solution going from pH=10 to pH=4

The picture 5.2 shows a sensitivity test on a single pixel. We use a pipette to inject 1ml of a commercial buffer solution with pH=10. Then after 30 seconds, the solution is removed and 1ml of buffer solution with pH=4 injected. We can see the step rise of voltage between the two solutions of approximately 100 millivolts. We have a pH difference of 6 units so that means the chip has an average sensitivity of 16.7 mV/pH close to the sensitivity of 20 mV/pH mentioned in reference [1].

Sometimes arrays don't present a uniform pixel sensitivity, but there is a slight differentiation. Therefore, some arrays are only recommended for single pixel measurements, while others, where pixels work uniformly can serve for spatial imaging. The chip of our experiment presented excellent sensitivity but not uniform pixel reference voltage. This is probably caused by cations bound on the chip surface from previous measurements that alter the reference voltage of an individual chip. To demonstrate this behaviour we present the graph below in Fig. 5.3. Sensitivity is identical for all presented pixels, as in the previous graph, but the reference voltage varies.

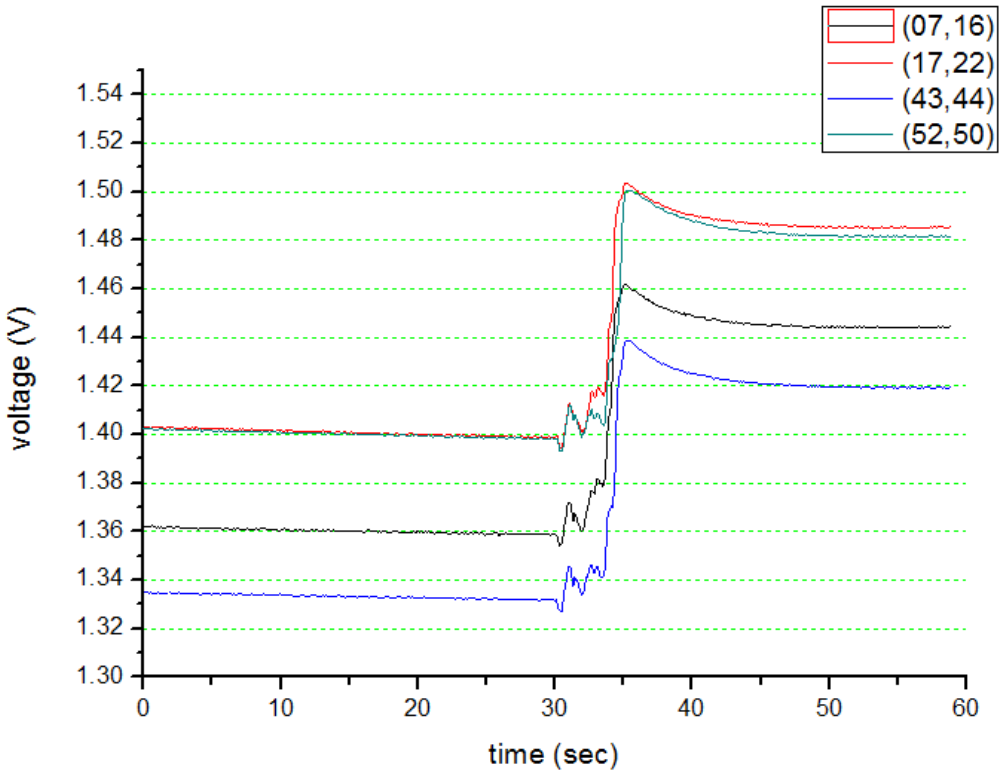

Fig. 5.3: Single pixel view of the sensitivity test for various pixels. We examine four different areas of the array. The reference voltage may vary, but the sensitivity is the same for all four of them (16,7 mV/pH).

5.4 Introductory experiments with ascending concentrations of HCl

Our first attempt to conduct experiments with the ISFET array system was to study and monitor the potentiometric behaviour of the chip with ascending concentrations of HCl. The long-range goal of these experiments is to achieve selectivity of certain cations with the use of specific layers, which we will present in a later paragraph.

We started using HCl solutions with varying concentrations. More specifically, we used solutions of 10^{-4} *M*, 10^{-3} *M*, 10^{-2} *M*, 10^{-1} *M* and *1 M*. We start using the most dilute solution first ending with the most concentrated one. Our aim is precision between concentrations, so removing and adding the solutions was a challenge to be considered. The initial idea was to add each new solution with a precision pipette by injection, leave it for a considerable amount of time, which varied from 30 seconds to 120 seconds most of the time, and then removing it by suction with the pipette, repeating the process for the next solution. In some

initial experiments cleaning with water was applied between solutions but this proved not so crucial later on.

In Fig. 5.4 we use a 120 second time period where each solution stays in the sensor, the suction and cleaning period usually lasts 80 seconds. We start with a 10^{-4} *M* solution till 120 seconds, then 10^{-3} *M* is injected at 200 seconds till 320 seconds and so on, ending with a *1M* solution injected on 800 seconds. The experiment was stopped due to a software's problem before reaching the 120 second period for the last concentration. We can see clear patterns when solution is in the sensor and the expected ascending trend in voltage as solution becomes more concentrated. In Table 5.1 we present the numerical values of this experiment. The error in the values is 500 μV being the smallest voltage change that can be monitored with this sensor [7] which can be amplified due to extra layers deposited, as we will see in 5.5.

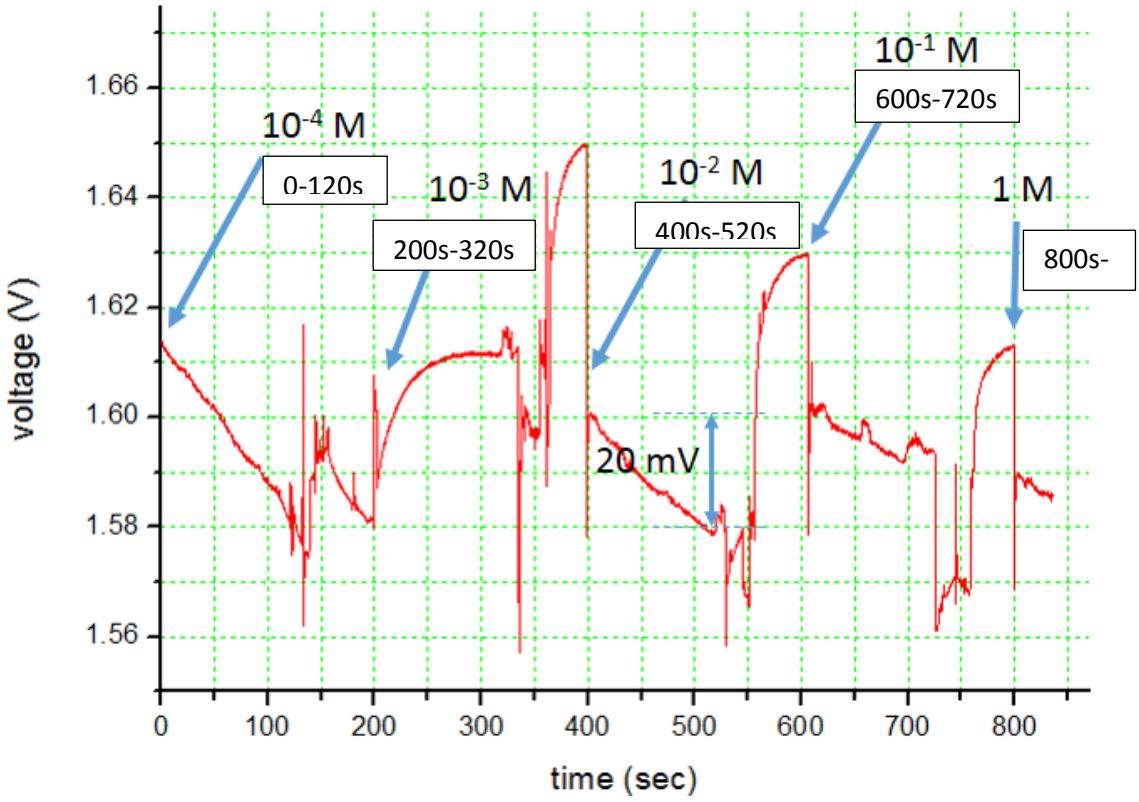

Fig. 5.4: Initial experiment with HCl going from low to high concentration of HCl with a difference in order of magnitude 1 between solutions.

Concentration transition	10^{-4}M →10^{-3}M	10^{-3} M →10^{-2}M	10^{-2}M →10^{-1}M	10^{-1}M →1M
Voltage amplitude	30 mV ±0.5mV	Unclear	20 mV ±0.5mV	≈ 0

Table 5.1: Voltage amplitude of the initial experiment with HCl going from low to high concentration of HCl with a difference in order of magnitude 1 between solutions.

We observe a big drift in voltage. Drift is an intrinsic characteristic of the ISFET [48] examined with more detail at the end of this chapter, but it can be amplified due to bad packaging or because of an electrode that had been used for many experiments. The suction between solutions often produces spikes of voltage or other unexpected behaviour. We measure voltage differences between the initial injection and previous value just before suction. Interesting to see that some steps have the expected voltage difference, as between 10^{-2} M and 10^{-1} M which is 20 mV. Although the drift is very big, in these initial experiments, the signal of the transitions can be distinguished due to the very fast response of the sensor to the change of the concentration. Moreover, the signal would have an even bigger amplitude if we could substract the suction time.

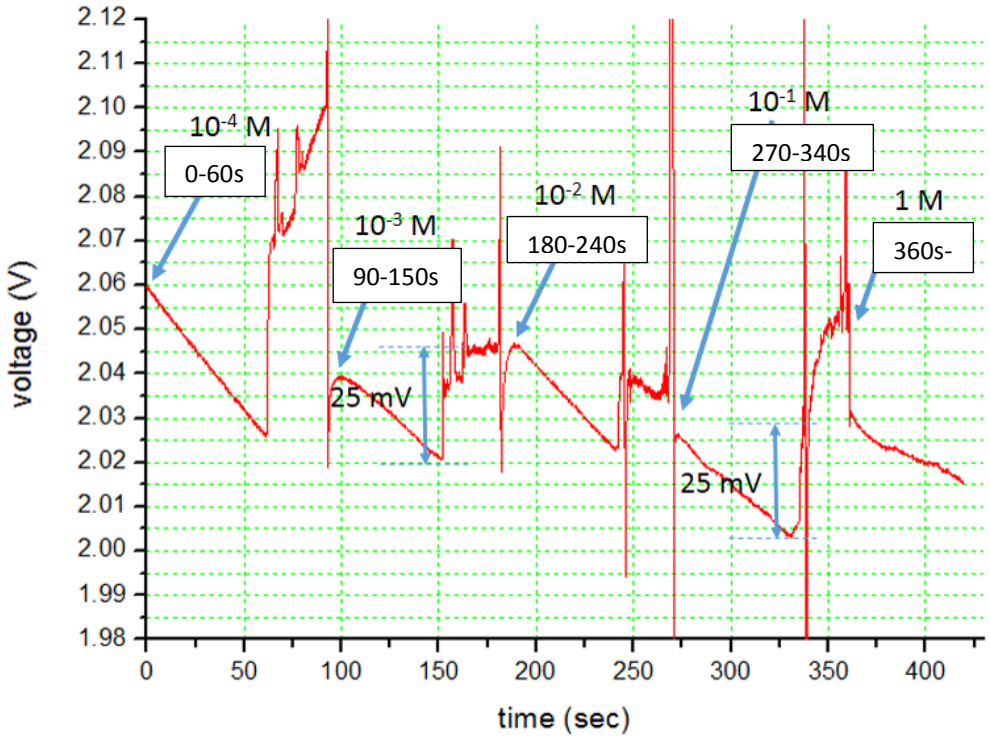

Fig. 5.5: Another experiment with HCl going from low to high concentration with a difference in order of magnitude 1. Although we have still a big drift, we achieved clearer ascending trends between solutions.

In Fig. 5.5 we see another similar experiment. This time we used a 60 second period interval to examine voltage differences and tried to keep the cleaning time between solutions shorter, approx. 30 seconds. This time a better maintained electrode was used and the solution curves are less noisy and more uniform. The voltage difference between the *1 M* and *0.1 M* solutions is *25 mV*. The same voltage difference was observed between 10^{-3} *M* and 10^{-2} *M* solutions. In Table 5.2 the numerical values of the voltage amplitude is presented.

Concentration transition	10^{-4}M $\rightarrow 10^{-3}$M	10^{-3} M $\rightarrow 10^{-2}$M	10^{-2}M $\rightarrow 10^{-1}$M	10^{-1}M $\rightarrow$1M
Voltage amplitude	15 mV ±0.5mV	25 mV ±0.5mV	≈ 0	25 mV ±0.5mV

Table 5.2: Numerical values of amplitude from the experiment shown in Fig. 5.5

5.5 Introductory experiments with ascending concentrations of KCl

Using the same method, we proceeded with KCl measurements following the same steps in adding solutions from 10^{-4} *M* to *1 M* with the same difference in order of magnitude, i.e. 1. KCl seemed harder to monitor with results varying from chip to chip, but a smaller difference in voltage was detected between solutions of different KCl concentrations.

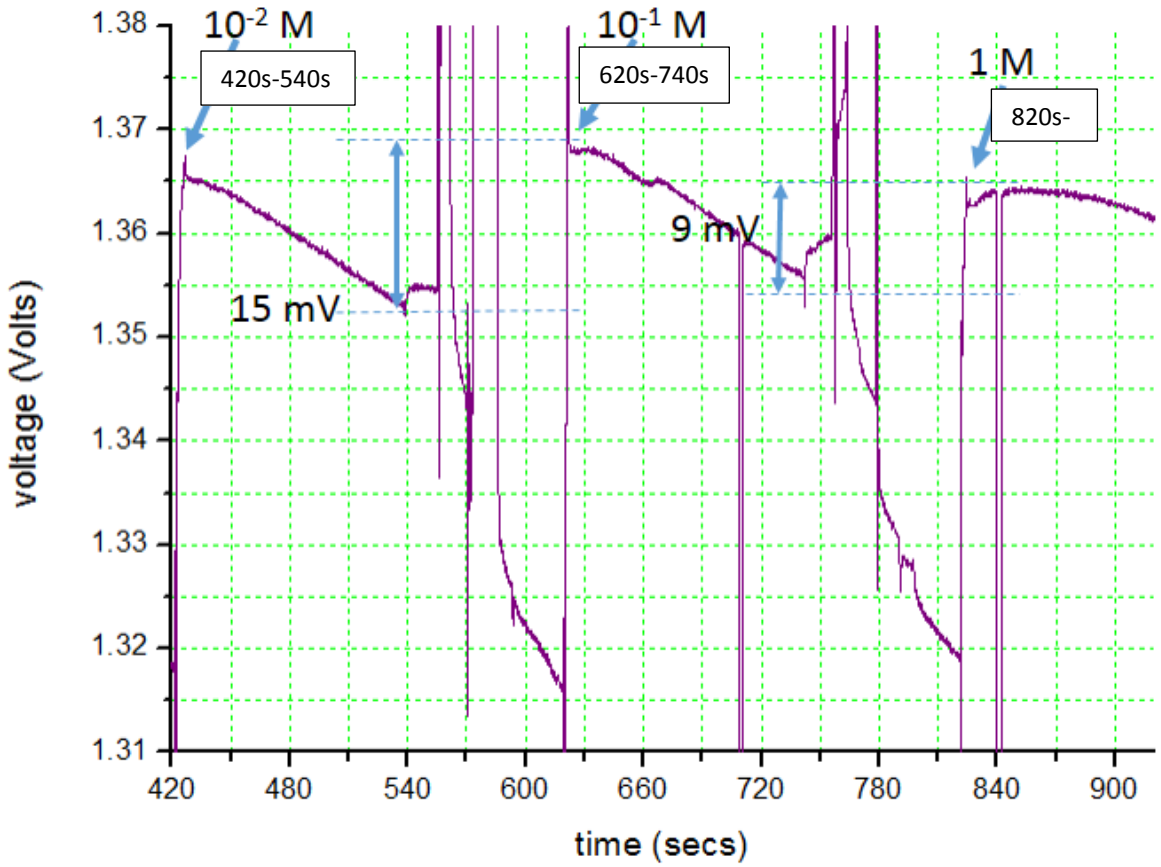

Fig. 5.6: Experiment using ascending concentrations of KCl. The voltage difference between different concentrations is smaller than for HCl.

Fig. 5.6 shows an experiment using ascending concentrations of KCl on the ISFET array. We start with injecting 10^{-2} *M* of KCl and leaving it on the array for 120 sec. On this experiment we employ a longer cleaning process introducing de-ionized water between solutions. We use suction to remove the solution, then we introduce water and wash the array three times, before injecting the new solution. This longer cleaning process results in more spikes seen on the graph. The voltage difference we took amongst these three solutions is *15 mV* and *9 mV* respectively from 10^{-2} *M* to 10^{-1} *M* and from 10^{-1} *M* to *1 M*. In the literature, most values are less than 20 mV/pK [49]. Some are near 8 mV/pK [3], or 7 mV/pK [50] and some even less than 2 mV/ pK [51] depending on different additional sensitive layers applied. For biomedical purposes we are mostly interested in solutions of pK between 1 and 3, these are the values that can be found in human blood serum [49]. Table 5.3 shows the numerical values of voltage amplitude of this experiment.

Concentration transition	$10^{-2}M \rightarrow 10^{-1}M$	$10^{-1} M \rightarrow 1M$
Voltage amplitude	15 mV ±0.5mV	9 mV ±0.5mV

Table 5.3: Numerical values of voltage amplitude for the KCl experiment described in Fig. 5.6.

5.6 Introducing polyoxometalate thin layers

We tried to convert our ISFET sensor array to a selective potentiometric sensor for specific ions. More specifically, we tried to introduce selectivity to potassium cations and to achieve a zero or almost zero response to protons and other cations, such as sodium ions.

Polyoxometalate (POM) crystals were used in order to construct POM salts to use as layers on the top of the chip. We used a specific structure of POMs called crown heteropolyanions which are more or less large molecular anionic structures with specific ion binding properties. The heteropolyanion used is $[P_8W_{48}O_{184}]^{40-}$ (Fig.5.7) which is derived from a mixed potassium/lithium salt $K_{28}Li_5H_7[P_8W_{48}O_{184}]\cdot 92H_2O$, the procedure of its synthesis can be seen here [52]. This heteropolyanion has the ability to bind with potassium cations (K^+) at pH >4 [53].

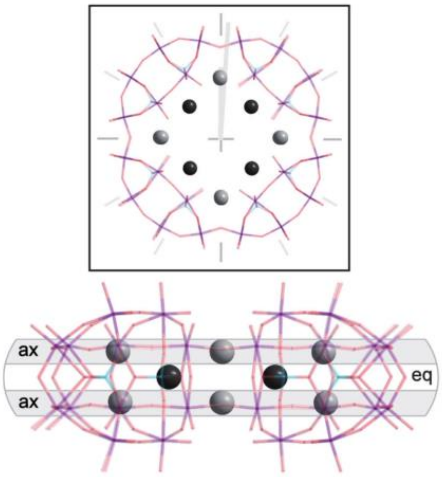

Fig. 5.7: The structure of the $K_{28}Li_5H_7[P_8W_{48}O_{184}]\cdot 92H_2O$ POM salt used to construct a potassium selective layer on the ISFET array. Black and grey spheres indicate the binding sites for potassium ions within the POM cavity [53]

This experiment was conducted with the collaboration of people from The Cronin Group from the Department of Chemistry, University of Glasgow. With their help, we formed an 8-layer substrate of the salt's anion onto the chip surface. The number of layers results from a compromise between having enough layers to detect ion acivity but not too many to add excess noise to our measurements. Then the substrate was dried and the chip was ready for experiments.

We used the same sequence of solutions as in the previous initial experiments. After some test measurements we concluded to conduct a single run of measurements of HCl, NaCl and KCl solutions one after the other in this order going like before from 10^{-4} *M* to *1 M* in the following steps: 10^{-4} *M*, 10^{-3} *M*, 10^{-2} *M*, 10^{-1} *M* and *1 M*. Each solution remained on the chip surface for 120 seconds. Between same substance solutions we washed the array with water. Each washing lasted approximately 80 seconds. Between substances, that is between HCl, NaCl and KCl respectively we conducted multiple flushes with water to make sure that that the array is not contaminated with the previous substance. These two flushing steps were at 300 and 500 seconds respectively shown in Fig.5.8.

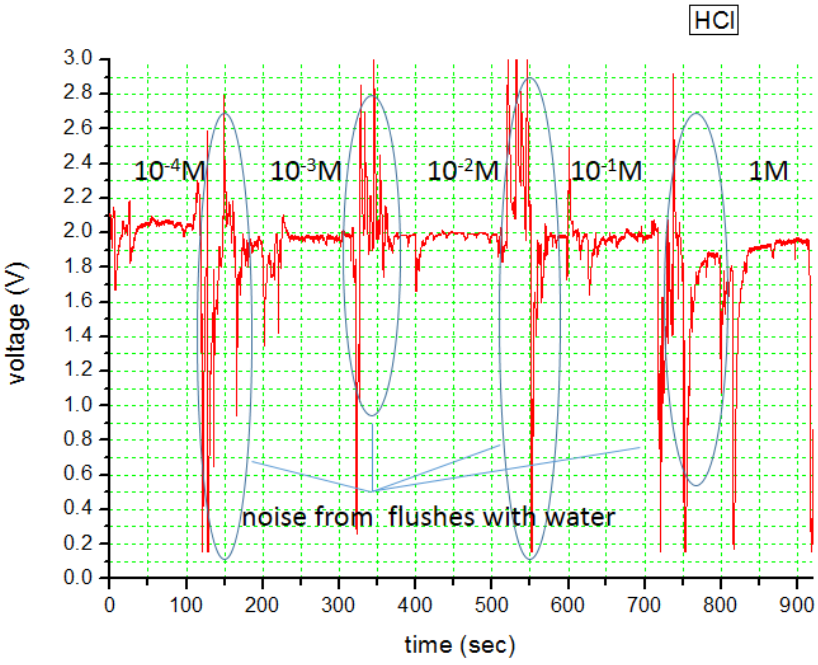

Fig. 5.8: Layer experiment with HCl going from small to big concentration with a difference in order of magnitude 1. The additional substrate used is an 8-layer of crystallised $[P_8W_{48}O_{184}]^{40-}$.

Concentration transition	10^{-4}M $\rightarrow 10^{-3}$M	10^{-3} M $\rightarrow 10^{-2}$M	10^{-2}M $\rightarrow 10^{-1}$M	10^{-1}M $\rightarrow$1M
Voltage amplitude	Not clear	0 mV ±10mV	0 mV ±10mV	-30 mV ±10mV

Table 5.4: Voltage amplitude of experiment with HCl going from low to high concentration of HCl with a difference in order of magnitude 1 between solutions.

In Fig.5.8, in comparison with the previous HCl experiment, the layer experiment seems to be insensitive to protons. The response is noisier as can be seen clearly in Fig 5.9 due to the salt formation on the surface of the chip from the POM extra layers reaching an error of as big as ±10mV, but this noise maintains a stable pattern around the mean value in each concentration.

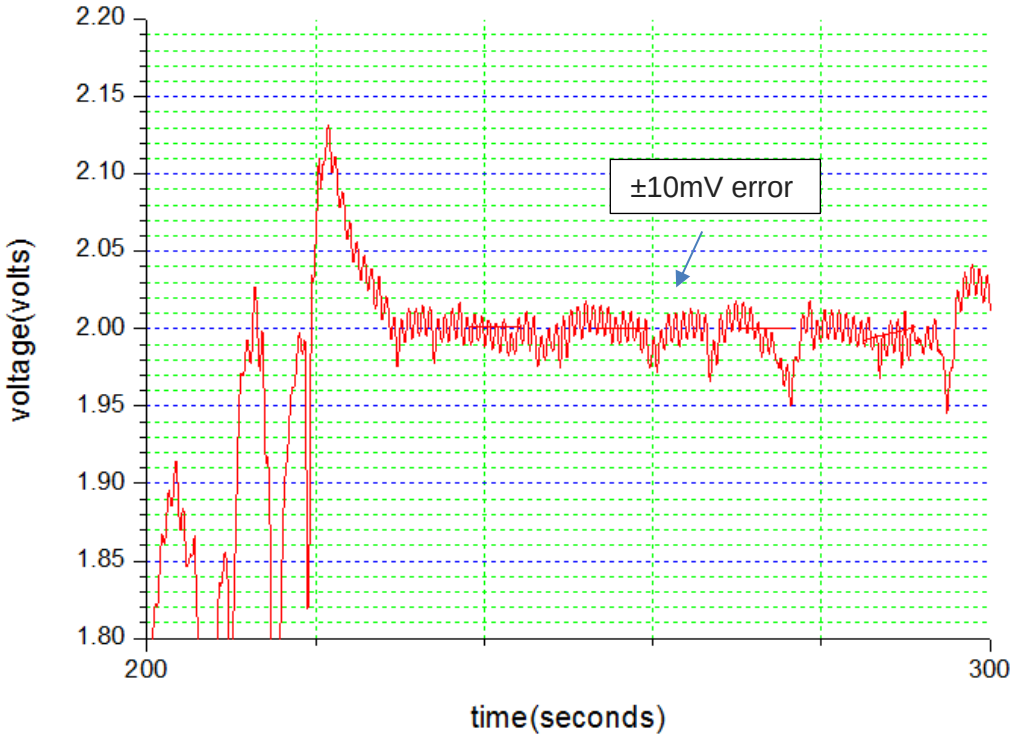

Figure 5.9 Detail of the noisier signal of figure 5.8 between 200 and 300 seconds

As concentrations are growing, the response stays stable to a certain threshold. The big spikes are noise during the 'suction-injection' cleaning process that

doesn't seem affect the response of the sensor when it contains measurable solution.

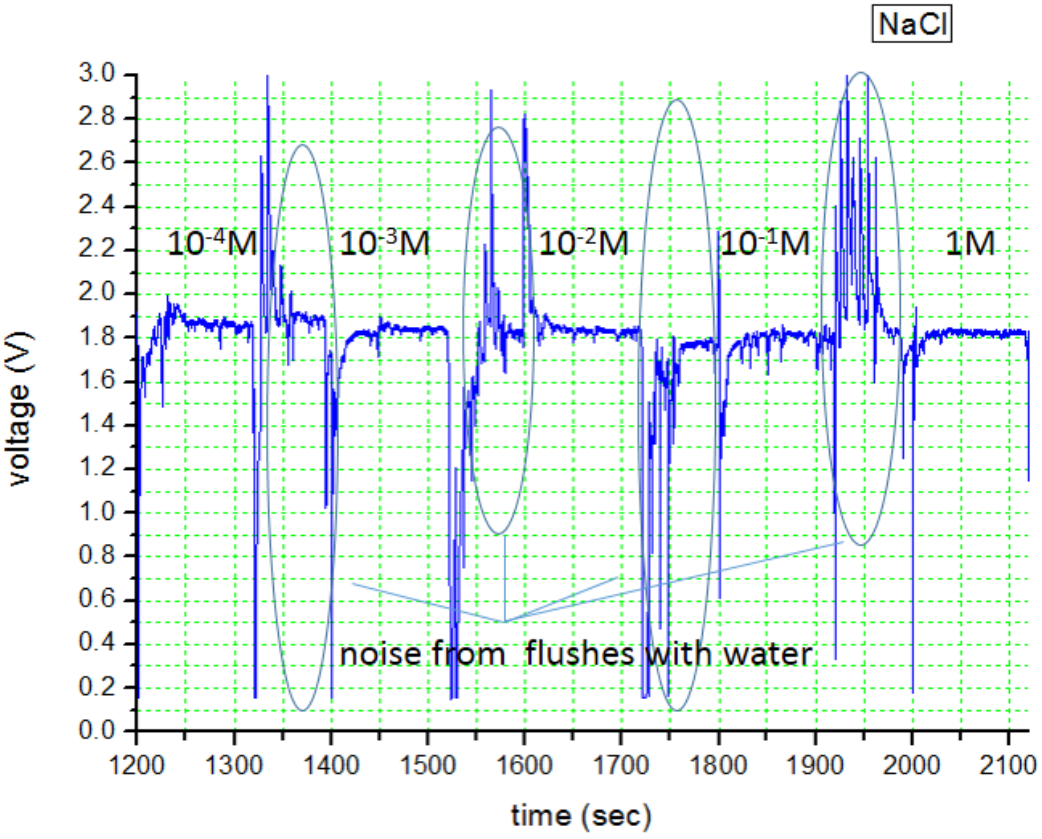

Fig. 5.10: Layer experiment with NaCl going from a small to large concentration with a difference in order of magnitude 1. The additional substrate used is an 8-layer of crystallised $[P_8W_{48}O_{184}]^{40-}$.

Concentration transition	$10^{-4}M \rightarrow 10^{-3}M$	$10^{-3}M \rightarrow 10^{-2}M$	$10^{-2}M \rightarrow 10^{-1}M$	$10^{-1}M \rightarrow 1M$
Voltage amplitude	-30mV±10mV	0 mV ±10mV	0 mV ±10mV	-30 mV ±10mV

Table 5.5: Voltage amplitude of experiment with NaCl going from low to high concentration of HCl with a difference in order of magnitude 1 between solutions.

In Fig. 5.10 we used NaCl going through the same process with ascending concentrations. We notice the same thing as with HCl. The response remains stable also with the Na cations. However, a small drift can be noticed through time, as also observed with HCl.

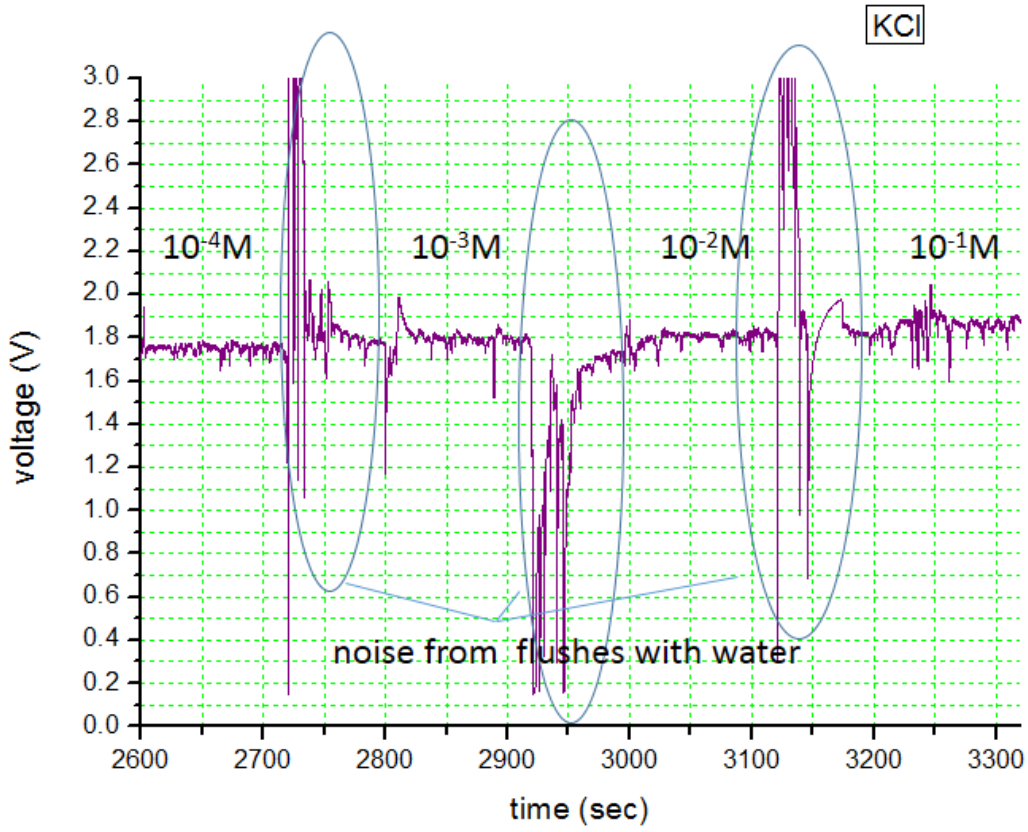

Fig. 5.11: Layer experiment with KCl going from small to big concentration with a difference in order of magnitude 1. The additional substrate used is an 8-layer of crystallised $[P_8W_{48}O_{184}]^{40-}$.

Fig. 5.11 shows the response of the layered array with the addition of ascending concentrations of KCl. The difference of the previous graphs is that there is an ascending trend noticed with the potassium cations. Fig. 5.12 gives a closer look to the graph. The noise pattern is the same with all solutions, only magnified. Here it is more evident that there is a strong ascending trend similar to the previous experiments without the POMs layer. More specifically 10^{-4} *M* of KCl gives a value of 1.755V and 10^{-3} *M* of 1.795V, that is a 40 mV difference. 10^{-2} *M* to 10^{-3} *M* gives a 25 mV difference and 10^{-1} *M* to 10^{-2} *M* gives a 40 mV difference. Table 5.6 provides us a numerical representation of the amplitude of voltage for this experiment

Concentration transition	10^{-4}M →10^{-3}M	10^{-3} M →10^{-2}M	10^{-2}M →10^{-1}M
Voltage amplitude	40 mV ±10mV	25 mV ±10mV	40 mV ±10mV

Table 5.6: Values of amplitude of voltage for the POM layer KCl experiment described in Fig.5.11.

Observing the whole experiment we can conclude that the ISFET sensor with the additional 8-layer of $[P_8W_{48}O_{184}]^{40-}$ remained insensitive to protons and sodium cations but a response was noticed when potassium cations added. Although there was a noticeable amount of noise, the ISFET sensor managed to act as an exclusive potassium ion sensor for concentrations from 10^{-4} *M* to 10^{-1} *M*, concentrations we encounter when we study human blood serum.

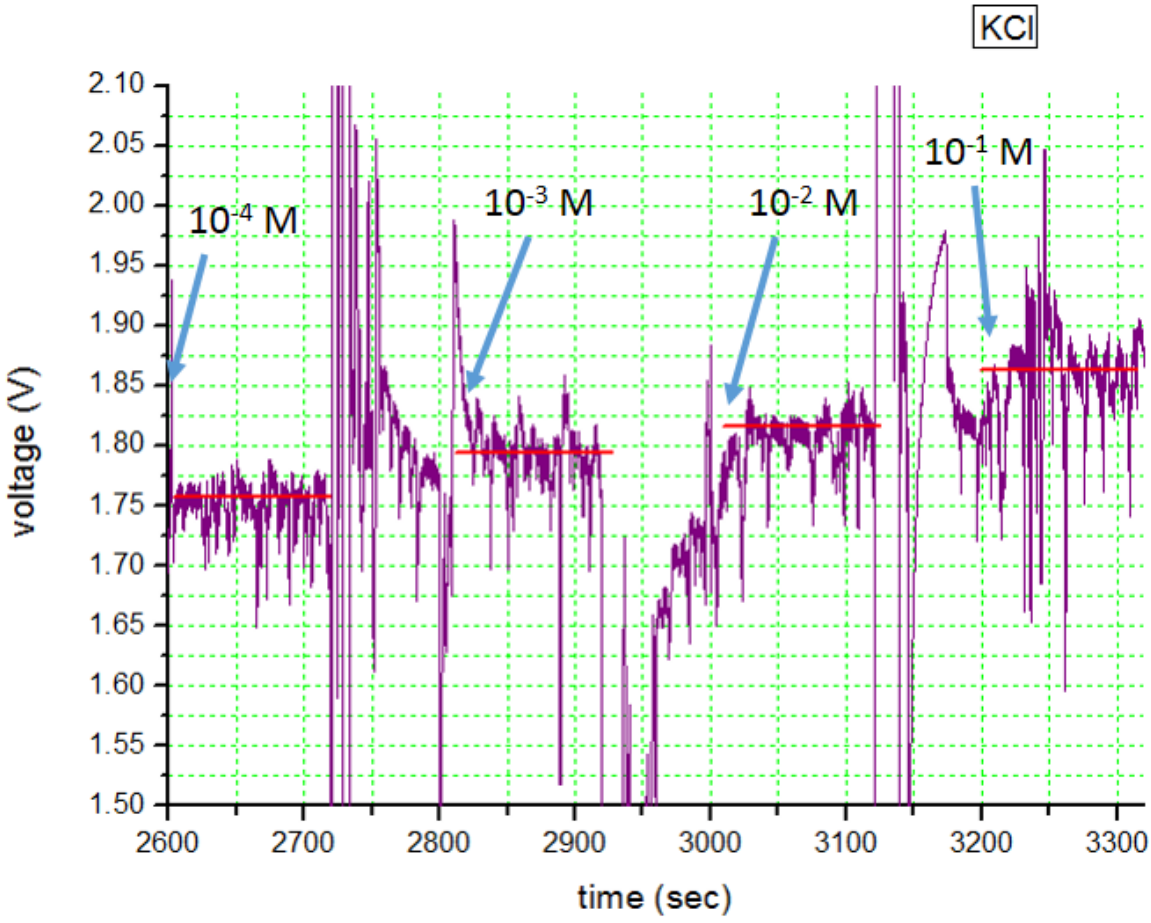

Fig. 5.12: Zoomed view of the graph of the 8-layer crystallised $[P_8W_{48}O_{184}]^{40-}$ substrate experiment with KCl

Undoubtedly the noise introduces a big measuring error to our measurements reaching 12.5 mV. The validity of our measurements can be further strengthened by comparison of all three runs of the ions where differences are more profound. For this, a graph is presented below in Fig. 5.13 to show the whole measurement process. Scale is not optimal for each substance separately, but provides a good overview for comparison between all substances showing drifting behaviour for HCl and NaCl and ascending behaviour for KCl thus implying the layer's selectivity to potassium. The experiment is also described in Table 5.7 in terms of the graph trend and sensitivity. Further experiments need to be conducted to secure these promising results.

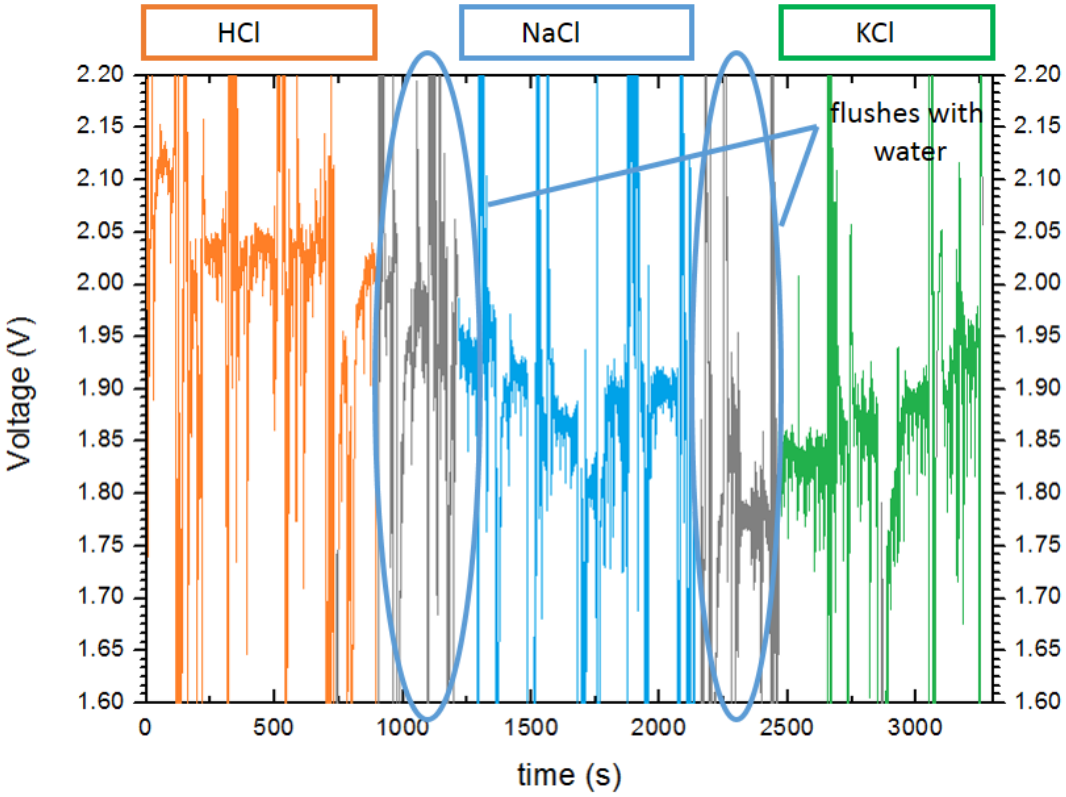

Fig. 5.13. Graph presenting all cations used in the experiment

	trend	sensitivity
HCl	stable/decreasing due to drift	no H+ sensitivity
NaCl	stable/decreasing due to drift	no Na+ sensitivity
KCl	ascending	K+ sensitivity

Table 5.7: Presentation of the whole experiment for ascenting concentrations of HCl, NaCl and KCl in sequence, in terms of the graph trend and the corresponding ion sensitivity.

5.7 Advanced experiments with ascending concentrations of HCl (no additional layer)

We kept repeating the descending concentrations experiments throughout our research, optimizing packaging, reference electrode functionality.

More specifically we:

- Kept the Ag/AgCl reference electrode for a maximum of 3-4 measurements and always away from light.
- Used DI water to clean all surfaces of chip and reference electrode
- Used N_2 gun to dry reference electrode and chip surface before measurement
- Kept reference electrode and chip insulated in a plastic box

In some runs we achieved minimum noise and drift. In the latest runs we changed the method of going through different concentrations. We kept the same mode of descending in an order of magnitude 1, but the actual solution addition was changed. It was considered that suction and injection throughout the different concentrations might affect some of the initial properties of the sensitive membrane for every new concentration. A new method was introduced where only injection was applied but with the appropriate manner so the concentrations changed in the same way as before. Therefore, the measurement goes 10^{-4} *M*, 10^{-3} *M*, 10^{-2} *M*, 10^{-1} *M* and concludes at *1 M* of solutions only through injecting. This is considered to result in a more robust transition between concentrations.

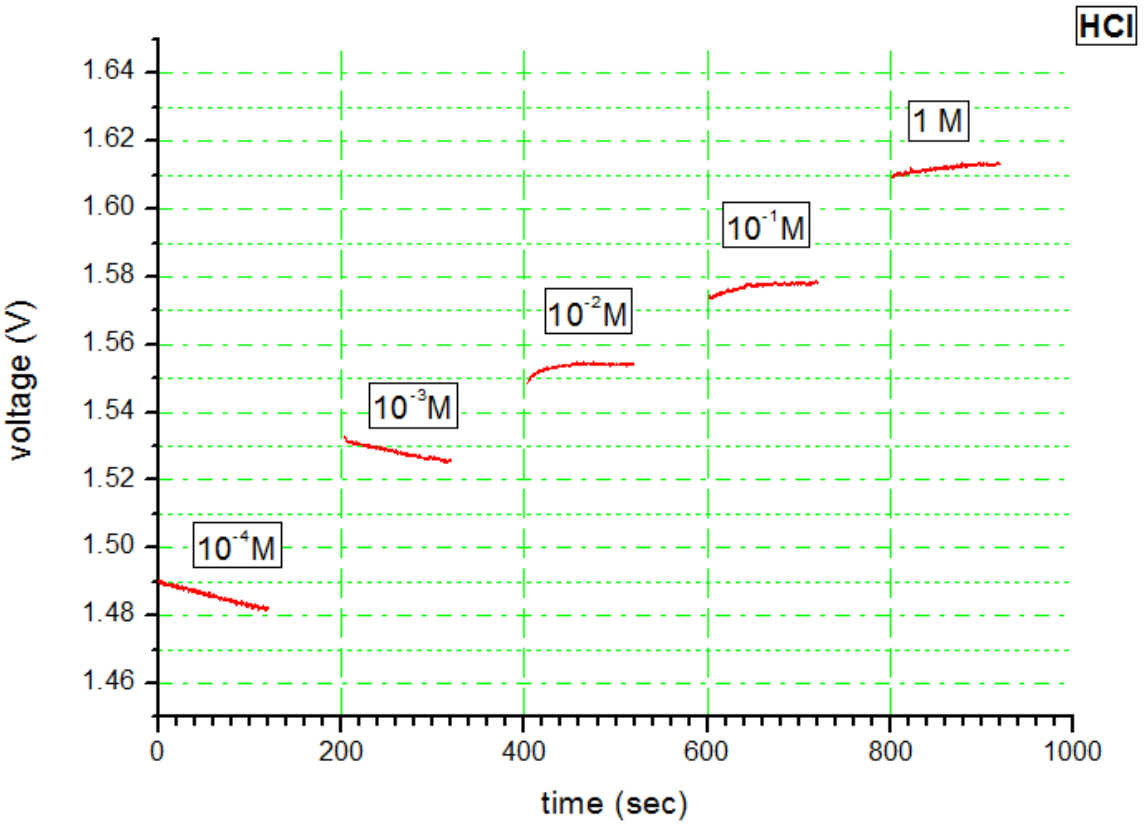

Fig. 5.14: Advanced experiment with HCl going from small to big concentration with a difference in order of magnitude 1. No suction was introduced this time, a different method was used implementing only injection of liquids. Time intervals of the injection were removed in this graph, for a better understanding of the transition.

Fig. 5.14 shows an HCl experiment with the use of the new injection-only method. Time intervals of the injections between concentrations were removed to emphasize voltage transitions. The drift and noise noticed is minimal. The transition voltages reached a maximum sensitivity recorded for the first time with the ISFET sensor array. More specifically, transition from 10^{-4} *M* to 10^{-3} *M* reached *50 mV*. We also had *30 mV* transitions for 10^{-3} *M* to 10^{-2} *M* and for 10^{-1} *M* to *1 M*. Transition from 10^{-2} *M* to 10^{-1} *M* was measured to be *25 mV*. Table 5.8 also presents the numerical values of the the voltage amplitudes in a tabulated form.

Concentration transition	10^{-4}M →10^{-3}M	10^{-3} M →10^{-2}M	10^{-2}M →10^{-1}M	10^{-1}M →1M
Voltage amplitude	50 mV ±0.5mV	30 mV ±0.5mV	25 mV±0.5mV	30 mV±0.5mV

Table 5.8: HCl experiment with the optimized 'injection-only' method corresponding to Fig. 5.14.

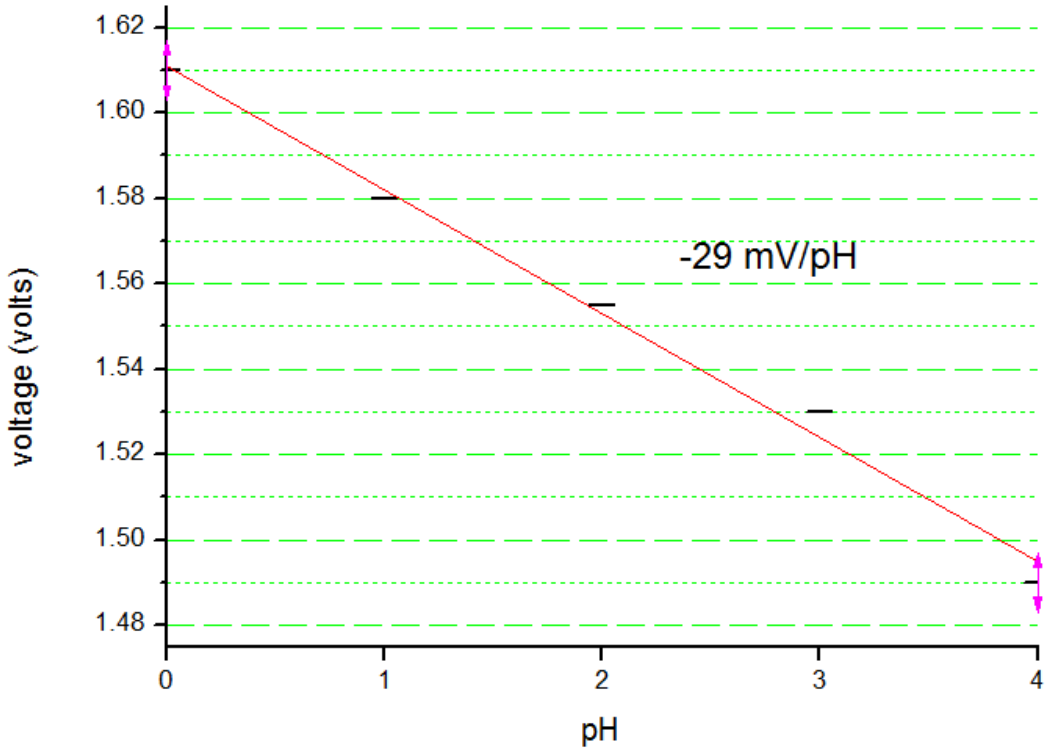

Figure 5.15: Voltage versus pH to present the optimal chip's sensitivity.

Finally, Fig. 5.15 presents the slope of the voltage versus pH to acquire a clearer image of chip's sensitivity and compare it with the graph seen in theory in paragraph 2.4.2. Indeed our silicon nitride surface presents a linear response to ascending concentrations of protons, i.e. to descending pH, with 10^{-4} M of HCl corresponding to pH=4, 10^{-3} M of HCl to pH=3 etc.

The sensitivity here is -29 mV/pH with a maximum of -50 mV/pH for the transition from pH=4 to pH=3, quite close to the theoretical nerstian value of -56.7 mV/pH and better than the -20 mV/pH sensitivity previously measured with the same chip.

In conclusion, it can be said that, optimizing packaging techniques, maintaining reference electrodes and engaging new more robust methods of transition

between liquids we managed to acquire more precise experiments by reducing drift and noise and increasing the sensitivity towards the Nerstian limit.

5.8 Drift

During experiments with ISFETs, a slow temporal change is often noticed taking place regarding the amplitude of the voltage on a measured solution. This phenomenon is widely known in literature as ‘drift’ What really happens is that there is a slow chemical alteration of the insulator as it is exposed to the electrolyte solution .

This modification of the chemical composition of the insulating surface of the ISFET causes a decrease to the insulator capacitance as time evolves and this consequently causes also a change to the threshold voltage of the ISFET [54].

This was monitored in our chips as a monotonic temporal decrease at the amplitude voltage. Through most of the experiments drift is varying between 0.05mV/sec - 0.1mV/sec, quite big for long duration measurements, but not significally affecting ours as we studied fast reactions happening in few seconds.

More specifically, in Figure 5.16, we see the temporal decrease of the amplitude voltage from experiment described in 5.7 when adding 10^{-4} M of HCl. The voltage drops from 1.490 V to 1.482 during a period of 120 seconds indicating a drift of 0.06 mV/sec. Figure 5.17 presents also drift behaviour of our glucose/hexokinase experiment presented in chapter 6 with a drift of 0.1 mV/sec.

Other writers claim that drift can be also caused by reactions happening the the bulk of the transistor [55]. Nevertheless, drift is still an ISFET behaviour which still needs to be investigated further.

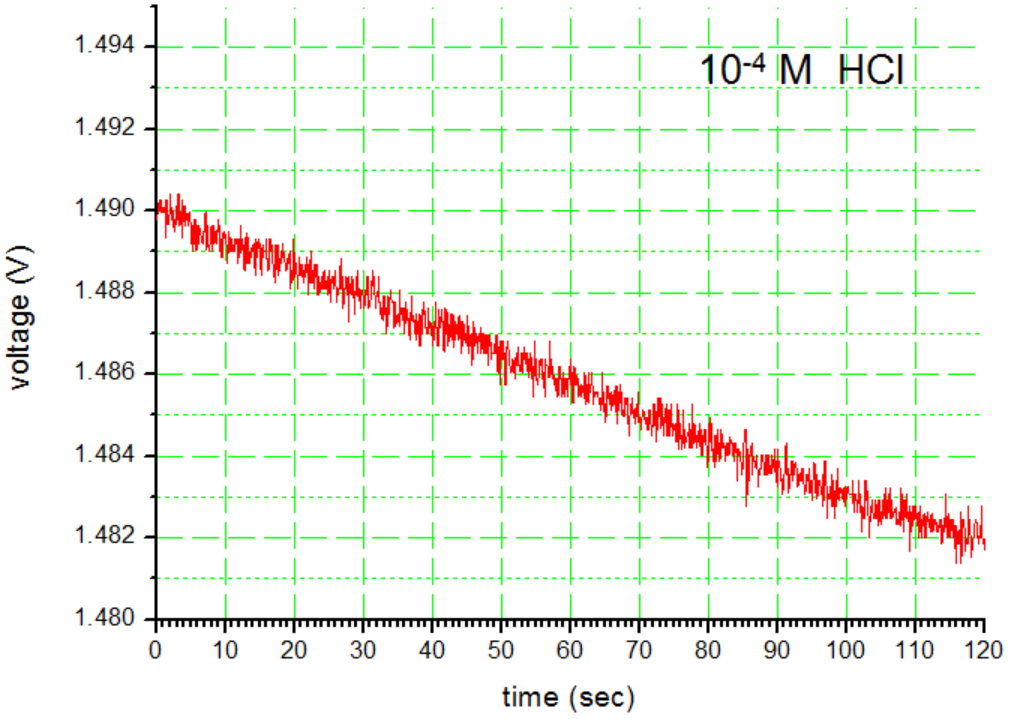

Fig. 5.16: First 120 seconds after addition of 10^{-4} M of HCl of experiment showed in 5.6. The drift follows a steady rate of 0.06 mV/sec.

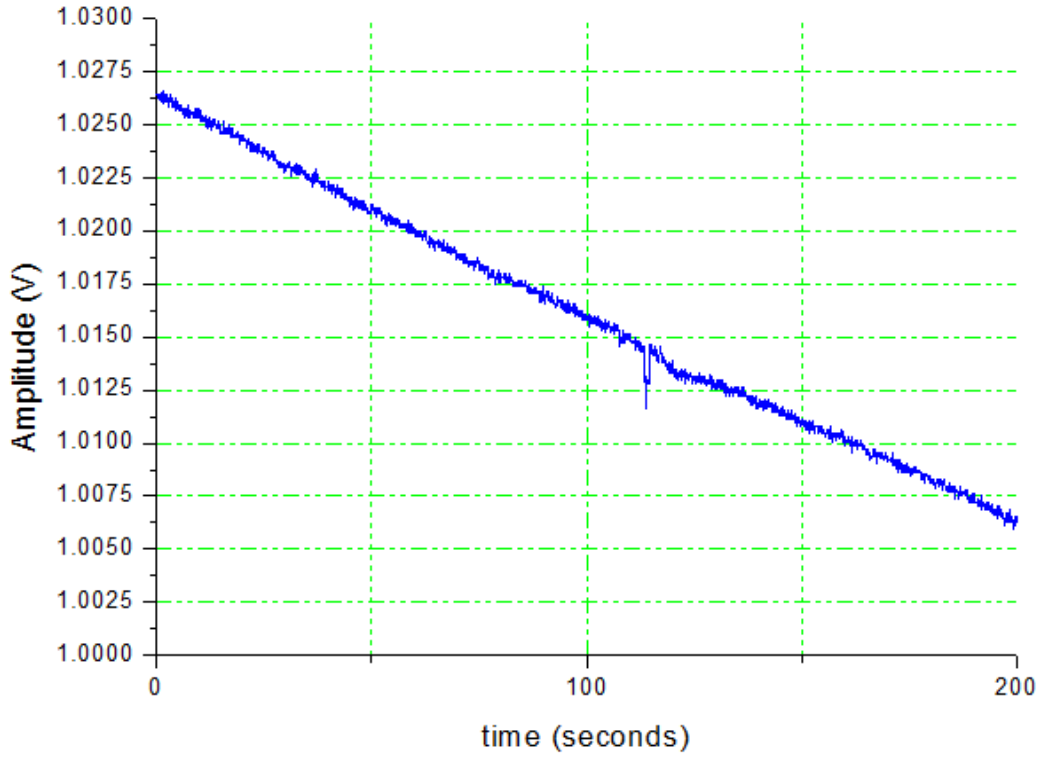

Fig. 5.17: First 200 seconds of a control glucose/hexokinase experiment of chapter 6. The drift follows a steady rate of 0.1 mV/sec.

5.9 Error in measurements

In this chapter, where first experiments with the ISFET sensor were conducted, apart from the actual measurements, we followed a process where methods needed to be optimised for clearer and more accurate results. When no added layer was involved, the error of our measurements was 0.5 mV, as presented before in literature [7] with the exception of flushing in and out solutions of different concentrations, considered as transition states and not taken into account.

When the additional POM layer was added, an ±10mV error in measurement was observed, sometimes even higher as seen in Fig. 5.9. The non-uniform surface of the POM layer definitely added a considerable amount of noise in our measurements but still the differences between the different cation solutions could be examined as in Fig. 5.13

5.10 Summary

We designed an experiment to examine POM's selective sensitivity to potassium cations. Initially we tried the sensor with no additional layer with protons sodium and potassium cations. We verified the expected response as seen previously: ascending amplitude for ascending concentration for protons, but also potassium cations. The average amplitude difference for every order of magnitude concentration was approximately around 25 mV but also significant drift was detected. Then, when the selective POM layer was introduced, the sensor presented selective sensitivity to potassium ions reaching 40 mV for every order of magnitude in concentration. At a later stage, when packaging was optimized significantly and a new technique 'only injection' was introduced, we achieved clearer transitions of amplitude using the same concentrations, less drift and a value of sensitivity of 50 mV/pH that was the closest recorded with this sensors to the Nerstian limit(59 mV/pH)

5.11 Conclusion

We initiate every new chip packaged with test experiments to check its functionality and sensitivity. We perform these test in single-pixel mode to check the voltage amplitude and also on an array mode to check if complete array is working properly. We performed experiments with ascending concentrations of HCl, NaCl and KCl to examine if other cations can be monitored besides protons in solution. We performed two separate experiments, one with no additional layer on the surface of the ISFET array and one with an additional K cation-selective POM layer. We achieved selectivity for K cations with the additional layer at the expense of extra noise. Finally, a more advanced experiment was conducted for a non-additional layer chip only for HCl. This experiment took the chip's sensitivity to the widely accepted uppermost limit for a silicon nitride sensing layer.

6. Experiments with enzymes

6.1 Introduction-Motivation

Enzymes are one of the most important macromolecules involved with energy production in living organisms. Their catalytic behaviour is involved in almost every chemical reaction, procedure and metabolic cycle that has to do with life. Most of them are proteinic structures consisting of organic and also inorganic parts. As catalysts, their main function is to lower the activation energy of a reaction and enable a reaction to reach equilibrium more rapidly. Enzyme activity can be affected by many factors such as temperature and pH.

Chemical reactions where enzymes are involved are of high interest regarding biomedical applications and sensor technology. Many biological catalysts are used already as indicators for a number of health issues such as stroke, heart attack, prostate cancer. Therefore fabricating enzyme ISFET sensors is regarded crucial and many authors presented in literature followed the path of the enzyme sensor fabrication.

Glucose detection in blood for monitoring diabetes is an experiment we found interesting to examine through the first step of glucolysis, a chemical reaction with ionic behaviour which is facilitated by the use of the enzyme hexokinase. We introduced there for a layer with immobilized hexokinase molecules consisting of beads made from sepharose with their size varying from 40 to 165 nm in diameter.

6.2 Preliminary enzyme experiments with papain

We first carried out some preliminary enzymatic test experiments using papain. Papain is a protein enzyme found in nature involved mainly in breaking peptide

bonds[56]. When papain incubates, which takes approximately 5 minutes, the addition of Ti(BALDH) (Titanium(IV) bis (ammonium lactato) dihydroxide) leads to the formation of a precipitate [57]. We attempted to grow minerals on ISFETs and measure the rate of enzyme-catalysed mineral formation.

We used a solution of 5 μM of papain (papaya proteinase) and left it on the surface of the array for 5 minutes. Then we rinsed the chip and the remaining papain was expected to lead to the precipitation of the upcoming titanium salt Ti(BALDH).

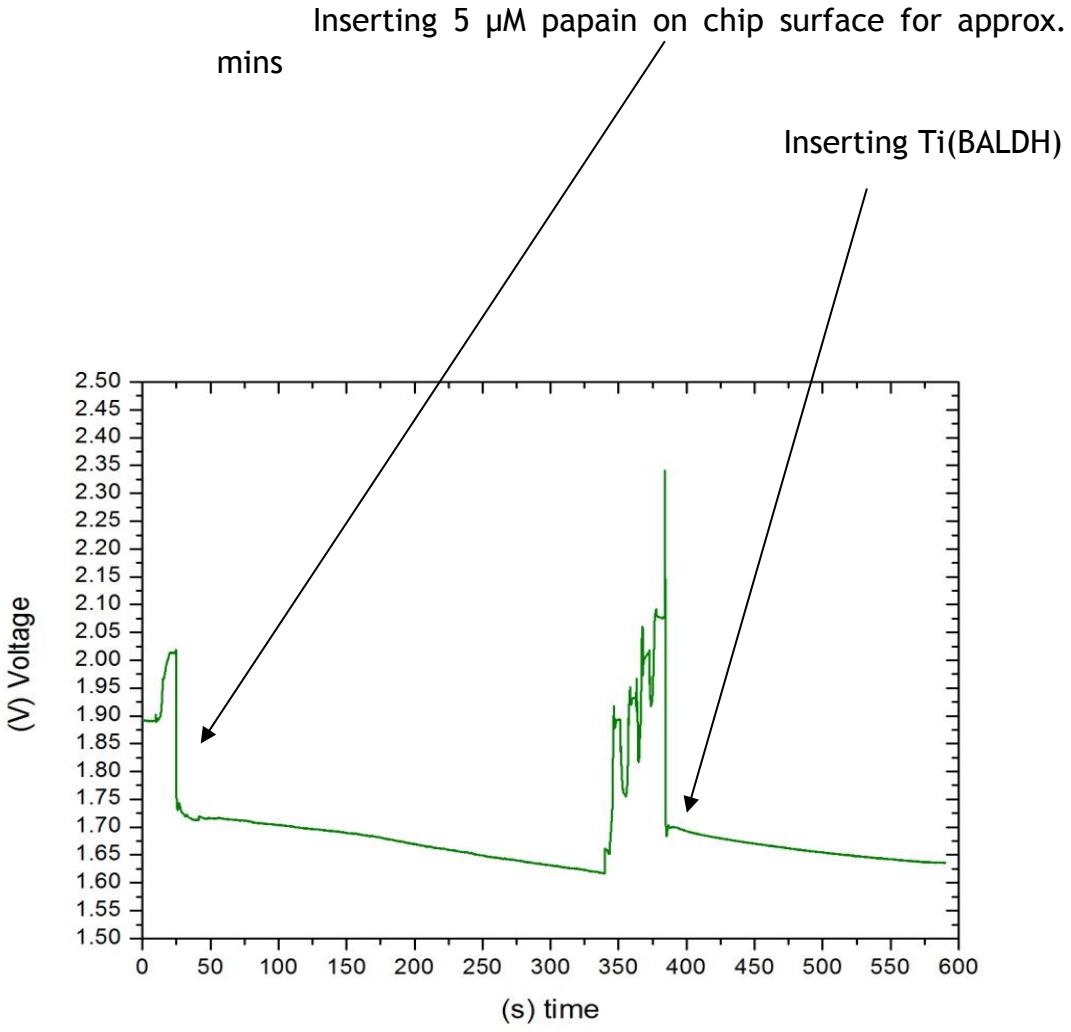

Fig. 6.1: Single pixel papain –Ti(BALDH) experiment

The single pixel image in Fig. 6.1 shows a differentiation on output voltage which indicates ionic activity. We also observe a voltage drift taking place in time which is a standard background on our measurements that has been discussed extensively in most of the paragraphs of Chapter 5. Furthermore, an image of the whole sensor array is needed to decide if any precipitation is formed in a specific area of the chip. We also have to clarify that the noisy signal between 340 and 390 seconds happens during the cleaning process of the chip's surface. The cleaning process was the same as in previous chapter. Suction and injection with cleaning liquids that introduced the formations of spikes on the graph but without affecting the outcome significantly.

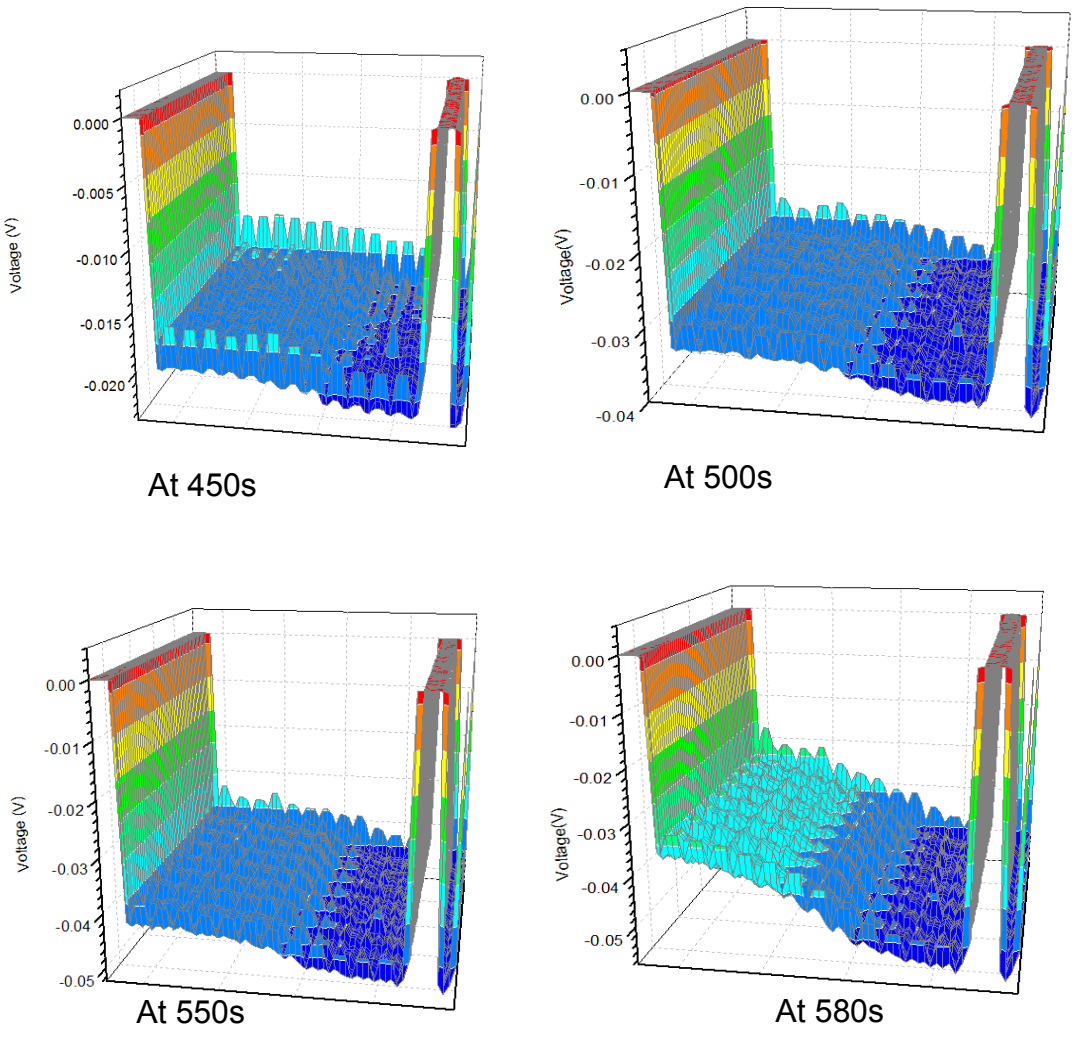

Fig. 6.2: Spatial monitoring of the 64x64 ISFET array

These three-dimensional graphs in Fig. 6.2 detail the temporal progression of voltage on the surface of the array. The x and y axes are the co-ordinates of the pixels in the array (64 x 64) and the z axis is the differential voltage amplitude. It goes below zero to show descending voltage amplitudes. We can notice two 'walls' in two sides of the array. That's nothing more than dead pixel columns, which carry no information whatsoever. Apart from the expected drift of the chip, part of the array, almost half, experiences an additional voltage difference reaching 20 mV. We presume that this difference is caused by the precipitate that is formed probably partially on the array. The voltage difference stabilises after 130 seconds – from 450 to 580 seconds. Thus we presume the precipitate formation takes approximately 2 minutes. Unfortunately it was not possible to conduct further experiments to reach a more definitive result and to further analyse the data.

6.3 Temporal and spatial study of the glucose-hexokinase reaction

6.3.1 Glycolysis – Hexokinase reaction

One of the most important reactions happening in a living organism is glycolysis. It is a reaction responsible for energy production and it is considered to be one of the oldest known metabolic pathways in nature [58]. The reaction consists of ten steps with glucose as the initial substance converted to pyruvate, with a specific enzyme involved in each step. Hexokinase is the enzyme involved in the first step of the glycolysis reaction. It is used to catalyse the conversion of the initial glucose molecule to glucose 6-phosphate (G6PD), by way of ATP. The ATP is used to provide the phosphate group priming glucose and to prevent it from being exported out of the cell. This first step is called Hexokinase Reaction due to the enzyme used and can be seen analytically in Fig.6.3.

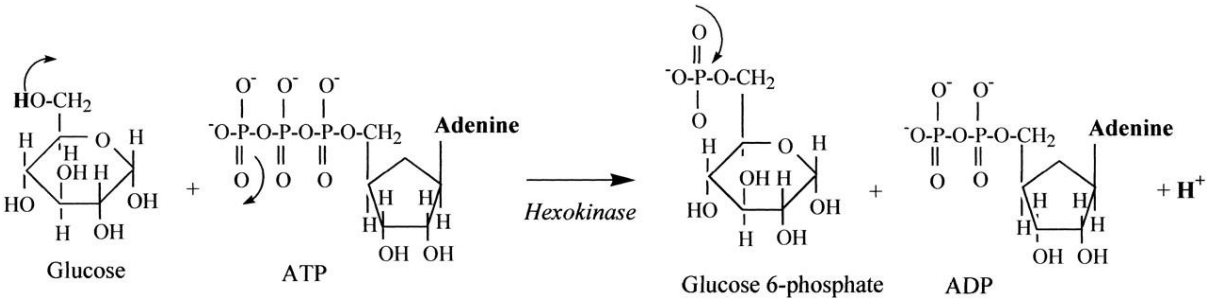

Fig. 6.3: Glucose and ATP reaction in the presence of Hexokinase [59]

The important issue in our research is that the Hexokinase reaction has an ionic character. It liberates a proton (H^+) that can directly be detected using the ISFET array which can be used as a measure for enzymatic activity.

6.3.2 Enzymatic behaviour and biosensors

Enzyme behaviour and its detection with sensors has been of high interest in biomedical engineering so far. For example, glucose oxidase is a well established enzyme for monitoring diabetes [60], sarcosine oxidase has been used as an indicator for prostate cancer [61], alcohol dehydrogenase also as an indicator for liver damage and Parkinson's disease [62]. These examples of metabolomic biosensors have led to the conclusion that direct measurements of certain metabolites can lead to the development of stratified medicine [63], resulting to a more personalised approach of diagnosis and treatment for many diseases.

Other laboratory methods, like mass spectroscopy have been used also to study groups of metabolites in patients with stroke [64], which analysis has detected certain metabolite trends leading to advanced diagnostic methods of early prognosis and appropriate prophylactic therapy. However, mass spectroscopy based in a laboratory is not the most convenient diagnostic means. A low cost, high volume technology is required such as Ion Sensitive Field Effect Transistors (ISFETs) that have been shown to work as potentiometric sensors in enzyme assays and in the formation of large arrays can be an adequate and effective method for chemical imaging [6] [1] and also genomic technologies [38].

This section is about presenting how an ISFET array can be used with hexokinase enzyme. We further show how the array can be used to observe the spatial and temporal dynamics of the enzyme assay over the surface of the ISFET array,

allowing the reaction rate to be monitored. This was accomplished using an enzyme immobilisation technology that shows some perspective for a future development of a multi-enzyme assay tool.

6.3.3. Hexokinase enzyme assays

The enzymatic activity of hexokinase (Sigma) was initially evaluated spectrophotometrically by varying the concentration and pH of different buffers; each buffer had a specified buffering range. For the spectrophotometer assay the following final concentrations were used: 25 mM sodium phosphate buffer pH 7.6, 216 mM glucose; 0.74 mM ATP; 7.8 mM $MgCl_2$; 1.1 mM b-nicotinamide adenine dinucleotide phosphate (b-NADP); 1.25 Units of glucose-6-phosphate dehydrogenase; and 5 Units hexokinase. For Hexokinase, 1 Unit will phosphorylate 1.0 µmole of D-glucose to D-glucose-6-phosphate per minute at 25 ˚C. For G6PDH, 1 Unit will oxidize 1.0 µmole of D-glucose-6-phosphate to 6-phospho-D-gluconate per minute in the presence of b-NADP at 25 ˚C. An example using sodium phosphate buffer is shown in Fig. 6.4. A final buffer concentration of approximately 25 mM gave the highest enzyme activity; hence this concentration was used in subsequent chip measurements.

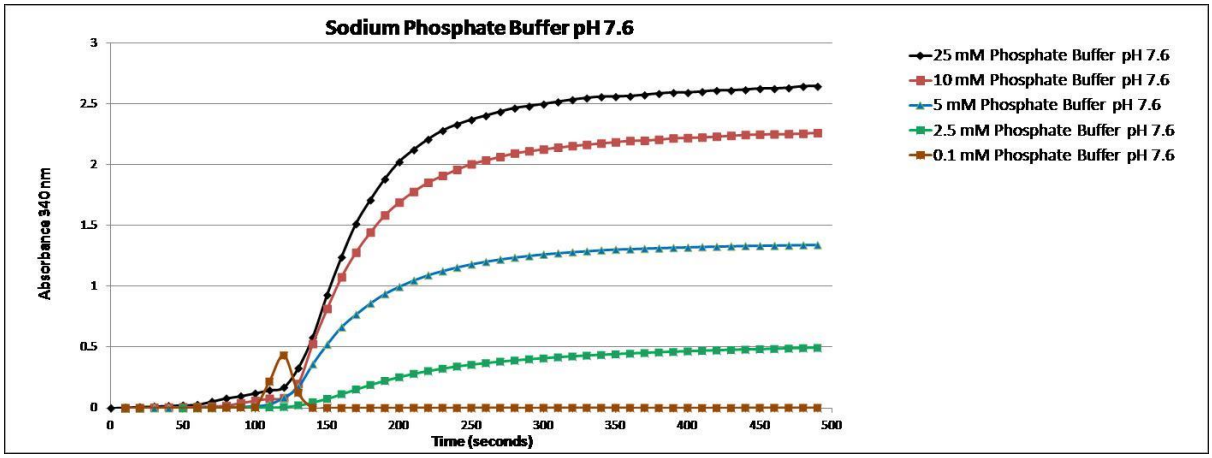

Fig. 6.4: Enzymatic activity of Hexokinase measurements using a spectrophotometer. Sodium phosphate is a common buffer solution and has a pH range of 5.8 – 8.0.

6.3.4 Cyanogen bromide-activated-Sepharose® beads

In order to immobilise hexokinase on top of the ISFET array sensor so as to form a layer whereby the reaction can take place, hexokinase was covalently coupled to cyanogen bromide-activated-Sepharose® 4B micro-beads (Catalog Number C9142) from Sigma-Aldrich, consisting of 4% agarose, varying from 40 to 165 μm in diameter. The beads were used according to instructions provided [65] (in '*http://www.sigmaaldrich.com/content/dam/sigmaaldrich/docs/Sigma/Product_Information_Sheet/c9142pis.pdf*' with the technical support of Institute of Infection, Immunity and Inflammation of the University of Glasgow. Cyanogen bromide reacts with hydroxyl groups on agarose and forms cyanate esters or imidocarbonates as shown in Fig. 6.5. The resulting structure is an imidocarbonate with no net charge.

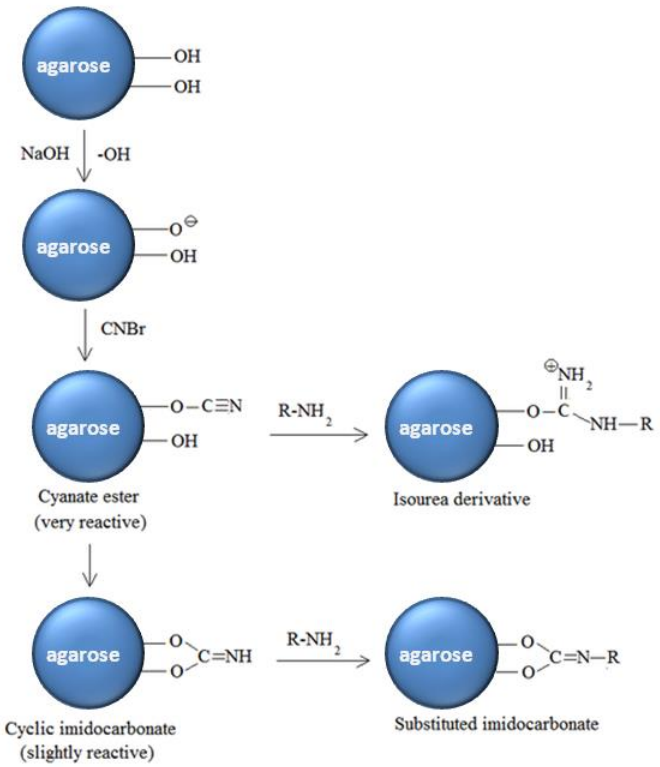

Fig. 6.5: Immobilisation reaction of hexokinase to Sepharose® beads (Sigma-Aldrich® product information sheet) [66].

The hexokinase sepharose® beads were washed thoroughly with 25 mM sodium phosphate buffer prior to each assay.

6.3.5 The glucose-hexokinase measurement setup

In order to monitor the hexokinase reaction and investigate its activity, we first added 750 µl of hexokinase-sepharose beads and allowed the beads to settle to the bottom of the sensor container to form an active layer. A top view of the array without and with the beads can be seen in Fig. 6.6.

Fig. 6.6:. Top view of the array sensor (a) without beads and (b) with settled beads.

6.3.6 Temporal response

After the beads had settled, 0.2 ml of 25% Glucose and magnesium chloride (a source of Mg^{2+} cofactor) were added gently to the surface of the liquid, away from the array. The solution was then left to diffuse for several minutes before ATP was added. Since hydrogen ions are liberated from the enzyme reaction, the

resulting potentiometric measurement was expected to be a voltage increase (and accompanying pH decrease). This increase was indeed observed and can be seen in Fig. 6.7.

The addition of the ATP activated the ionic reaction of the glucose/hexokinase. The voltage on the surface of the sensor increased reaching a plateau after 5 seconds creating a difference of 65 mV. Glucose and ATP facilited by hexokinase presence reacted according to equation 6.3 producing protons on the surface of the chip. This result can be cross referenced with literature where similar glucose ionic reactions such as the one mentioned in 3.5 from Park et al. measurements [43]. Our curve follows the same exponential trend reaching a plateau. Park measured the ionic reaction to give an increase of 85 mV, the same order of magnitude as ours, however using a silicon nitride/tantalum pentoxide as a base insulative layer which provides a slightly bigger sensitivity (see Table 3.1)

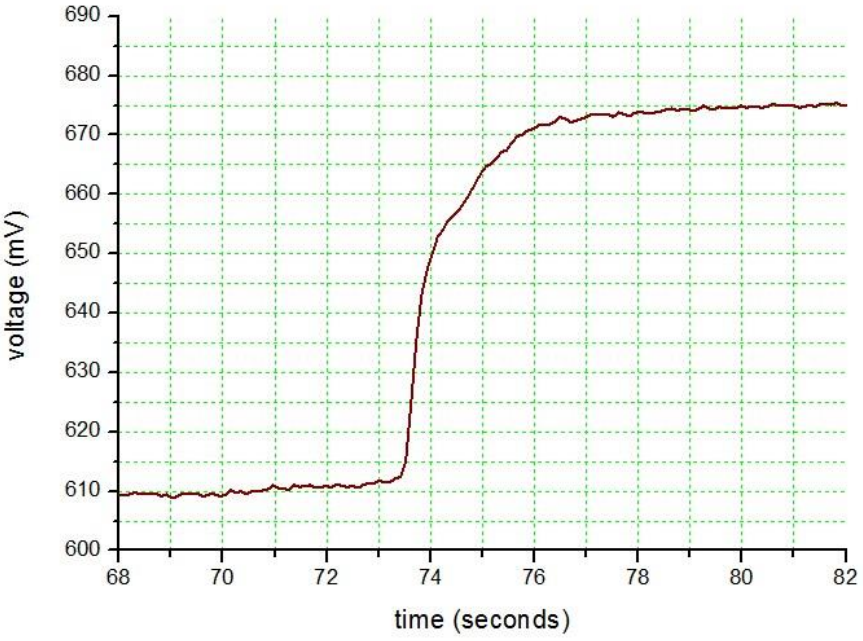

Fig. 6.7: Single pixel voltage increase of 65 mV when the ionic hexokinase reaction took place on the ISFET sensor array.

6.3.7 Spatial distribution

A spatial distribution of the reaction can be seen in Fig. 6.8. A 36 x 64 area pixel is presented in sequential time frames using t_o=0 as a datum reference. We observed that the reaction needs approximately 40 time frames (4 seconds; 10

frames/sec) to spread from the edge to the middle of the array. As evident in Fig 6.8, the reaction spreads from circular areas. In Fig 6.8(a) we see a half-circular pattern monitoring the beginning of the reaction pattern in the bottom centre of the array. The observable reaction spreads to adjacent areas, also following a curved pattern, which can be seen from the edges of the pattern, shown in Fig 6.8(b). Moreover, in Fig 6.8(b), there is another initiation of the reaction in the middle right area also with the same circular pattern. The shape of the pattern as the reaction spreads is a consequence of the added glucose reacting with the immobilised enzyme on the sepharose beads.

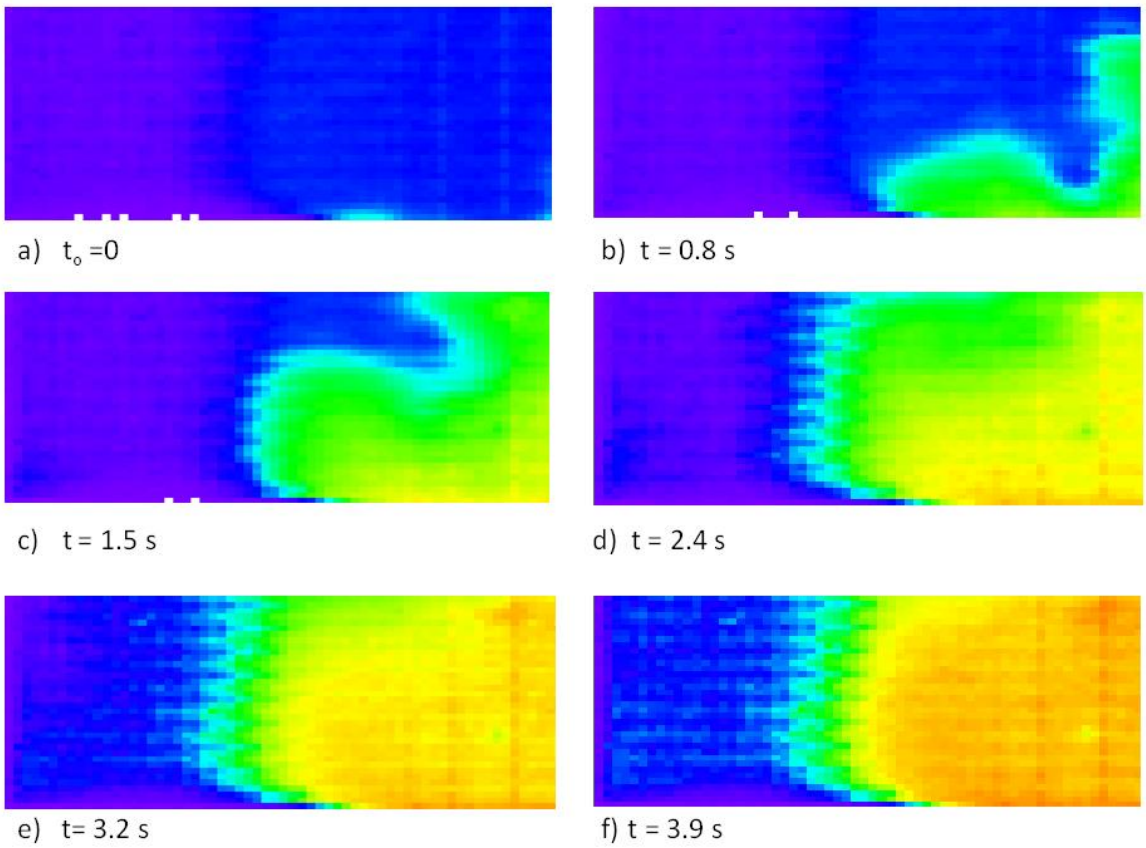

Fig. 6.8: Spatial distribution of the Hexokinase reaction over time

Examining the reaction in two dimensions we see ionic activity starting from the bottom middle/right in 6.8a) expanding circularly while another starts in 6.8b) expanding also in the same manner.

The reaction seems to cover a little more than half of the presented area while the rest seems inactive. This area of the chip was previously contaminated and

almost destroyed so couldn't present adequate sensitivity. Thus, our two dimensional observation of the reaction is therefore limited only to the right area presented.

The idea that this part of the chip was not covered with sepharose beads doesn't seem possible, as the beads were also observed that they have spread uniformly before the experiment.

6.3.8 Diffusivity

The contour map of the sensor array in Fig. 6.8 shows the spread of the reaction from pixel-to-pixel. As we have already shown, we can observe the rise of the signal voltage on a single pixel of the array (Fig. 6.7). In order to quantify the rate of movement of the reaction we have chosen several voltage thresholds, and then plotted the time taken for pixels along a straight line to respond and reach the threshold. The line we chose was on the path with the most rapid forward propagation of the reaction contour. Since a pixel is 10.2 microns, we calculated the distance traversed by the constant potential contour and plotted the data as shown in Fig. 6.9. The relationship between the diffusivity coefficient and the mean distance traversed is shown in Equation 6.1 [67].

$$\sqrt{\bar{x}^2} = \sqrt{2Dt} \qquad (6.1)$$

Where x is the distance travelled, the time and D the diffusivity coefficient. Using data fits from the graphs in Fig. 6.9, we found the mean value of diffusivity coefficient to be $3.5 \cdot 10^{-5} cm^2 \cdot s^{-1}$. For comparison, the diffusivity coefficient of hydrogen ions in water is $9.3 \cdot 10^{-5} cm^2 \cdot s^{-1}$ and for glucose it is $0.67 \cdot 10^{-5} cm^2 \cdot s^{-1}$. The value we measured was closer to the value for hydrogen ions in water. We therefore conclude that the measurement we observed is not limited by the diffusion of glucose. It is likely that we are detecting H^+ ions diffusing rapidly over the sensor, inhibited by the presence of the beads.

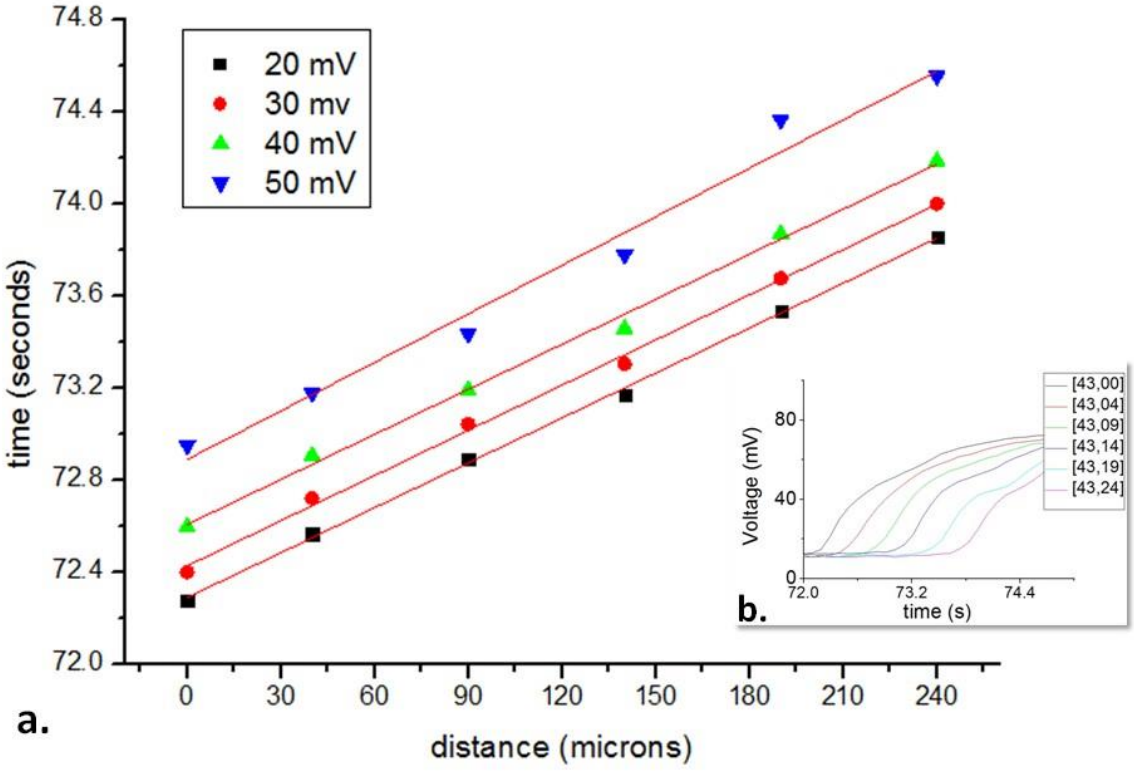

Figure 6.9. (a). Time taken for pixels along a straight line to reach a selected voltage threshold. (b). The voltage on 5 pixels along a straight line as a function of time.

6.3.9 Control experiments

Because of the acidic pH of ATP in water (pH 3.5), a control experiment was conducted to confirm that the rise on the output voltage was due to the protons generated by hexokinase and not by the addition of ATP. We added glucose without coupled hexokinase beads, and after approximately 1050 frames (105 seconds) ATP was added. As seen in Fig. 6.10a, the addition of ATP had no effect on the voltage difference.

The experiment was then repeated this time with extra buffer added. The red graph in Fig. 6.10b shows the same output voltage difference created with the addition of glucose and ATP solution to the hexokinase bead layer, but this time the signal was attenuated within 100 frames (10 secs). This might be because of the existence of excess buffer counteracting any change in pH caused by the generation of hydrogen ions. To confirm that the signal observed was generated by hydrogen ions produced by an enzymatic reaction, a control experiment was

conducted using sepharose coupled bovine serum albumin (BSA), a non-enzymatic protein. As expected, there was no signal evident.

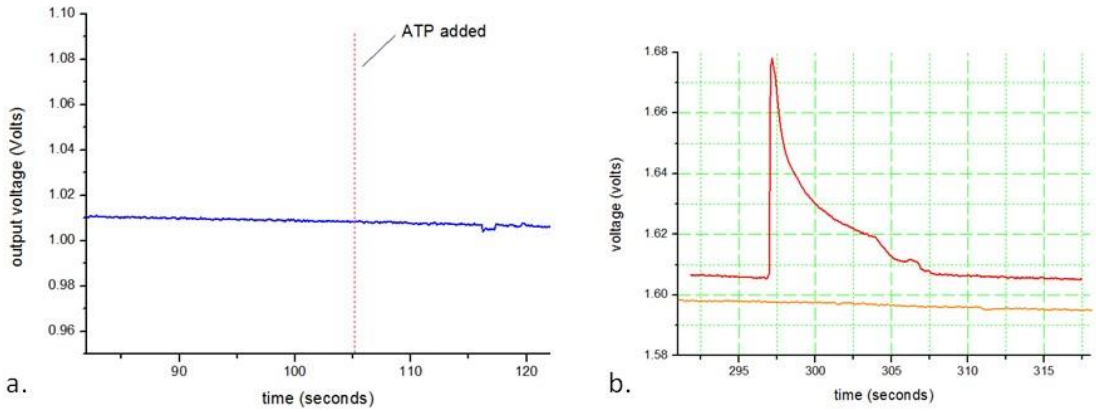

Fig. 6.10 (a). Addition of ATP in the absence of hexokinase beads caused no effect to output voltage (b). Hexokinase reaction with the use of buffer in excess and control experiment with bovine serum albumin.

6.4 Summary-Conclusion

We used the 64 x 64 ISFET array sensor to monitor a possible precipitate formation using the papain enzyme. First preliminary tests showed an ionic change which might be linked with the activation of the papain and Ti(BALDH) (Titanium(IV) bis (ammonium lactato) dihydroxide) salt. We observed the first temporal and spatial representation of an ionic reaction related with enzyme.

However, the most important section of this chapter is the experiment regarding hexokinase enzymatic activity. The sensor successfully detected and monitored the production of hydrogen ions as evidenced by a change in voltage. In the single pixel view, we observed temporal dynamics. The voltage amplitude increased by 65 millivolts when the hexokinase reaction took place, compared with the value of 85 millivolts we had from literature [43] (seen in Literature Review chapter) for similar ionic reactions with enzyme- immobilized layers for glucose detection. We also used the array in an imaging mode in order to observe the progress of the enzyme reaction across the surface of the chip. The progress of the reaction contour could be adequately modelled using a simple diffusion relation, allowing possible future prediction of the speed at which

materials on a chip's surface will mix. The use of sepharose® beads appears to slow down the rate of diffusion, increasing the time available for ideally independent reactions to occur. We found the mean value of diffusivity coefficient to be $3.5 \cdot 10^{-5} cm^2 \cdot s^{-1}$. We conclude that the device, and the system of immobilisation and measurement we have demonstrated, can be used for novel methods of glucose detection and may, with further work, be used for the detection of multiple enzymes on a single chip to facilitate a broad spectrum metabolomic screening device, the integration density of which will be limited by the diffusion rate of H^+ ions in the medium.

7. Experiments with cyanobacteria

7.1 Introduction-Motivation

This chapter is about the presentation of experiments related to the ionic activity of the prokaryotic organism Synechocystis sp. PCC 6803 [68], a cyanobacterium capable of photosynthesis and also with the ability to maintain a circadian clock (Fig.7.1). Synechocystis as an autotroph that is also able to perform a set of other biochemical reactions to produce energy such as respiration and nitrogen fixation. We attempted to monitor all this activity with potentiometric measurements with the use of a Ion Sensitive Field Effect Transistor (ISFET) Array we developed using a standard 0.35 μm austriamicrosystems CMOS technology.

Motivation for this set of measurements is that cyanobacteria is a promising source of renewable energy, as it is already known that fossil fuels are limited. Cyanobacterial cultures grow easily with basic nutritional requirements and solar energy. Their cultivation is therefore inexpensive and elementary [69]. Although we examined various signals which showed a periodic bacterial activity, we focused mostly on the light-depended behaviour of the culture linked with photosynthesis, with the perspective to regard it as a potential energy producing photovoltaic cell.

7.2 Synechocystis sp. PCC 6803

Cyanobacteria are considered to be amongst the most ancient living organisms of the planet. Their ability to generate oxygen changed Earth's atmospheric chemistry dramatically allowing aerobic organisms to dominate the planet [70].

Synechocystis sp. PCC 6803 belongs to the big family of cyanobacteria with the ability to photosynthesize, that is to create chemical fuels using a light source. A more detailed representation of this process can be seen in Fig. 7.2: The photosynthesis mechanism of the bacterium cell consists of two photosystems, photosystem I (PS I) and photosystem II (PS II) which are the parts of the cell interacting with light and thus maintaining an electron cycle resulting in pumping protons (H^+) across the cell's thylakoid membrane. Electrons are transferred via certain cytochromes (cyt) to ATP synthase (ATPase) resulting finally in the production of the chemical fuel ATP from ADP.

Synechocystis sp. PCC 6803 has also been examined as a promising biocatalyst for electricity generation in research regarding microbial fuel cells [71]. The genome of *Synechocystis* sp. PCC 6803 was fully sequenced in the 1990s [72] [73] which made it a very popular model organism for photosynthetic monitoring. Also, given that cyanobacteria are the biggest oxygen producer on the planet [74] –considering also pelagic cyanobacteria that live in the oceans- the study of cyanobacteria is of significant interest.

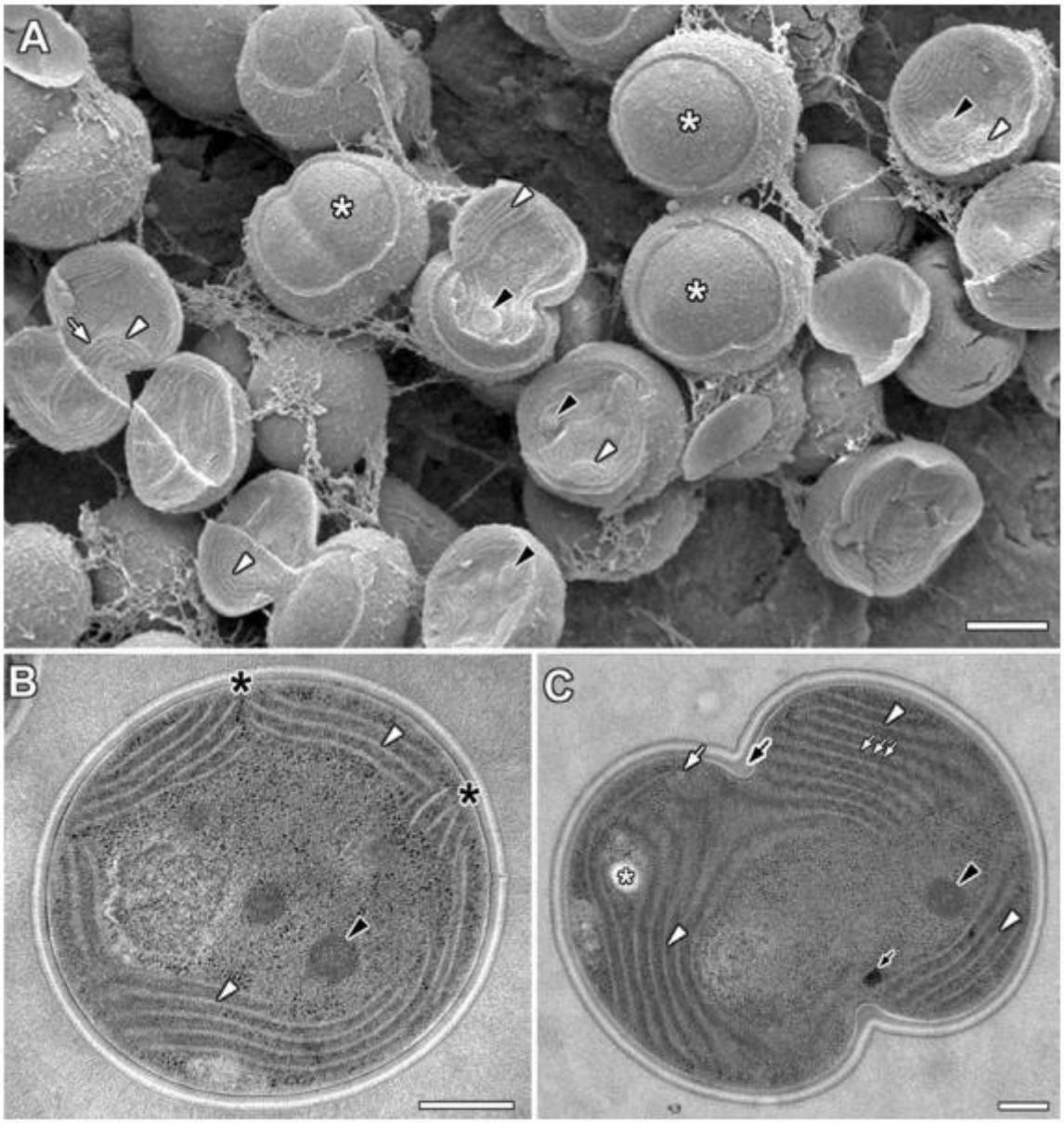

Fig: 7.1 Cells of the cyanobacterium Synechocystis sp. PCC 6803 a: Cryo-SEM image of high pressure frozen and freeze-fractured cells. Bar = 500 nm b: TEM image of a non-dividing cell. c: TEM image of a cell in early division. Bars = 200 nm [70]

Another significant aspect of cyanobacteria is that they are the only bacterial species that have a circadian clock [75]. In biology, a circadian rhythm is an oscillation happening in many of the organism's functions which coincides with the 24h day and night cycle [75]. There are specific genes which control this process and there are also studies to show that these circadian rhythms can be also demonstrated in darkness [76] or under continuous illumination [77] under certain treatment.

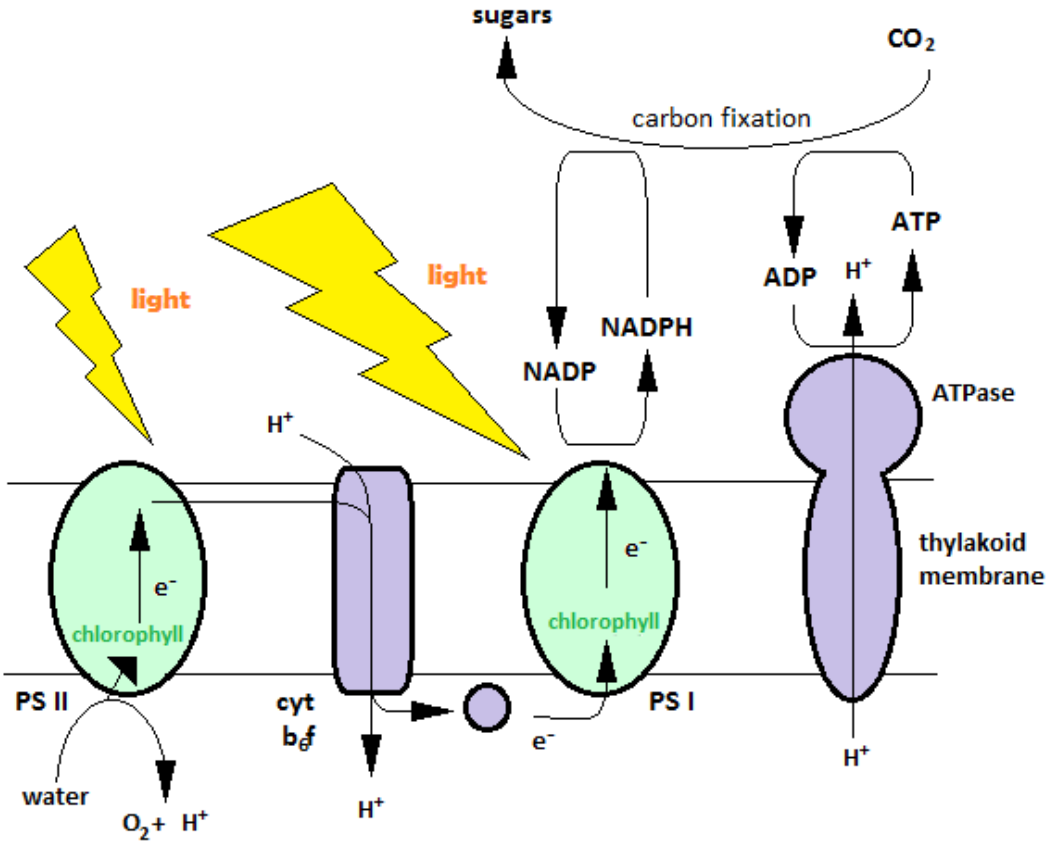

Fig. 7.2: A schematic representation of the photosynthesis process happening in the thylakoid membrane of a cell.

7.3 Bacterial culture preparation

A liquid culture of the wild type cyanobacterium, Synechocystis sp. PCC6803, was prepared photoautotrophically in the Cronin group, Department of Chemistry, Glasgow University, from a single colony of plate-grown cells provided by Dr Andrew Hitchcock from the National Oceanographic Centre, Southampton, to an optical density of around OD_{750} = 1.0. Cells were then harvested by centrifugation (30min at 4400rpm) and re-suspended in fresh growth media prior to use. Initial growth conditions consisted of constant illumination under a full spectrum light source, shaking at 150rpm and the standard growth media, BG-11 [78] - a widely-used nutrient broth providing the major salts and trace minerals required for healthy growth.

7.4 Fast oscillations

Our preliminary experiments with the Synechocystis cultures showed a fast oscillating activity. We kept the cyanobacteria in a broth solution and further diluted, to approximately six times less concentrated than the initial solution, reasoning that by doing this the light would reach the sensor surface more readily. The broth was inserted inside the ISFET chip reaction chamber (Fig. 7.4). We managed to detect an oscillating signal of 2-3 mV amplitude and a period of 20 seconds, as seen in Fig. 7.3. Further tests showed that these oscillations were light independent, so they might be related with activity of the heterocystous cells of the culture, as opposed to the vegetative cells which are photosynthetic. [77] [79]. It is also suggested that there can be oscillating activity mostly linked to nitrogen fixation or carbohydrate degradation under continuous illumination [77]. Mostly oscillations refer to activity related to the circadian circle of the culture, but there have been studies [80] showing that events can occur also in the time span of seconds, when protons are monitored.

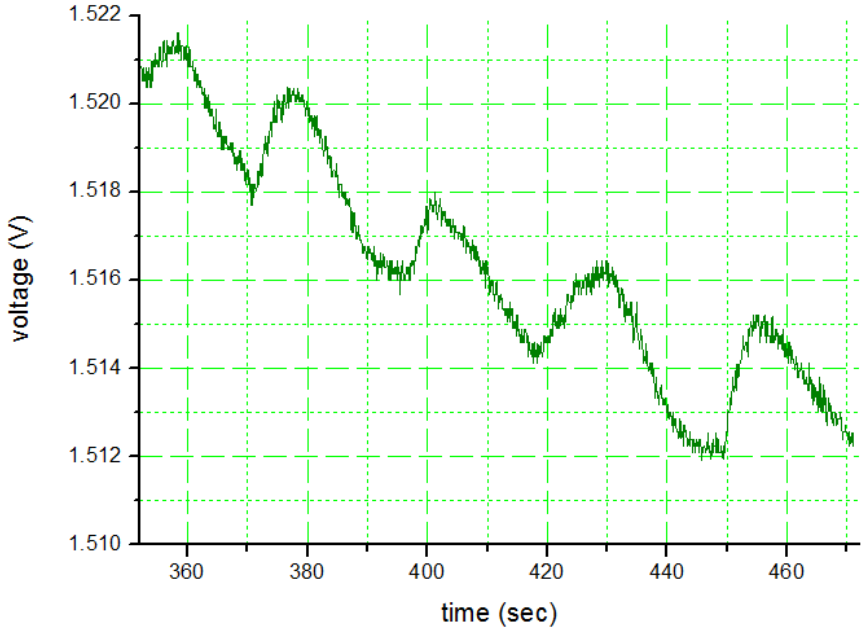

7.3 Fast oscillations detected in a broth of Synechocystis sp. PCC 6803

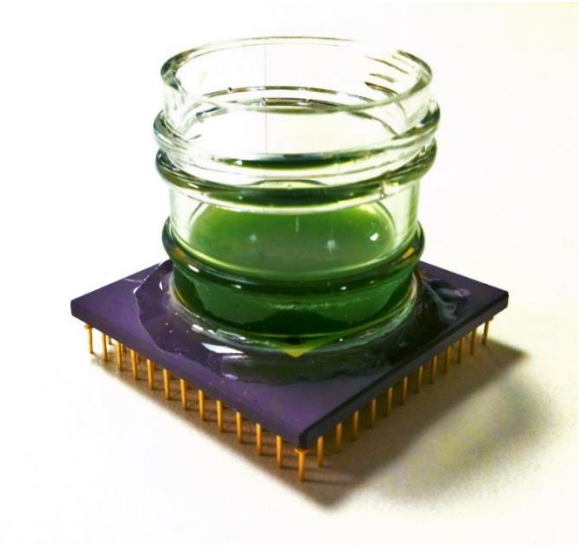

7.4 Picture of the ISFET chip filled with a broth of cyanobacteria in BG-11 growth media

7.5 Developing biofilms and growth of culture in the dark

The approach to study cyanobacteria as a broth of cells eventually brought up problems with the interface of the silicon nitrate sensitive membrane of the ISFET sensor array. As the solution of BG-11 with the cyanobacterial culture was inserted into the chip's container, most of the cells remained suspended in the broth making it difficult for the sensor to monitor them for more precise measurements. To optimise sensing, cells needed to be grown as films so they could form a better interface with the array sensor (see Fig. 7.5), a tactic also seen elsewhere [44].

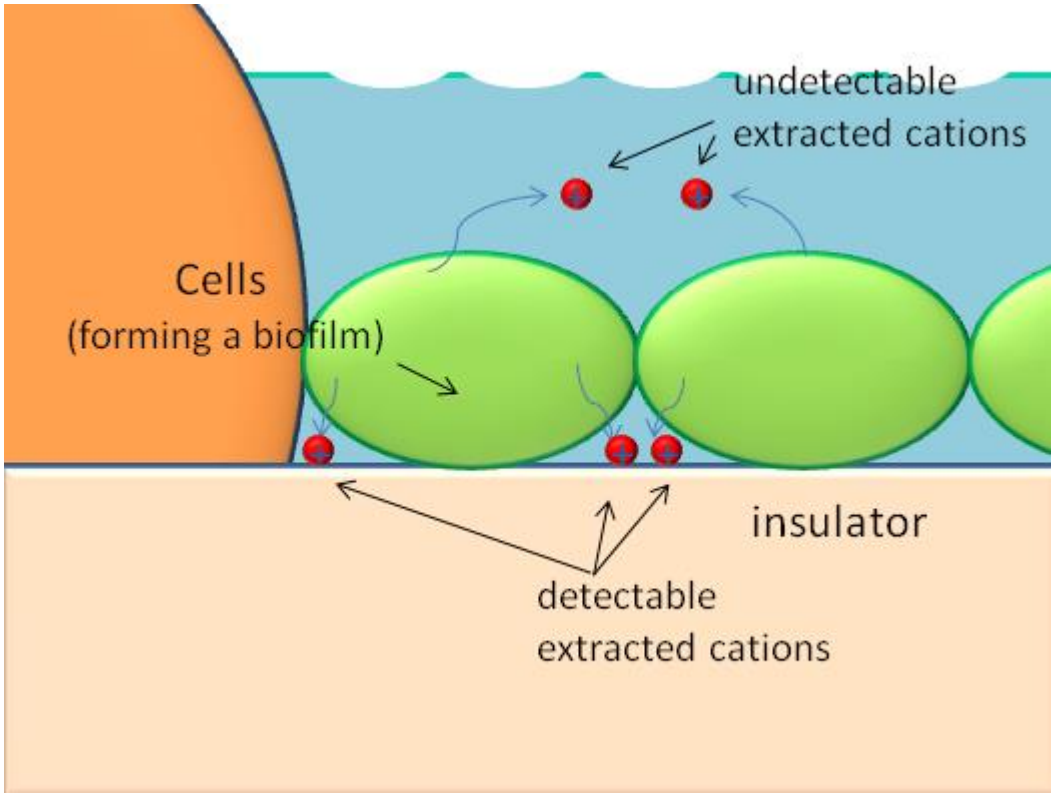

Fig.7.5: A graphic representation of a biofilm formation.

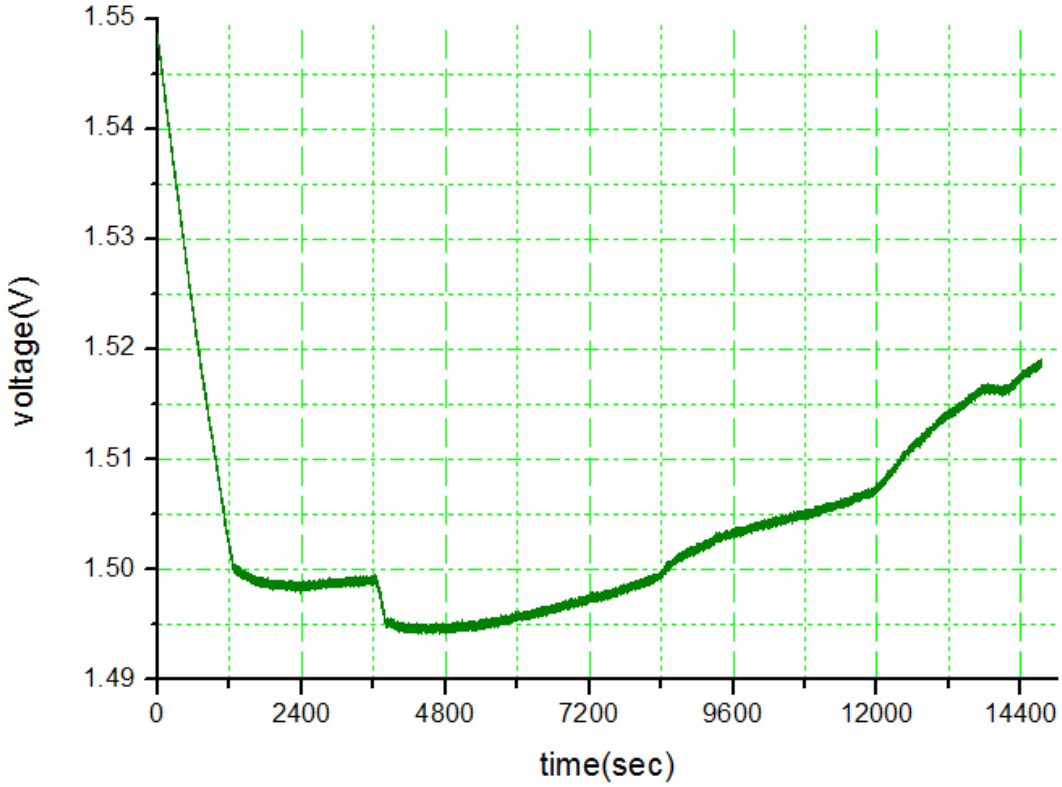

Fig.7.6 Synechocystis PCC 6803 activity in darkness. Settling culture, growth and possible proton diffusion into cells.

We added the broth, BG-11 with the cells, trying to keep the volume of solution on top of the array sensor as small as possible so that the cells will precipitate faster and the liquid will eventually evaporate leaving us with a gelatinous mass of the cells attached on the surface. The whole procedure was conducted with no source of light, in the dark. The 600 μl of the broth remained in suspension until 1020 seconds, that is approximately 17 minutes. Then cells began to settle onto the array surface. For these first 17 minutes the voltage monitored kept the chip's characteristic drift. Then various pixels of the ISFET chip presented a signal as can be seen in Fig.7.6. Settling time behaviour and similar trend has been reported also before [81]

After settling, the cyanobacteria maintained a steady state for 2400 seconds approximately and then moved to a new ascending state for almost 4800 seconds. Then a new cycle of increase started lasting 3600 seconds and then another one for 2400 seconds this time.

The voltage kept increasing and the experiment stopped after 14400 seconds. We assumed that this increase of voltage indicates the production of different ions in the solution, as seen also in literature [81]. Moreover, this production of cations which are diffused out of the cells makes the solution more acidic and probably some reactions with the growth medium solution can occur [80]. The bacterial behaviour of Fig. 7.6 can be summarized in a tabulated form in table 7.1.

behaviour	culture settling	steady state	ascending curve	ascending curve	ascending curve
Time (sec)	0-1040	1040-3400	3400-8200	8200-11800	11800-14400

Table 7.1: Synechocystis PCC 6803 activity in darkness. Settling culture, growth and possible proton diffusion into cells

7.6 Photosynthesis. Interaction with light

The most important feature of the cyanobacteria Synechocystis PCC 6803 is its ability to convert light to chemical energy, an operation called photosynthesis. Cyanobacteria are the only organism besides plants able to perform photosynthesis and the only bacterial species to have a circadian clock [82]. After managing some control over the Synechocystis culture and being able to form biofilms, we proceeded to perform experiments involving light and darkness intervals.

First, the response of the ISFET sensor array was examined without any culture on it, only with the BG-11 solution. The device presents a drift which is a built-in property of the array due to its electronic design (see paragraph 5.7). After several tests we concluded that the drift was increased during the light-on intervals, going back to its normal intensity during light-off intervals as can be seen in Fig. 7.7. Tabulated results can be seen in Table 7.2

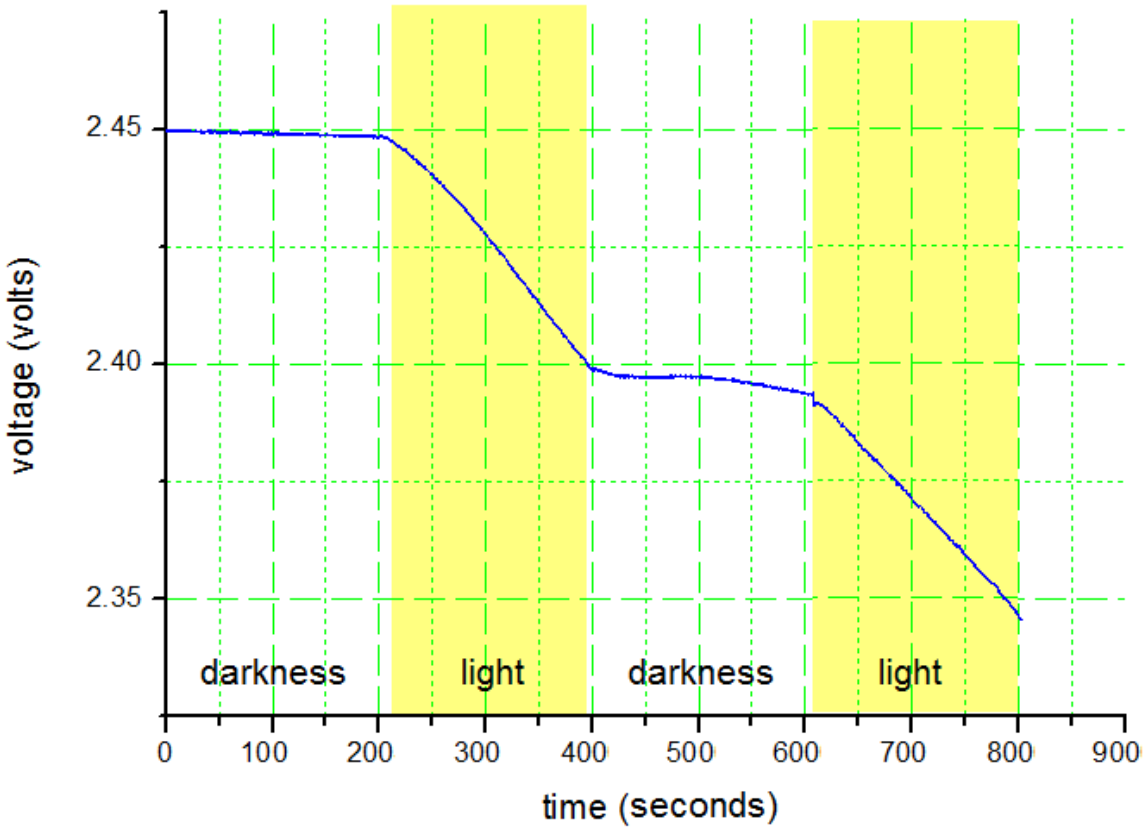

Fig. 7.7: Control experiment studying the behaviour of the ISFET sensor during dark-light intervals. Solely BG-11 solution was used for intervals of 200 seconds with the following pattern: dark-light-dark-light.

light state	darkness	light	darkness	light
control solution	steady at 2.45	drift 2.45V→2.4V	steady at 2.4V	drift 2.4V→2.35V
time (sec)	0-200	200-400	400-600	600-800

Table 7.2: Tabulated results of the control experiment of Fig. 7.7.

The light source used for this experiment was light from a fluorescent tube of approximately 5200 to 5800 lumens from a distance greater than 200 centimetres to avoid major thermal effects on the sensitive surface of the chip.

In the second phase of our experiment, we worked on settling the culture in an appropriate way to get the most efficient signal, which means establishing the culture in a biofilm form. The culture needs to settle from a minimum amount of

BG-11 and form a precipitate. Then the solution needs to evaporate leaving a gelatinous layer of the culture. The culture can stay active as long as it stays moist, so there is approximately a 4 hour time space for any experiment to be performed. After several trials we concluded that the most appropriate time interval to be monitored was 15 minutes. When the biofilm was ready we performed a 45-minute experiment consisting of 15-minute intervals of darkness, light, and darkness respectively. The results can be seen in Fig. 7.8.

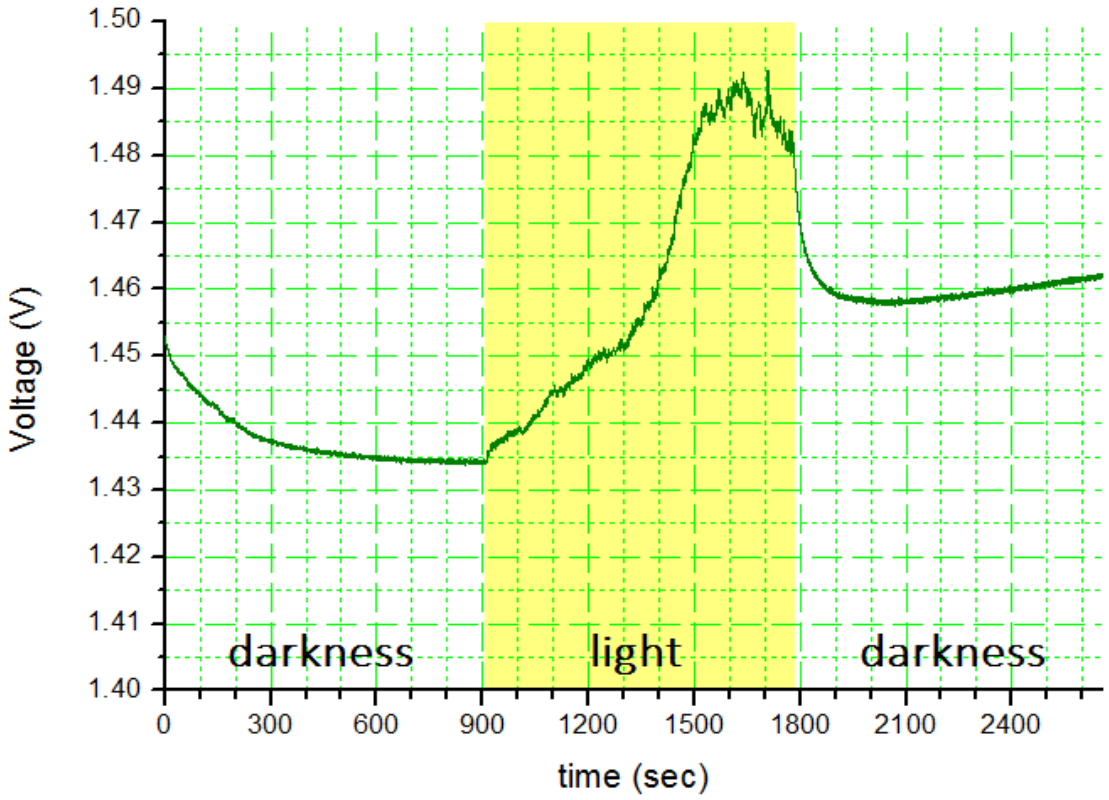

Fig. 7.8: Photosynthesis monitored in real-time with the ISFET sensor. Establishing a 15-minute light interval between two 15-minute dark intervals we were able to create a 'biological light switch' with a voltage signal reaching 55 mV.

The first 15 minutes –approx. 900 seconds- the culture followed a fast exponential drift in voltage and remained stable for the most of the interval.

During the light-on interval, the culture followed an upward trend which reached a plateau after 600 seconds –ten minutes approx.- resulting in an increase of 55 mV. When light was off again, the signal followed again an exponential decline and then stabilised with a small upward drift. Similar results with biological light switches has been also reported by Bombelli et al. as mentioned previously in literature (paragraph 3.6) [44]. Bombelli used cyclic voltammetry techniques to measure photosynthesis of cyanobacteria implementing electrodes coated with different conductive polymers and other electron mediators [44]. A voltage difference of 33.7 mV during light-off light-on intervals was reported, similar to our light-off light-on experiments. Figure 7.9 presents: a) biofilm and device of Bombelli's work and also b) voltage response during light-off light-on intervals.

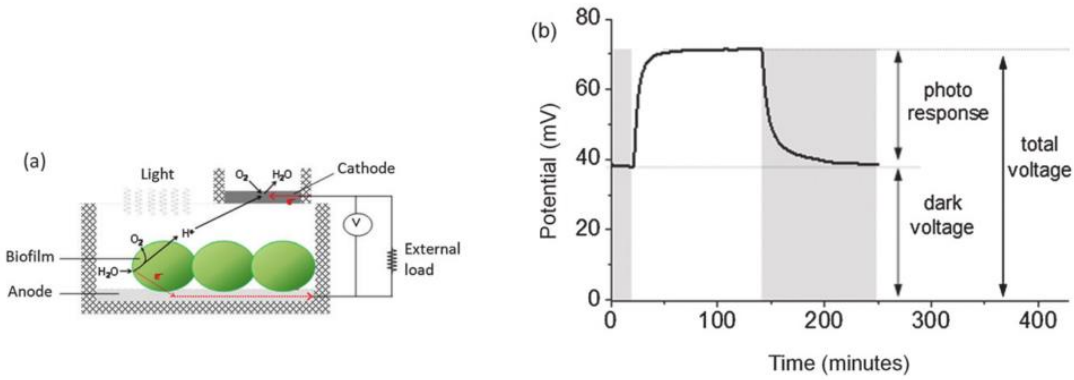

Fig.7.9: a. biofilm of cyanobacteria and measuring unit. b. voltage response of the photosensitive device

Coming back to our measurements, we can also notice that in the second darkness period the stable amplitude of the voltage was at a greater value to before irradiation, probably implying some kind of a hysteresis occurring, most likely due to culture's interaction with the chip's surface.

The same experiment was conducted with no bacterial culture, just with plain BG-11 solution to stand as a control of our results. The control experiment can be seen in Fig 7.10.

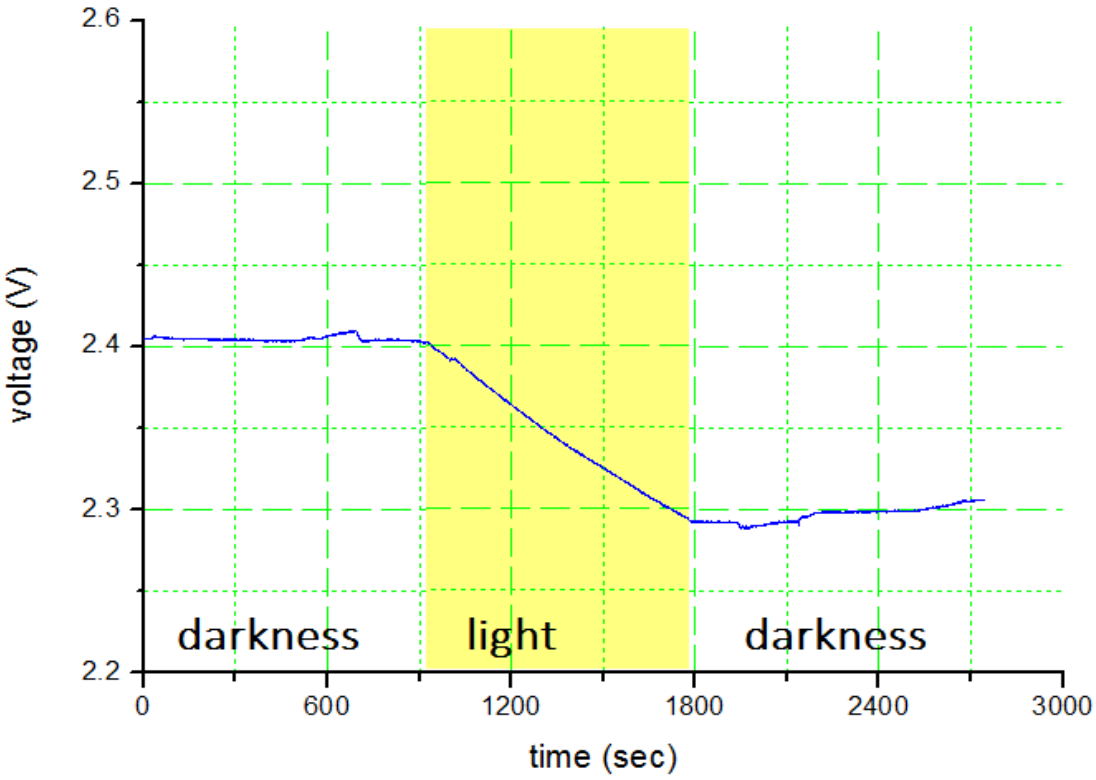

Fig.7.10: Control experiment using solely BG-11

From the above figure we can understand that the ascending signal during the light-on interval comes to contrast more –in fact counteracts- the expected drift of the control experiment. This leads us to presume that if the drift was somehow eliminated the amplitude of the voltage when light is on might reach an even higher value.

Below in Table 7.3, the results of this measurement are presented in a tabulated form for the reader's convenience.

light state	darkness	light	darkness
bacterial culture	drift 1.45V→ 1.43V	ascending voltage reaching peak at 1.49V	voltage drop at 1.46mV ±0.5 mV
control solution	steady at 2.4	drift 2.4V→2.3V	steady at 2.3V
time (sec)	0-900	900-1800	1800-2700

Table 7.3: Results of the light-depended experiment with darkness and light intervals with bacterial culture and control solution compared.

Data from the photosynthesis experiment as shown in Fig. 7.8 provided us also with a spatial representation of the measurement which can be depicted in a contour map of the surface of the ISFET sensor array in relation to the voltage amplitude. The progression of the measurement over time can be seen in Fig. 7.11.

In the 1250s frame, the area is covered with green colour which according to the countour map is somewhere in the middle. From Figure 7.8 we see that this corresponds to 1.45 V. Next frame 1450s, we see already a big increase since we are in the light-on period corresponding to 1.47 V, 20 mV more than the previous frame. At 1650s, we reach the peak of 1.49 V. The next frame at 1850s is now in the light-off period. The voltage has decreased as the culture doesn't react with the light anymore and falls to 1.46 V.

We observe that the voltage change is uniform to this 20x20 area of the array, implying that the biofilm has been deposited properely on the surface.

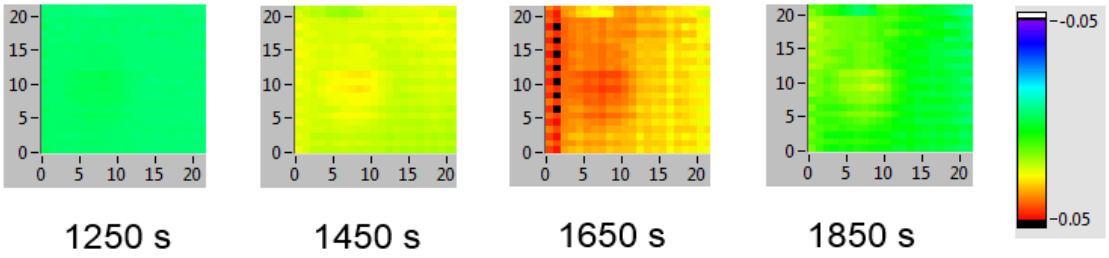

Fig. 7.11: Contour voltage difference maps of a selected area of 20x20 pixel on the ISFET array with green showing minimum and red maximum respectively.

7.7 Summary-Conclusion

This chapter was about the bioelectochemical behaviour of Synechocystis sp. PCC 6803, a cyanobacterium found in abundance in nature. Cyanobacteria are capable of photosynthesis and contribute dramatically to oxygen production on the planet along with plants. We managed to monitor temporally oscillating signals of the organism when the bacterial cells remained in a broth mode. For a more systematic observation of the cyanobacterial culture we needed to form biofilms of the culture in order to acquire accurate measurements. Experiments

showed that the biofilm was formed after 20 minutes of resting on the chip surface. Similar behaviour of an initial drift and then a slow periodic activity was recorded before in bibliography (see 7.5) Moreover, inducing darkness-light intervals including also the appropriate control experiments with no bacterial layers, we managed to demonstrate that there is increased ionic activity rising the voltage amplitude to 55 millivolts when the culture on the chip was illuminated probably due to the photosynthetic ability of the Synechocystis.

8. Conclusion and Future work

8.1 Conclusion

In this thesis the achievements and scientific work of a 64 x 64-pixel ion camera fabricated in an unmodified 0.35 μm CMOS technology has been presented. Conclusions and the important outcomes of the measurements and experiments will be presented in the following sections.

8.1.1 The array chip system

We used an array of ISFET sensors previously designed and fabricated in order to monitor and measure chemical and biochemical reactions in real time. The area used was a 4.2 x 4.3 mm silicon chip while the actual ISFET array covered an area of 715.8 x 715.8 μm consisting of 4096 ISFET pixels in total with a 1 μm separation space among them. The maximum spatial resolution was 10.2 x 10.2 μm, the size of each ISFET pixel. Each pixel contained 3 NMOS and one PMOS ISFET device. Schematic and layout representation of the chip were designed and simulated using the HIT-Kit v.3.70 design libraries from austriamicrosystems.

The chip's ion sensitive layer was a silicon nitride layer, the final top layer of the AMS 0.35 μm 4-metal CMOS technology used. Our measurements showed an average sensitivity of silicon nitride to be 20-25 mV/pH although it reached higher values when chip and reference electrode was better maintained and around 9-15 mV/pK. The sensitivity was sufficient enough to monitor a 65 mV change during our glucose experiments and the 55 mV difference in amplitude during photosynthesis experiments.

The interface between the chip and the NI PXIe-6358 measurement cards was maintained with the use of printed circuit boards (PCBs), which they also provided test pins in order to detect and correct any possible hardware problems. A custom Ag/AgCl reference electrode was used providing more accuracy than commercial ones on our specific measurements.

8.1.2 Real-time data acquisition

The ISFET array was capable of non-equilibrium chemical measurements. The real-time data acquisition was capable of a maximum of 40 μs per pixel and a 10.2 ms per array sampling rate. For data-size reasons though, a 400 μs per pixel rate was satisfactory for our measurements, so the previously designed program was slightly modified in order to cover our needs. Acquisition was carried out with the use of two PXIe-6358 measurement cards on a PXIe-1073 5-slot chassis and the use of a LabVIEW data acquisition software.

8.1.3 Packaging and encapsulation

Chips were attached on the Printed Circuit Boards with the use of ceramic PGA-100 chip carriers which provided the appropriate number of pins for our chip. Also, plastic chip carriers have been tried, but they didn't produce robust results as the ceramic ones. Wire bonding of the chip onto the carriers was conducted in a technical laboratory of the Physics Department of the University of Glasgow. A two-component epoxy was used to insulate wire bonding of the ISFET from the aqueous solutions. Thus, Epotek 302-3M solution A and B were mixed in the suggested ratio to provide insulation. Due to the arc-shape formed in wire bonding we had to apply various layers of epoxy to ensure insulation, always waiting for the previous layer to fully dry in room temperature, a process taking 24 h for each layer. Finally, plastic cylinders were cut, in different lengths according to experiments and glued on the chip with epoxy or super glue to provide the reaction chamber of the ISFET array chip. Some cylinders had screw caps attached which provided storage for longer periods of time, while others had to be crafted as short as possible for the easy access of other devices such as microscopes and micromanipulators.

8.1.4 Measurement results

Various experiments were conducted with the 64 x 64-pixel ISFET sensor array throughout this thesis. Initial experiments were mostly about checking and

testing the system's integrity and robustness. The chip's sensitivity was verified to be around 20 mV/pH although with better maintained reference electrodes and advanced packaging techniques sometimes larger sensitivity for Hydrogen Ions were obtained. Experiments with potassium showed a sensitivity reaching 9-15 mV/pK.

Additional layers were embedded to the ISFET array chip to induce selectivity in ions. Particularly, an 8-ple additional layer made from a specific polyoxometalate crown heteropolyanion was used in order to bind potassium cations. When the layer was added, a single measurement consisting of hydrogen cations, sodium cations and potassium cations showed a clear response from the potassium cations and little or zero response from the other cations, supporting the selectivity assumption. Moreover, more advanced and controllable experiments were conducted with clearer responses for protons with new methods of solution injection on the chip, experiments that most probably reached sensitivity to new limits.

The ISFET chip was used to monitor possible precipitate formation of Ti(BALDH) (Titanium(IV) bis (ammonium lactato) dihydroxide) salt using the papain enzyme. This elementary measurement was a first temporal and spatial representation of an ionic reaction where enzymes were involved.

An essential part of our experiments were related to the hexokinase reaction measurements. We settled the base point of a study involving enzyme dynamics by attempting to monitor the first step of the biological procedure called glycolysis. This was made possible with the use of a layer made of hexokinase-infused microbeads placed on the chip's surface. This also provided us with the potential to study the reaction diffusion properties. We found the mean value of the diffusivity coefficient to be $3.5 \cdot 10^{-5} cm^2 \cdot s^{-1}$. The temporal response of the reaction was 65 mV for most of the pixels.

Finally, the bioelectrochemical behaviour of photosynthetic bacteria was studied in various conditions. Ionic oscillations were detected under darkness or light conditions similar to oscillations found in literature. The need of biofilm formation was suggested in order to obtain a suitable interface with the sensor for more sophisticated experiments. Thus, inducing darkness-light intervals we managed to demonstrate interval-related voltage differences related to the

photosynthetic ability of the bacterial culture. The voltage difference signal reached 55 mV.

8.2 Future work

8.2.1Short term objectives: Enhanced packaging

Some modifications in packaging can lead to new approaches on measurements. Multiple loci with physical boundaries can be introduced where experiments can be run simultaneously with different solutions or layers. In other words, certain number of pixels of an ISFET array can be used for a measurement and in some other area of the chip, pixels can be used for another measurement. This improved sensor can be capable of multiple experiments saving time and space and enhancing sensing to other approaches. Locality on measurements can be achieved with the use of micromanipulators, such as the ones used for cell research in biology. Attempts of micro-manipulating have already been tested but there were not included in this thesis. The minimum size that could be achieved for the reaction chamber on the chip would be crucial for the introduction of the micromanipulator along with any additional monitoring microscope.

8.2.2 Medium term objectives: Quality of passivation

We followed a standard custom technique for the chip's passivation using liquid resins which solidify through time. More sophisticated and standardized passivation is also achievable with the use of industrial techniques provided by certain companies. Also with the use of 3-D printing we can acquire more detailed patterns which can be embeddable to the chip's surface for passivation reasons. With more standardized passivation we manage to manipulate more robust and reliable chips, but cost can be an issue to look at more extensively.

8.2.3 Long term objectives: a. Additional ion sensitive layers.

Since the chip surface has been tested extensively, we started conducting measurements with additional ion sensitive layers. This opens the way to numerous applications of extra layers. Some tests to induce selectivity have been already made for potassium ions, but there are also other materials for investigating ionic sensitivity for cations essential to biomedical research such as calcium [83] [84] [85], magnesium [86] ions or other ions [87]. Tantalum pentoxide is a good candidate for an additional layer which could be used either on top of the present silicon oxide/nitride layer or after etching the latter one and replace it.

b. Advanced circuit design

A new 256x256 pixel design has already been fabricated and awaiting to be tested and used providing better resolution and possibly better time response. With the appropriate use of the auxiliary circuitry and ensuring that there would be no significant deceleration of the scanning rate the system can be further enhanced with the use of more pixels providing higher resolution, more space for reactions and also being able to act as a multiple ion sensor with even different layers on specific loci of the array.

References

[1] B. Nemeth, M. S. Piechocinski, and D. R. S. Cumming, “High-resolution real-time ion-camera system using a CMOS-based chemical sensor array for proton imaging,” *Sensors Actuators B Chem.*, vol. 171–172, pp. 747–752, Aug. 2012.

[2] P. Bergveld, “Development of an Ion-Sensitive Solid-State Device for Neurophysiological Measurements,” *Biomed. Eng. IEEE Trans.*, vol. BME-17, no. 1, pp. 70–71, May 1970.

[3] S. Alegret, J. B. C. Jimeneq, and M. Valle, “pH-ISFET with NMOS Technology,” *Electroanalysis*, vol. 3, no. 4–5, pp. 355–360, 1991.

[4] L. Bousse, J. Shott, and J. D. Meindl, “A process for the combined fabrication of ion sensors and CMOS circuits,” *IEEE Electron Device Lett.*, vol. 9, no. 1, pp. 44–46, Jan. 1988.

[5] A. Hassibi and T. H. Lee, “A Programmable 0 . 18- μ m CMOS Electrochemical Sensor Microarray for Biomolecular Detection,” *Sensors Journal, IEEE*, vol. 6, no. 6, pp. 1380–1388, 2006.

[6] B. Nemeth, C. Busche, S. Tsuda, L. Cronin, and D. R. S. Cumming, “Imaging the Belousov-Zhabotinsky reaction in real time using an ion sensitive array.,” *Chem. Commun. (Camb).*, vol. 48, no. 42, pp. 5085–7, May 2012.

[7] B. Nemeth, M. D. Symes, A. G. Boulay, C. Busche, G. J. T. Cooper, D. R. S. Cumming, and L. Cronin, “Real-time ion-flux imaging in the growth of micrometer-scale structures and membranes.,” *Adv. Mater.*, vol. 24, no. 9, pp. 1238–42, Mar. 2012.

[8] P. Bergveld, “Thirty years of ISFETOLOGY,” *Sensors Actuators B Chem.*, vol. 88, no. 1, pp. 1–20, Jan. 2003.

[9] R. A. D. A.K. Covington, R.G. Bates, “DEFINITION OF pH SCALES , STANDARD REFERENCE VALUES , MEASUREMENT OF pH AND RELATED TERMINOLOGY,” *Pure Appl. Chem.*, vol. 57, no. 3, pp. 531–542, 1985.

[10] P. Bergveld, “Development , Operation , and Application of the Ion-Sensitive Field-Effect Transistor as a Tool for Electrophysiology,” *IEEE Trans. Biomed. Eng.*, vol. BME-19, no. 5, pp. 342–351, 1972.

[11] L. R. F. A.J. Bard, “Electrochemical Methods: Fundamental and Applications, 2nd ed. Masachussets, United States of America: John Wiley and Sons, 2001,” *Chapter 3*.

[12] S. D. Collins, “Practical limits for solid-state reference electrodes,” *Sensors Actuators B Chem.*, vol. 10, no. 3, pp. 169–178, Feb. 1993.

[13] D. C. Grahame, “The Electrical Double Layer and the Theory of Electrocapillarity.,” *Chem. Rev.*, vol. 41, no. 3, pp. 441–501, 1947.

[14] W. M. and R. S. C. C. Siu, “Basic Properties of the Electrolyte-Si02-Si System :Physical and Theoretical Aspects,” *Electron Devices, IEEE Trans.*, vol. 26, no. 11, pp. 1805–1815, 1979.

[15] and T. W. H. Yates, D.E., S. Levine, “Site-binding Model of the Electrical Double Layer at the Oxide / Water Interface,” *J. Chem. Soc. Faraday Trans. 1 Phys. Chem. Condens. Phases*, vol. 70, pp. 1807–1818, 1973.

[16] J. D. Harame, D.L. ; IBM Thomas J. Watson Research Center, Yorktown Heights, NY ; Bousse, L.J. ; Shott, J.D. ; Meindl, “Development of an Ion-Sensitive Solid-State Device for Neurophysiological Measurements,” *Biomed. Eng. IEEE Trans.*, vol. 34, no. 8, pp. 1700–1707, 1970.

[17] and P. B. Bousse, L., N.F. De Rooij, “Operation of chemically sensitive fieldeffect sensors as a function of the insulator-electrolyte interface,” *Electron Devices, IEEE Trans.*, vol. 30, no. 10, pp. 1263–1270, 1983.

[18] M. J. Milgrew, *An integrated CMOS sensor array technology for direct extracellular ion imaging*. 2007.

[19] K. D. Matsuo, Tadayuki, Wise, “An Integrated Field-Effect Electrode for Biopotential Recording,” *Biomed. Eng. IEEE Trans.*, vol. BME–21, no. 6, pp. 485–487, 1974.

[20] S. D. Moss, J. Janata, and C. C. Johnson, “Potassium ion-sensitive field effect transistor,” *Anal. Chem.*, vol. 47, no. 13, pp. 2238–2243, Nov. 1975.

[21] M. Esashi and T. Matsuo, “Integrated micro multi ion sensor using field effect of semiconductor.,” *IEEE Trans. Biomed. Eng.*, vol. 25, no. 2, pp. 184–92, Mar. 1978.

[22] S. Wakida, Y. Kohigashi, K. Higashi, and Y. Ujihira, “Chemically Modified Copper Ion-selective Field-effect Transistor With 7,7,8,8-tetracyanoquinodimethane,” in *Solid-State Sensors and Actuators, 1995 and Eurosensors IX.. Transducers ’95. The 8th International Conference on*, 1995, pp. 925–927.

[23] and J. E. C. Cane, I. Gracia, A. Merlos, M. Lozano, E. Lora-Tamayo, “Compatibility of ISFET and CMOS technologies for smart sensors,” *TRANSDUCERS ’91 1991 Int. Conf. Solid-State Sensors Actuators. Dig. Tech. Pap.*, pp. 225–228.

[24] M. H. H. Wong, White, “A CMOS-integrated `ISFET-operational amplifier’ chemical sensor employing differential sensing,” *Electron Devices, IEEE Trans.*, vol. 36, no. 3, 1989.

[25] J. Bausells, J. Carrabina, a Errachid, and a Merlos, “Ion-sensitive field-effect transistors fabricated in a commercial CMOS technology,” *Sensors Actuators B Chem.*, vol. 57, no. 1–3, pp. 56–62, Sep. 1999.

[26] H. A. T. Matsuo, M. Esashi, “pH ISFET’s using Al2O3,Si3N4, and SiO2 gate thin films,” *IEEE Trans. Electron Devices*, vol. 26, no. 11, pp. 1856–1857, 1979.

[27] W. G. P. Gimmel, B. Gompf, D. Schmeisser, H.D. Wiemhöfer, “Ta2O5-gates of pH-sensitive devices: Comparative spectroscopic and electrical studies,” *Sensors and Actuators*, vol. 17, no. 1–2, pp. 195–202, 1989.

[28] W. W. A. Olszyna and W. T. D. Sobczyńska, “A study of borazon-gate pH-sensitive field effect transistors,” *J. Cryst. Growth*, vol. 82, no. 4, pp. 757–760, 1987.

[29] W. T. Dorota Sobczyńska, “ZrO2 gate pH-sensitive field effect transistor,” *Sensors and Actuators*, vol. 6, no. 2, pp. 93–105, 1984.

[30] J. A. Mihell and J. K. Atkinson, “Planar thick-film pH electrodes based on ruthenium dioxide hydrate,” *Sensors and Actuators*, vol. 48, no. 1–3, pp. 505–511, 1998.

[31] Y.-L. Chin, J.-C. Chou, Z.-C. Lei, and T.-P. Sun, “Titanium Nitride Membrane Application to Extended Gate Field Effect Transistor pH Sensor Using VLSI Technology,” *Jpn. J. Appl. Phys.*, vol. 40, p. 6311, 2001.

[32] K. Tsukada, T. Kiwa, T. Yamaguchi, S. Migitaka, Y. Goto, and K. Yokosawa, “A study of fast response characteristics for hydrogen sensing with platinum FET sensor,” *Sensors Actuators B Chem.*, vol. 114, pp. 158–163, 2006.

[33] W. Huang, H. Cao, S. Deb, M. Chiao, and J. C. Chiao, “A flexible pH sensor based on the iridium oxide sensing film,” *Sensors Actuators A. Phys.*, vol. 169, no. 1, pp. 1–11, 2011.

[34] V. Jankovic and J. P. Chang, “HfO 2 and ZrO 2 – Based Microchemical Ion Sensitive Field Effect Transistor (ISFET) Sensors : Simulation & Experiment,” *J. Electrochem. Soc.*, vol. 158, no. 10, pp. 115–117, 2011.

[35] M. J. Milgrew, P. a. Hammond, and D. R. S. Cumming, “The development of scalable sensor arrays using standard CMOS technology,” *Sensors Actuators B Chem.*, vol. 103, no. 1–2, pp. 37–42, Sep. 2004.

[36] M. J. Milgrew, M. O. Riehle, and D. R. S. Cumming, “A large transistor-based sensor array chip for direct extracellular imaging,” *Sensors Actuators B Chem.*, vol. 111–112, pp. 347–353, Nov. 2005.

[37] P. Shields, B. Nemeth, R. B. Green, M. O. Riehle, D. R. S. Cumming, and S. Member, “High-Speed Imaging of 2-D Ionic Diffusion Using a 16 × 16 Pixel CMOS ISFET Array on the Microfluidic Scale,” *Sensors Journal, IEEE*, vol. 12, no. 9, pp. 2744–2749, 2012.

[38] J. M. Rothberg, W. Hinz, T. M. Rearick, J. Schultz, W. Mileski, M. Davey, J. H. Leamon, K. Johnson, M. J. Milgrew, M. Edwards, J. Hoon, J. F. Simons, D. Marran, J. W. Myers, J. F. Davidson, A. Branting, J. R. Nobile, B. P. Puc, D. Light, T. a Clark, M. Huber, J. T. Branciforte, I. B. Stoner, S. E. Cawley,

M. Lyons, Y. Fu, N. Homer, M. Sedova, X. Miao, B. Reed, J. Sabina, E. Feierstein, M. Schorn, M. Alanjary, E. Dimalanta, D. Dressman, R. Kasinskas, T. Sokolsky, J. a Fidanza, E. Namsaraev, K. J. McKernan, A. Williams, G. T. Roth, and J. Bustillo, "An integrated semiconductor device enabling non-optical genome sequencing.," *Nature*, vol. 475, no. 7356, pp. 348–52, Jul. 2011.

[39] M. L. Pourciel-Gouzy, W. Sant, I. Humenyuk, L. Malaquin, X. Dollat, and P. Temple-Boyer, "Development of pH-ISFET sensors for the detection of bacterial activity," *Sensors Actuators B Chem.*, vol. 103, no. 1–2, pp. 247–251, Sep. 2004.

[40] M. Castellarnau, N. Zine, J. Bausells, C. Madrid, a. Juárez, J. Samitier, and a. Errachid, "Integrated cell positioning and cell-based ISFET biosensors," *Sensors Actuators B Chem.*, vol. 120, no. 2, pp. 615–620, Jan. 2007.

[41] P. B. Bart H. van der Schoot, "ISFET based enzyme sensors.," *Biosensors*, vol. 3, no. 3, pp. 161–86, 1988.

[42] X.-L. Luo, J.-J. Xu, W. Zhao, and H.-Y. Chen, "Glucose biosensor based on ENFET doped with SiO2 nanoparticles," *Sensors Actuators B Chem.*, vol. 97, no. 2–3, pp. 249–255, Feb. 2004.

[43] K. Y. Park, S. B. Choi, M. Lee, B. K. Sohn, and S. Y. Choi, "ISFET glucose sensor system with fast recovery characteristics by employing electrolysis," *Sensors Actuators, B Chem.*, vol. 83, no. 1–3, pp. 90–97, 2002.

[44] P. Bombelli, M. Zarrouati, R. J. Thorne, K. Schneider, S. J. L. Rowden, A. Ali, K. Yunus, P. J. Cameron, A. C. Fisher, D. Ian Wilson, C. J. Howe, and A. J. McCormick, "Surface morphology and surface energy of anode materials influence power outputs in a multi-channel mediatorless bio-photovoltaic (BPV) system.," *Phys. Chem. Chem. Phys.*, vol. 14, no. 35, pp. 12221–9, Sep. 2012.

[45] "austriamicrosystems AG [Online]. Available: http://www.austriamicrosystems.com, December 2011." .

[46] B. Nemeth, "Ion camera development for real – time acquisition of localised pH responses using the CMOS based 64 × 64 – pixel ISFET sensor array technology," 2012.

[47] D. A. Fiedler, M. Koppenol, and A. M. Bond, "An ESR-Electrochemical Cell Which Can Be Used in High and Low Dielectric Solvents Over Wide Ranges of Temperature and Time Domain," *J. Electrochem. Soc.*, vol. 142, no. 3, pp. 862–867, 1995.

[48] L. Bousse and N. F. de R. H.H. van den Vlekkert, "Hysteresis in A1203 - gate ISFETs," *Sensors Actuators B Chem.*, vol. 2, no. 2, pp. 103–110, 1990.

[49] B. Hajji, J. Launay, T. Conto, and A. Martinez, "pH , pK and pNa detection properties of SiO 2 / Si 3 N 4 ISFET chemical sensors," *Microelectron. Reliab.*, vol. 40, no. 4–5, pp. 783–786, 2000.

[50] A. Errachid, J. Bausells, and J.-R. N, “A simple REFET for pH detection in differential mode,” *Sensors Actuators B Chem.*, vol. 60, no. 1, pp. 43–48, 1999.

[51] P.-K. Shin and T. Mikolajick, “Alkali- and hydrogen ion sensing properties of LPCVD silicon oxynitride thin films,” *Thin Solid Films*, vol. 426, no. 1–2, pp. 232–237, Feb. 2003.

[52] A. T. Roland Contant, “A new crown heteropolyanion K28Li5H7P8W48O184.92H2O: synthesis, structure, and properties,” *Inorg. Chem*, vol. 24, pp. 4610–4614, 1985.

[53] T. Boyd, S. G. Mitchell, D. Gabb, D.-L. Long, and L. Cronin, “Investigating cation binding in the polyoxometalate-super-crown [P8W48O184]40-.,” *Chemistry*, vol. 17, no. 43, pp. 12010–4, Oct. 2011.

[54] S. Jamasb, S. Collins, and R. L. Smith, “A physical model for drift in pH ISFETs,” *Sensors Actuators B Chem.*, vol. 49, no. 1–2, pp. 146–155, 1998.

[55] P. B. Luc Bousse, “The role of buried OH sites in the response mechanism of inorganic-gate pH-sensitive ISFETs,” *Sensors and Actuators*, vol. 6, pp. 65–78, 1984.

[56] R. L. Brutchey and D. E. Morse, “Silicatein and the Translation of its Molecular Mechanism of Biosilicification into Low Temperature Nanomaterial Synthesis,” *Chem. Rev.*, no. 108, pp. 4915–4934, 2008.

[57] G. P. Smith, K. J. Baustian, C. J. Ackerson, and D. L. Feldheim, “Metal oxide formation by serine and cysteine proteases,” *J. Mater. Chem.*, vol. 19, no. 44, p. 8299, 2009.

[58] T. C. A.H. Romano, “Evolution of carbohydrate metabolic pathways,” *Res. Microbiol.*, vol. 147, no. 6–7, pp. 448–455, 1996.

[59] R. a Robergs, F. Ghiasvand, and D. Parker, “Biochemistry of exercise-induced metabolic acidosis.,” *Am. J. Physiol. Regul. Integr. Comp. Physiol.*, vol. 287, no. 3, pp. R502–16, Sep. 2004.

[60] T. Zhang and E. V Anslyn, “Using an indicator displacement assay to monitor glucose oxidase activity in blood serum.,” *Org. Lett.*, vol. 9, no. 9, pp. 1627–9, Apr. 2007.

[61] G. Lucarelli, M. Fanelli, A. M. V. Larocca, C. A. Germinario, M. Rutigliano, A. Vavallo, F. P. Selvaggi, C. Bettocchi, M. Battaglia, and P. Ditonno, “Serum sarcosine increases the accuracy of prostate cancer detection in patients with total serum PSA less than 4.0 ng/ml.,” *Prostate*, vol. 72, no. 15, pp. 1611–21, Nov. 2012.

[62] S. Buervenich, O. Sydow, A. Carmine, Z. Zhang, M. Anvret, and L. Olson, “Alcohol dehydrogenase alleles in Parkinson’s disease,” *Mov. Disord.*, vol. 15, no. 5, pp. 813–818, Sep. 2000.

[63] I. P. Hall, “Stratified medicine: drugs meet genetics.,” *Eur. Respir. Rev.*, vol. 22, no. 127, pp. 53–7, Mar. 2013.

[64] T. García-Berrocoso, A. Penalba, C. Boada, D. Giralt, E. Cuadrado, N. Colomé, L. Dayon, F. Canals, J.-C. Sanchez, A. Rosell, and J. Montaner, “From brain to blood: New biomarkers for ischemic stroke prognosis.,” *J. Proteomics*, vol. 94, pp. 138–48, Dec. 2013.

[65] Sigma-Aldrich, “Cyanogen Bromide activated agarose gel,” *Cyanogen Bromide Act. agarose gel*.

[66] “Sigma-Aldrich® product information sheet [Online] http://www.sigmaaldrich.com/catalog/product/sigma/c9142?lang=en&region=GB.” .

[67] A. Einstein, “Über die von der molekularkinetischen Theorie der Wärme geforderte Bewegung von in ruhenden Flüssigkeiten suspendierten Teilchen,” *Ann. Phys.*, vol. 322, no. 8, 1905.

[68] T. Kaneko and S. Tabata, “Complete genome structure of the unicellular cyanobacterium Synechocystis sp. PCC6803.,” *Plant Cell Physiol.*, vol. 38, no. 11, pp. 1171–1176, 1997.

[69] N. Quintana, F. Van Der Kooy, M. D. Van De Rhee, G. P. Voshol, and R. Verpoorte, “Renewable energy from Cyanobacteria: Energy production optimization by metabolic pathway engineering,” *Appl. Microbiol. Biotechnol.*, vol. 91, no. 3, pp. 471–490, 2011.

[70] A. M. L. van de Meene, M. F. Hohmann-Marriott, W. F. J. Vermaas, and R. W. Roberson, “The three-dimensional structure of the cyanobacterium Synechocystis sp. PCC 6803.,” *Arch. Microbiol.*, vol. 184, no. 5, pp. 259–70, Jan. 2006.

[71] L. Mao and W. S. Verwoerd, “Genome-scale stoichiometry analysis to elucidate the innate capability of the cyanobacterium Synechocystis for electricity generation.,” *J. Ind. Microbiol. Biotechnol.*, vol. 40, no. 10, pp. 1161–80, Oct. 2013.

[72] T. Kaneko, S. Sato, H. Kotani, a. Tanaka, E. Asamizu, Y. Nakamura, N. Miyajima, M. Hirosawa, M. Sugiura, S. Sasamoto, T. Kimura, T. Hosouchi, a. Matsuno, a. Muraki, N. Nakazaki, K. Naruo, S. Okumura, S. Shimpo, C. Takeuchi, T. Wada, a. Watanabe, M. Yamada, M. Yasuda, and S. Tabata, “Sequence Analysis of the Genome of the Unicellular Cyanobacterium Synechocystis sp. Strain PCC6803. II. Sequence Determination of the Entire Genome and Assignment of Potential Protein-coding Regions,” *DNA Res.*, vol. 3, no. 3, pp. 109–136, Jan. 1996.

[73] Y. Nakamura, T. Kaneko, M. Hirosawa, N. Miyajima, and S. Tabata, “CyanoBase , a www database containing the complete nucleotide sequence of the genome of Synechocystis sp. strain PCC6803,” *Nucl. Acids Res.*, vol. 26, no. 1, pp. 63–67, 1998.

[74] Z. I. Johnson, E. R. Zinser, A. Coe, N. P. Mcnulty, E. M. S. Woodward, and S. W. Chisholm, “Niche Partitioning Among Prochlorococcus Ecotypes Along Ocean-Scale Environmental Gradients,” *Science (80-.).*, vol. 311, no. March, pp. 1737–1740, 2006.

[75] K. Kucho, K. Okamoto, Y. Tsuchiya, S. Nomura, M. Nango, M. Kanehisa, and M. Ishiura, “Global analysis of circadian expression in the cyanobacterium Synechocystis sp. strain PCC 6803.,” *J. Bacteriol.*, vol. 187, no. 6, pp. 2190–9, Mar. 2005.

[76] S. Aoki, T. Kondo, H. Wada, M. Ishiura, S. Aoki, T. Kondo, and H. Wada, “Circadian rhythm of the cyanobacterium Synechocystis sp . strain PCC 6803 in the dark . Circadian Rhythm of the Cyanobacterium Synechocystis sp . Strain PCC 6803 in the Dark,” *J. Bacteriol.*, vol. 179, no. 18, pp. 5751–5755, 1997.

[77] A. Mitsui, S. Cao, A. Tiikahashi, and T. Arai, “Growth synchrony and cellular parameters of the unicellular nitrogen-fixing marine cyanobacterium , Synechococcus sp . strain Miami BG 043511 under continuous illumination,” *Physiol. Plant.*, vol. 69, 1987.

[78] M. H. and R. Y. S. Rosmarie Rippka, Josette Deruelles, John B. Waterbury, “Generic Assignments , Strain Histories and Properties of Pure Cultures of Cyanobacteria,” *J. Gen. Microbiol.*, vol. 110, no. 2, pp. 1–61, 1979.

[79] Y. Liu, N. F. Tsinoremas, C. H. Johnson, N. V Lebedeva, S. S. Golden, M. Ishiura, and T. Kondo, “Circadian orchestration of gene expression in cyanobacteria.,” *Genes Dev.*, vol. 9, no. 12, pp. 1469–1478, Jun. 1995.

[80] R. H. Crlst, K. Oberholser, D. Schwartz, J. Marzoff, and D. Ryder, “" Interactions of Metals and Protons with Algae,” *Environ. Sci. Technol.*, vol. 22, no. 7, pp. 755–760, 1988.

[81] D. L. R. W. D. P. S. Robert H. Reed, “Na+ uptake and extrusion in the cyanobacterium Synechocystis PCC 6714 in response to hypersaline treatment. Evidence for transient changes in plasmalemma Na+ permeability,” *Biochim. Biophys. Acta*, vol. 814, pp. 347–355, 1985.

[82] K. Kucho, K. Okamoto, Y. Tsuchiya, S. Nomura, M. Nango, M. Kanehisa, M. Ishiura, and S. Pcc, “Global Analysis of Circadian Expression in the Cyanobacterium Synechocystis sp . Global Analysis of Circadian Expression in the Cyanobacterium,” *J. Bacteriol.*, vol. 187, no. 6, pp. 2190–2199, 2005.

[83] A. van den Berg, A. Grisel, and E. Verney-Norberg, “An ISFET-based calcium sensor using a photopolymerized polysiloxane membrane,” *Sensors Actuators B Chem.*, vol. 4, no. 1991, pp. 235–238, 1991.

[84] A. Bratov, N. Abramova, C. Domínguez, and A. Baldi, “Ion-selective field effect transistor (ISFET)-based calcium ion sensor with photocured polyurethane membrane suitable for ionised calcium determination in milk,” *Anal. Chim. Acta*, vol. 408, pp. 57–64, 2000.

[85] J. Artigas, a Beltran, C. Jiménez, J. Bartrolí, and J. Alonso, “Development of a photopolymerisable membrane for calcium ion sensors,” *Anal. Chim. Acta*, vol. 426, pp. 3–10, 2001.

[86] A. Seki, K. Motoya, S. Watanabe, and I. Kubo, “Novel sensors for potassium, calcium and magnesium ions based on a silicon transducer as a light-addressable potentiometric sensor,” *Anal. Chim. Acta*, vol. 382, pp. 131–136, 1999.

[87] M. L. Hamlaoui, R. Kherrat, M. Marrakchi, N. Jaffrezic-Renault, and a. Walcarius, “Development of an ammonium ISFET sensor with a polymeric membrane including zeolite,” *Mater. Sci. Eng. C*, vol. 21, pp. 25–28, 2002.